DTU Physics
Department of Physics

MSc. Thesis

Hydrodynamic interactions in microfluidic acoustophoresis

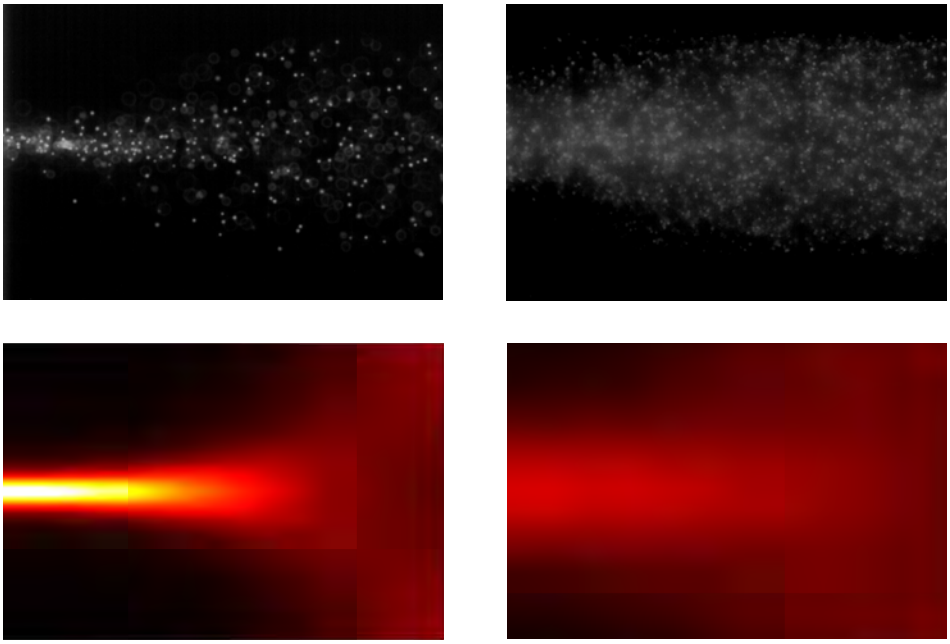

Mikkel Wennemoes Hvitfeld Ley, s082635

Supervisor: Henrik Bruus

DTU Physics
Technical University of Denmark
2014 February 19

Cover illustration

Top: Experimental measurement of acoustophoretic focusing of polystyrene microparticles in a microfluidic channel. Left: Dilute suspension. Right: concentrated suspension.
Bottom: Corresponding theoretical predictions.

Abstract

We present a theoretical modelling framework for simulating the behaviour of micron sized particles, suspended in a Newtonian fluid, undergoing microfluidic acoustophoresis. Within this framework, we have mainly focused on two things. 1) Identifying the critical particle concentrations, where particle-particle interactions, significantly changes the particle dynamics. 2) Characterising the particle dynamics above these levels, compared to that of dilute particle suspensions.

This was achieved by deriving the particles as a continuous concentration field, and numerically implementing hydrodynamic interaction effects. At sufficiently high particle concentrations, these interaction effects give rise to changes in the particle dynamics. Two types of interaction mechanism are investigated. 1) The effect of increasing the effective suspension viscosity, and Stokes drag forces on the particles, as particle concentration increases. 2) The effect of letting the particles exert a force on the fluid, setting it in motion, which in turn changes the suspension dynamics by fluid convection. It is found that the first type of interactions, is by far the most dominant for purposes of particle focusing and up-concentration, within the geometry and acoustic fields investigated in this work. As a general result, it is found that the particle dynamics slows down, for increasing particle concentrations. Specifically, we find that the focus time increases by 50 for 1% particle volume concentration, and 100% for 3 % particle volume, where both are compared to the focus times of dilute suspensions. For different particle sizes, very little differences in focusing times are observed..

We find that the second type of interactions (convective), are crucial for a general correct description of the particle dynamics. Though minutely influential for the net particle transport, for the geometry and acoustic fields investigated here.

In addition to the theoretical work, we present qualitative comparisons with experiments, performed in collaboration with the Faculty of Engineering of Lund Technical University. Preliminary comparisons reveal that the numerical model proposed, captures the overall behaviour of dilute as well as concentrated particle suspensions, in microfluidic acoustophoresis. It is concluded that further experimental and theoretical investigation, would allow model improvements that would permit direct quantitative comparison between theory and experiment.

Resumé

Vi præsenterer et teoretisk modelleringssystem til simulering af mikrometer størrelse partikler opslæmmet i en Newtonsk væske, under påvirkining af mikrofluidisk akustoforese. Fokus har været hovedsageligt været på to punkter. 1) Identifikation af de kritiske koncentrationsniveauer, hvor partikel-partikel vekselvirkninger betydeligt ændrer partikeldynamikken. 2) Karakterisere denne dynamik over disse kritiske grænser, sammenlignet med dynamikken for fortyndede partikel opslæmninger.

Dette blev opnået ved at betragte partiklerne som et kontinuert koncentrationsfelt, og numerisk implementere hydrodynamiske vekselvirkninger. Disse vekselvirkinger giver anledning til ændringer i partikeldynamikken, ved tilstrækkelig høj partikelkoncentration. To typer af vekselvirkningsmekanismer blev udforsket. 1) Effekten af en forøgelse af den effektive viskositet af hele mediet, samt en forøgelse af Stokes trækkræfterne påpartiklerne, når partikelkoncentrationen gradvist øges. 2) Effekten af at lade partiklerne virke påvæsken med en kraft, hvilket sætter væsken i bevægelse og ændrer partiklernes bevægelse grundet konvektion. Det konkluderes, at den første mekanisme er den dominerende mht. opkoncentrering og fokusering af partiklerne, for den specifikke geometri og akustiske felter, studeret i dette arbejde. Generelt finder vi at partikeldynamikken går langsommere, for voksende partikelkoncentrationer. Mere specifikt, findes det at partikelfokuseringstiden forøges med 50% ved 1% partikel volumen, og 100% ved 3% partikel volumen, begge sammenlignet med fokustider for fortyndede partikelopslæmninger. For forskelige partikelstørrelser, finder vi meget småforskelle i fokustider.

For den anden type vekselvirkninger (konvektion), finder vi at den er afgørende for en korrekt generel beskrivelse af partikeldynamikken, men at den har minimal indflydelse pånetto transporten af partikler, for den, her studerede geometri samt specifikke akustiske felter.

Udover det teoretiske arbejde, præsenteres kvalitative sammenligner med eksperimenter, udført i samarbejde med Lund Tekniske Højskole (LTH). Foreløbige sammenligner viser at den udarbejdede numeriske model fanger essensen i partikeldynamikken, både for fortyndede såvel som højt koncentrerede partikelopslæmninger i mikrofluidisk akustoforese. Det konkluderes at yderligere eksperimenter og teoretiske undersøgelser vil muliggøre modelforbedringer, der vil tillade direkte kvantitative sammenligninger mellem teori og eksperiment.

Preface

This thesis is submitted as partial fulfillment of the requirements for obtaining the degree in Master of Science in Engineering at the Technical University of Denmark (DTU). The thesis work was carried out the department of physics (DTU Physics), at the group Theoretical Microfluidics (TMF), headed by Professor Henrik Bruus. The work was carried out in the period from 19 August 2013 to 18 February, and corresponds to a workload of 35 ECTS credits.

The main contribution of this thesis work, should be seen as the compilation of a physically realistic model for hydrodynamic interactions in acoustophoresis, constructed from various established theoretical models, more than development of new theoretical ground. Furthermore, we present only about a third of the numerical work carried out, as challenges concerning mesh convergence and the exact numerical weak form implementation in COMSOL initially proved problematic.

First and foremost, I would like to thank my supervisor Henrik Bruus, for always keeping me on the right track, but probably most of all for his endless dedication in teaching me not only physics, but also how to be a physicist. Secondly, I would like to thank the TMF research group, for creating an inspiring work place everyday that is impressively professional and relaxed at the same time. Especially I would like to thank my fellow master student in acoustofluidics Jonas T. Karlsen, partly for always being ready to bounce ideas of off, and for making the long office ours fun and enjoyable.

Next, I would like to thank Professor Thomas Laurell for kindly hosting us at Lund University on several occasions, and for a great collaboration collaboration between theory and experiment. Especially, I would like to thank Postdoc Kevin Cushing for a great collaboration, always being willing to, yet again, make one more dataset.

I also wish to express my big gratitude to everybody that has undertaken the assignment of proofreading different parts of my thesis, as this has given me invaluable feedback to improve my thesis work.

Lastly, I would like to thank my loving girlfriend Stine Harrekilde, for all her love and patience during this period, making it a little easier to endure the hard times of the project.

Mikkel Wennemoes Hvitfeld Ley
Department of Physics
Technical University of Denmark
2014 February 19

List of symbols

Symbol	Description	Unit
$2a$	Diameter of microparticle	m
β	Ratio between transverse and lateral wavelength	1
c	Number concentration of particles.	m^{-3}
$d_{\mathrm{p-p}}$	Average particle-particle distance in suspension	m
D	Particle diffusion constant	$\mathrm{m}^2\ \mathrm{s}^{-1}$
δ	Viscous boundary layer thickness	m
E_{ac}	Acoustic energy density	$\mathrm{J}\ \mathrm{m}^{-3}$
η	Dynamic fluid viscosity	Pa s
$\boldsymbol{f}_{\mathrm{ext}}$	External body forces on fluid	$\mathrm{N}\ \mathrm{m}^{-3}$
$\boldsymbol{F}_{\mathrm{ac}}$	Acoustic radiation force on the particles	N
$\boldsymbol{F}_{\mathrm{d}}$	Stokes drag force	N
$\boldsymbol{J}_{\mathrm{p}}$	Particle number current density	$\mathrm{s}^{-1}\ \mathrm{m}^{-2}$
$\boldsymbol{k}$	Wave number of soundwave	m^{-1}
κ_0	Fluid compressibility	Pa^{-1}
κ_{p}	Particle compressibility	Pa^{-1}
m_{p}	Particle mass	kg
N	Total number of microparticles	1
N_{cen}	Number of particles in the innermost 20% of the channel	1
p	Fluid pressure	Pa
$\boldsymbol{r}_{\mathrm{p}}$	Particle position	m
ρ	Mass density of fluid	$\mathrm{kg}\ \mathrm{m}^{-3}$
ρ_{p}	Mass density of particles	$\mathrm{kg}\ \mathrm{m}^{-3}$
$\boldsymbol{\sigma}$	Cauchy Stress tensor	Pa
$\boldsymbol{u}_{\mathrm{p}}$	Microparticle velocity	$\mathrm{m}\ \mathrm{s}^{-1}$
s	Logarithm of the particle number concentration	1
$\boldsymbol{v}$	Fluid velocity	$\mathrm{m}\ \mathrm{s}^{-1}$
v_{s}	Isentropic speed of sound in fluid	$\mathrm{m}\ \mathrm{s}^{-1}$
V_{p}	microparticle volume	m^3
W	Width of the microchannel	m
ϕ	Particle volume concentration	1
ϕ_0	Initial particle volume concentration	1
Φ	Acoustic contrast factor	1
χ	Relative particle mobility	1
ψ	Relative effective medium viscosity	1
ω	Acoustic actuation angular frequency	s^{-1}

Continued on next page.

Symbol	Description	Unit
i	The imaginary unit	
e	Eulers number $\ln(\mathrm{e}) = 1$	
$\partial\Omega$	Boundary of computation domain	m
Ω	Computation domain	m^2
$\boldsymbol{r}$	General position vector	m
(x, y, z)	Cartesian co-ordinates	m
(r, θ, ϕ)	Spherical co-ordinates	m
$\boldsymbol{e}$	Unit vector	1
$\boldsymbol{n}$	Normal unit vector	1
∂_x	Partial x-derivative	m^{-1}
∂_y	Partial y-derivative	m^{-1}
∂_z	Partial z-derivative	m^{-1}
∂_t	Partial time derivative	s^{-1}
d_t	Time derivative	s^{-1}
$\boldsymbol{\nabla}$	Nabla operator	m^{-1}
∇^2	Scalar Laplace operator	m^{-2}
$\langle\square\rangle$	Time average of $\square$	
$\lvert\square\rvert$	Absolute value of $\square$	

List of Figures

Contents

Chapter 1

Introduction and motivation

1.1 Lab-on-a-chip systems

Lab-on-a-Chip systems (LoC) is a technology that was founded in the early 1990s, and has since gained much attention. For an introduction to LoC we refer the reader to the following introductory textbooks [1, 2, 3, 4, 5]. The basic idea in LoC systems, is to downscale and automate, total chemical and biological analysis, on one single chip, which has numerous advantages. Conventionally, chemical and biological analysis takes place in centralised lab with skilled personnel and specialised machinery. Compared to this, LoC technology offers fast analysis, with reduces sample and reagent volumes. This is valuable, especially if sample supply are limited and reagents are costly. Furthermore, the operation of LoC does not necessarily require any special training or education, as it is aimed to be fully automated in the developed commercialised state. This is advantageous for instance in medical tests, where analysis can be performed on-site, with quick feedback to the patients. The downscaling in size allows also for high portability. Examples of this are the monitoring of ammonium in wastewater, or the monitoring of glucose levels in blood for diabetes patients. The possibility of using microfabrication techniques, developed in the MEMS in the 1960s, allows for highly reproducible large scale batch production of LoC devices, potentially reducing costs compared to competing macroscale technologies.

The working principle idea behind LoC, is to utilise the laminar flow structures of submillimetre fluidic channels, for well controlled transport, reaction and mixing of various chemical and biological reagents. This is possible because the small length scales involved, very often makes viscous effects dominant over inertial effects, making the fluid dynamics enter the low Reynolds number regime $Re < 1$. In this regime, very little turbulence exists in the fluid, yielding the predictable laminar flows. This study of fluid behaviour and transport on the microscale, is referred to as Microfluidics.

One of the challenges often encountered in LoC systems, is the handling, separation and manipulation of biological particles such as cells and bacteria. To meet these challenges several techniques have been developed, such as dielectrophoresis, magnetophoresis and optical manipulation [6]. In e.g. magnetophoresis, a small magnetic tag is chemically attached to the bioparticle of interest, allowing manipulation by applying an external magnetic field. One of the strong emerging competitors within manipulation and handling is that of *acoustophoresis*, which is the manipulation of particles by the use of sound.

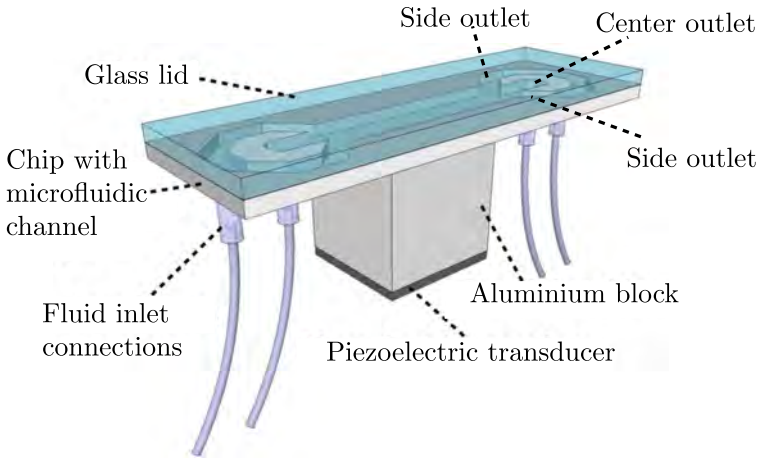

Figure 1.1: Sketch of a typical acoustofluidic setup, where the typical length of the channel is of the order of a few centimeters. Liquid and biological particles of interest are allowed access through the fluid in- and outlet connections. A piezoelectric transducer vibrates the system, typically at MHz frequency, building up a resonant acoustic field in liquid. By scattering of sound waves, the particles feel an acoustic radiation force. This force can cause the particles to migrate by sound (acoustophoresis), towards either the center or side outlets . The figure is adapted from [10].

1.2 Acoustofluidics

Combining acoustophoresis with microfluidics has coined the term *acostofluidics*. In a series of tutorial papers, the Journal *Lab on a Chip* published a number articles on acoustofluidics from 2011-2013 [7], several of which has been used in this thesis work. In acoustophoresis particles migrate due to the scattering of incoming sound waves, transfering momentum to the particles. There are several advantages of using acoustophoresis for separating and manipulating biological particles. Some of them are mentioned in the tutorial paper by Lenshof *et al.* [8]. 1) It is label free, compared to fluorescent or magnetic tagging, where a label is chemically attached. This could for instance be of interest in medical tests, where you prefer no chemicals to have interacted with the sample before analysis. 2) Acoustophoresis has a high potential throughput $\sim$1 L/h, compared to e.g. magnetophoresis which is of the order $\sim$0.01 L/h, and 3) it is harm free for the particles in up-concentration processes, compared to e.g. centrifugation, where particles are subjected to high stresses [9]. The only requirement for using acoustophoresis, is having a difference in acoustic properties between the particle and the suspending liquid medium.

In Fig. 1.1 a typical acoustofludic setup is sketched.

A microfluidic channel is attached to in- and outlet channels, giving access to the fluid and particles. A glass lid is typically attached, allowing for direct visual inspection. The chip is mounted to a piezoelectric transducer that vibrates the channel, typically in the MHz regime. The frequency is chosen, such that a resonant acoustic field, builds up in the liquid. By scattering of incoming ultrasound waves, the particles feel an acoustic radiation force [11]. This force can cause the particles to migrate in the transverse direction, across the width of the channel. This allows for manipulating particles to be directed towards either the center, or the side outlets, by simple adjustment of the piezoelectric actuation. From this simple principle, increasingly advanced devices and techniques are developed. As an example, it was recently demonstrated how more advanced particle manipulation could be achieved using an array of 30 local and individually controlled transducers [12].

Among the applications found for particle manipulation is the removal of a specific type of biological particle away from some medium, e.g. the removal of *E. Coli* bacteria from a suspension with red blood cells [13]. f interest in the acoustofluidic applications, is to separate biological particles directly from biological fluids. One example of this, is the separation of fatty lipids directly from raw milk [14, 10], used for quality control of food products in the dairy industry. Another example is the removal of lipids from blood [15, 16], which is to prevent lipid microembolies in the brain capillaries after cardiac surgery.

One of the challenges in working directly with biofluids such as blood, is that a large fraction of the suspension volume consist of particles. In human blood approximately 45% of the volume consists of red blood cells, white blood cells and blood platelets [16]. Petersson *et al.* [16] reports a lipid separation percentage of 80%, with a red blood cell recovery of 70% in bovine blood. This is compared to a study by the same research group by Nordin and Laurell [17], where prostate cancer cells and red blood cells are upconcentrated from diluted suspensions. In the case of dilute suspensions, Nordin and Laurell [17] measure the recovery percentage of red blood cells to be 97%, compared to the recovery percentage of 70% when using undiluted blood.

In this light, it is clear that directly using biofluid suspensions in acoustofluidic systems poses technological challenges due to the high fractional volume of suspended particles. For suspensions with the mentioned concentration levels, we suspect the observed changes in behaviour to be the result of different particle-particle interactions taking place in the suspension, thus changing the dynamics. This issue is to the authors knowledge not yet resolved.

1.3 Main goal for this project

In this thesis work we take the first steps in meeting the above mentioned technological challenge. We do this by a theoretical investigation of how the behaviour of a particle suspension changes, when the fractional particle volume gradually increases. In biological fluid suspensions, such as blood, there exist a wealth of different types of particles, each having different mechanical properties and various non-trivial shapes. Therefore, in this first investigation we will focus our attention to non-biological suspensions, consisting of hard monodisperse spheres in a Newtonian fluid. With this starting point, we will make a series of simplifications and implement particle-particle interaction mechanisms, in simulations of particle suspensions undergoing acoustophoresis. Within this framework we aim to answer two main question: 1) At what critical concentration levels do the acoustophoretic particle behaviour begin to change significantly, and 2) what characterises the acoustophoretic particle behaviour above this critical level.

1.4 Thesis outline

Chapter 2 - Theory

The fundamental governing equations are outlined, and first-order perturbation theory is employed to derive the acoustic fields in the liquid, and we briefly discuss two second-order acoustic effects. Next we review a theoretical model for the enhanced effective medium viscosity for the suspension and Stokes drag force felt by the particles, both models being functions of particle concentration.

Chapter 3 - Model system

We build the theoretical modelling framework. First we define the outer circumstances: System geometry, external actuation, materials, etc. From this we derive arguments, assumptions and approximations from which we make a series of physically reasonable simplifications, allowing the formulation of solvable governing equations with corresponding boundary conditions. As we go along, we physically motivate the implementation of several hydrodynamic particle-particle interaction mechanisms, implementing them step by step.

Chapter 4 - Numerical implementation in COMSOL

The basic principle of the *finite element method* is outlined, which is a numerical method of solving differential equations. We implement the our model framework in the finite element method using the commercially available software *COMSOL*. The COMSOL model is explained and numerical convergence analysis is performed.

Chapter 5 - Results - Non-interacting particle dynamics

Result are presented for particle suspensions in the non-interacting regime, and compared with experimentally validated results. Moreover, we derive and compare analytical approximate models with the numerical framework presented in chapter 4.

Chapter 6 - Results - interacting particle dynamics

Results are presented for the interacting particle dynamics. The fields of fluid pressure, velocity and particle concentration are plotted and compared for interacting versus non-interacting regimes. We investigate the transient dynamics of the particle focusing and corresponding fluid velocity field, and investigate the impact of different interaction effects on the particle focusing. Lastly we identify critical concentration values, for which hydrodynamic particle interaction are significant.

Chapter 7 - Discussion

We present qualitative comparisons with experimental data are discuss these in relation to the presented model framework. We discuss the implications of the results presented in the previous chapter, and discuss weak and strong points of the model proposed. On the basis of the discussion, we suggest ideas for further work.

Chapter 8 - Conclusion and outlook

Chapter 2

Theory

In this thesis, we aim to derive and understand the dynamics of micrometre sized particles suspended in a Newtonian liquid in the limit of both dilute and concentrated particle concentrations, when subjected to ultrasound waves.

First, we present the governing equations for, and then, using first-order perturbation theory, we will derive the acoustic fields. Next, we discuss some relevant second-order effects that arise from products of the first-order fields. Primarily, the acoustic radiation force will be of interest, since it is the driving force behind the complex dynamics of the microparticles.

Lastly, we review a model describing how the presence of many suspended particles affect the dynamics of single particles, through enhanced effective medium viscosity and decreased particle mobility.

2.1 Governing equations

In the simple cases where the suspended particles are non-interacting, and the fluid remains at rest, the governing equation is simply Newtons second law for a single particle

$$m_\mathrm{p} \mathrm{d}_t^2 \boldsymbol{r}_\mathrm{p} = \boldsymbol{F}_\mathrm{ext}\,, \tag{2.1}$$

where m_p is the mass of the particle, $\boldsymbol{r}_\mathrm{p}$ is the position of the particle and $\boldsymbol{F}_\mathrm{ext}$ is the sum of external forces acting on the particle.

To describe the dynamics of many particles, we employ the continuum limit where the density of particles are given as number concentration field $c(\boldsymbol{r}, t)$. By requiring the total number of particles to be conserved, c must obey a continuity equation

$$\partial_t c = -\boldsymbol{\nabla} \cdot \boldsymbol{J}_\mathrm{p}\,, \tag{2.2}$$

where is $\boldsymbol{J}_\mathrm{p}$ is the particle current density, to be treated in detail later. The microparticle suspension is governed by the Navier-Stokes equation for the liquid, and the continuity equation for the liquid Eq. (2.3b) and the particles Eq. (2.2). For a compressible Newtonian fluid, the Navier-Stokes Eq. and the mass continuity equation are respectively [5, 18],

$$\begin{aligned}\rho(\partial_t + \boldsymbol{v}\cdot\boldsymbol{\nabla})\boldsymbol{v} = &\quad \boldsymbol{\nabla}\cdot\boldsymbol{\sigma} + \boldsymbol{f}_\mathrm{ext} \\ &= -\boldsymbol{\nabla} p + \eta\nabla^2\boldsymbol{v} + \beta_\mathrm{visc}\eta\boldsymbol{\nabla}(\boldsymbol{\nabla}\cdot\boldsymbol{v}) + \boldsymbol{f}_\mathrm{ext}\,,\end{aligned} \tag{2.3a}$$

$$\partial_t \rho = -\boldsymbol{\nabla}\cdot(\rho\,\boldsymbol{v})\,, \tag{2.3b}$$

where ρ is the mass density, $\boldsymbol{v}$ is the fluid velocity, $\boldsymbol{\sigma}$ is the Cauchy stress tensor, p is the pressure, η is the viscosity and β_{visc} is the dimensionless viscosity ratio relating compressional and shear stress, which is approximately 3.0 for water [19]. $\boldsymbol{f}_{\text{ext}}$ is external force densities acting on the liquid. In the description of the sound wave propagation in the liquid, it is useful to relate pressure and mass density. For this, we use the thermodynamic equation of state between pressure and mass density

$$p = p(\rho)\,. \tag{2.4}$$

2.2 Acoustofluidic theory

To find the ultrasonic perturbations to the pressure and velocity we first consider only the fluid and employ basic acoustic perturbation theory. From this, we derive a linear wave equation for the first-order perturbation pressure, and discuss some of the second order effects. Of particular interest, is the acoustic radiation force, which stems from scattering of sound waves on the particles.

The theoretical approach is primarily inspired by Bruus [20], partly by Barnkob [21] and Muller [22], but also by the classic text book by Landau and Lifshitz [23].

The governing equations (2.3a), (2.3b) and (2.2), is a set of second order, non-linear partial differential equations, which are notoriously hard to solve. However, since soundwaves in a fluid are oscillatory motions with small amplitude around equilibrium values [23], we can use perturbation theory.

In perturbation theory, the idea is to expand a physical quantity of interest f, in a small region close to a known solution f_0

$$f = f_0 + \alpha\, f_1 + \alpha^2 f_2 + \ldots\ . \tag{2.5}$$

The fields f_1, f_2, ..., act as perturbations to the known solution f_0, and α is a dimensionless perturbation parameter. This parameter α can then be varied slightly away from 0 to study how the quantity of interest f behaves when being increasingly perturbed from its known state f_0. Convergence of the full perturbation scheme, Eq. (2.5), may be obtained if we require the perturbation parameter α is very small $\alpha \ll 1$.

We consider a quiescent fluid, at thermal equilibrium containing no particles, as the known state f_0. We expand the fields of fluid velocity, mass density and pressure, in a perturbation scheme

$$\boldsymbol{v} = \boldsymbol{0} + \boldsymbol{v}_1 + \boldsymbol{v}_2 + \ldots\,, \tag{2.6a}$$

$$\rho = \rho_0 + \rho_1 + \rho_2 + \ldots\,, \tag{2.6b}$$

$$p = p_0 + p_1 + p_2 + \ldots\,. \tag{2.6c}$$

Here, the small perturbation parameter α is implicitly included in the fields, such that the amplitude of the perturbation fields themselves decrease rapidly with increasing order.

Physically, the first-order fields describe the acoustic sound wave propagation. Knowing that water to a good approximation can be considered incompressible, it reasonable to expect that the mass density perturbation $\approx \rho_1 + \rho_2$ is very small compared to the unperturbed mass density of water ρ_0. For the pressure we find that a proportionality exists between pressure p_1 and mass density ρ_1. This implies that higher order fields of pressure are automatically smaller than p_0 if the perturbations in mass density are small. For the fluid velocity, we note that the liquid is quiescent in the unperturbed state. Therefore, the higher order velocity fields cannot be

compared to the unperturbed fluid velocity. The correct characteristic fluid velocity to compare to the higher order velocity fields will turn out to be the isentropic speed of sound v_s in the liquid.

2.2.1 First-order acoustic fields

To find the first-order fields, we start by performing an isentropic Taylor expansion of the equation of state (2.4) around the equilibrium mass density ρ_0, to first order

$$p(\rho) \simeq p(\rho_0) + \left(\frac{\partial p}{\partial \rho}\right)_S\Big|_{\rho=\rho_0} \rho_1 = p_0 + v_\mathrm{s}^2 \rho_1 \,, \tag{2.7}$$

where the subscript S denotes constant entropy and v_s^2 has been introduced as the derivative of the pressure with respect to mass density at ρ_0. Later, we will recognise v_s as the isentropic speed of sound. From Eq. (2.7) we note the direct relation between the first-order perturbations of pressure and mass density $p_1 = v_\mathrm{s}^2 \rho_1$, allowing us to substitute terms of the first-order mass density. Doing this, and inserting the perturbation scheme Eq. (2.6) in the governing equations (2.3), we find to first order,

$$\rho_0 \partial_t \boldsymbol{v}_1 = -\boldsymbol{\nabla} p_1 + \eta \nabla^2 \boldsymbol{v}_1 + \beta_\mathrm{visc} \eta \boldsymbol{\nabla}(\boldsymbol{\nabla} \cdot \boldsymbol{v}_1) \,, \tag{2.8a}$$

$$\frac{1}{v_\mathrm{s}^2} \partial_t p_1 = -\rho_0 \boldsymbol{\nabla} \cdot \boldsymbol{v}_1 \,. \tag{2.8b}$$

We take time derivative of the mass continuity equation (2.8b), followed by insertion of the time derivative of the fluid velocity from Eq. (2.8a),

$$\partial_t^2 \rho_1 = v_\mathrm{s}^2 \nabla^2 \rho_1 - (1 + \beta_\mathrm{visc}) \eta \nabla^2 (\boldsymbol{\nabla} \cdot \boldsymbol{v}_1) \,. \tag{2.9}$$

To arrive at an equation for the pressure, we insert the divergence of the fluid velocity from Eq. (2.8b) into Eq. (2.9),

$$\frac{1}{v_\mathrm{s}^2} \partial_t^2 p_1 = \left(1 + \frac{(1 + \beta_\mathrm{visc})\eta}{\rho_0 v_\mathrm{s}^2} \partial_t\right) \nabla^2 p_1 \,. \tag{2.10}$$

In the inviscid case ($\eta = 0$), we recover the wave equation for the pressure, with a propagation velocity of v_s. Consequently, the perturbation pressure p_1 is readily interpreted as a sound wave, propagating with the isentropic speed of sound.

The fluid is mechanically actuated by the channel walls, which is attached to a piezo-electric element, driven by a AC voltage. The applied voltage is time-harmonic with frequency f, and angular frequency $\omega = 2\pi f$. The first-order fields are therefore also time-harmonic,

$$\boldsymbol{v}_1(\boldsymbol{r}, t) = \boldsymbol{v}_1(\boldsymbol{r})\, \mathrm{e}^{-\mathrm{i}\omega t} \,, \tag{2.11a}$$

$$\rho_1(\boldsymbol{r}, t) = \rho_1(\boldsymbol{r})\, \mathrm{e}^{-\mathrm{i}\omega t} \,, \tag{2.11b}$$

$$p_1(\boldsymbol{r}, t) = p_1(\boldsymbol{r})\, \mathrm{e}^{-\mathrm{i}\omega t} \,. \tag{2.11c}$$

Given this, all time derivatives ∂_t, can be replaced by a factor of $-\mathrm{i}\omega$ in Eq. (2.10), and we define a wavenumber as $k \equiv \omega / v_\mathrm{s}$

$$\nabla^2 p_1 = -\frac{1}{1 - \mathrm{i}\gamma} k^2 \, p_1 \,, \tag{2.12a}$$

$$\gamma = \frac{(1 + \beta_\mathrm{visc})\eta\omega}{\rho_0 v_\mathrm{s}^2} \,. \tag{2.12b}$$

The dimensionless quantity γ represents the viscous losses in the propagating sound wave. Operating the acoustofluidic device in the ultrasound regime, corresponds to frequencies in the MHz regime (2 MHz). Using this frequency, and parameters for water at ambient conditions, (see table A.1 in appendix A) one finds that $\gamma \approx 10^{-5} \ll 1$. This implies that the imaginary part of the pressure equation (2.12a) to a good approximation can be neglected. The physical interpretation is that ultrasonic waves in the MHz regime, to a good approximation propagate in bulk water without any losses. In this inviscid approximation ($\eta = 0$), we note how the structure of the pressure equation (2.12a) reduces to a Helmholtz equation

$$\nabla^2 p_1 = -k^2 p_1 \quad \text{for} \quad \eta = 0\,. \tag{2.13}$$

From Eq. (2.8a), we also note that neglecting viscosity and applying the time derivative $\partial_t \to -\mathrm{i}\omega$, leads to a simple relation between first-order fluid velocity and pressure

$$\boldsymbol{v}_1 = -\mathrm{i}\frac{1}{\rho_0 \omega}\boldsymbol{\nabla} p_1 \quad \text{for} \quad \eta = 0\,. \tag{2.14}$$

By neglecting effects of viscosity in the propagation of sound waves in the fluid, the relation between pressure and fluid velocity makes Eq. (2.13) the single governing partial differential equation for the acoustic fields (pressure and velocity). In chapter 3, we will define the geometry and relevant boundary conditions, allowing for determination of the explicit acoustic field. We mention that no account will be taken in this thesis for the varying temperature field that also will be present in the fluid [24]. A full thermo-acoustofluidic account is not an aim of this thesis, and we refer the reader to the work by Muller et *al.* [24, 25].

2.2.2 Second-order acoustic effects

Since all first-order fields are a direct response from the actuating ultrasound, all first-order fields inherit the harmonic time dependence from Eq. (2.11). For one full period $\tau = 2\pi/\omega$, we define the time-average of an arbitrary field $X(t)$ as

$$\langle X \rangle \equiv \frac{1}{\tau}\int_0^\tau \mathrm{d}t\, X(t)\,. \tag{2.15}$$

Because the average value of a harmonic function is zero, the time-average of any first-order field, is zero. Physically this result can be understood in the following way. Because we typically operate the ultrasound at MHz frequency, and the first-order oscillations are tiny, observing the first-order fields over the course of a few tens of µs or longer, will look virtually as if nothing is happening. However, if the perturbation scheme of Eq. (2.8), is derived to second order, products of first-order fields contribute, as their time-averaged values are non-zero, in analogy with e.g. $\langle \cos^2(\omega t) \rangle = 1/2$. In the next subsection we discuss two second-order effects that have non-zero time-averaged values, acoustic streaming and acoustic radiation force.

Acoustic streaming

One important second-order effect, arising from the acoustofluidic perturbation scheme to second-order is acoustic streaming. Acoustic streaming arise when including viscous stresses near a rigid wall, where no-slip boundary conditions are imposed [23]. As the velocity of the fluid has to go to zero on the wall, large shear stresses build up close to the wall in the so-called acoustic boundary layer. This is due to the driving oscillatory motion of the bulk fluid. The thickness

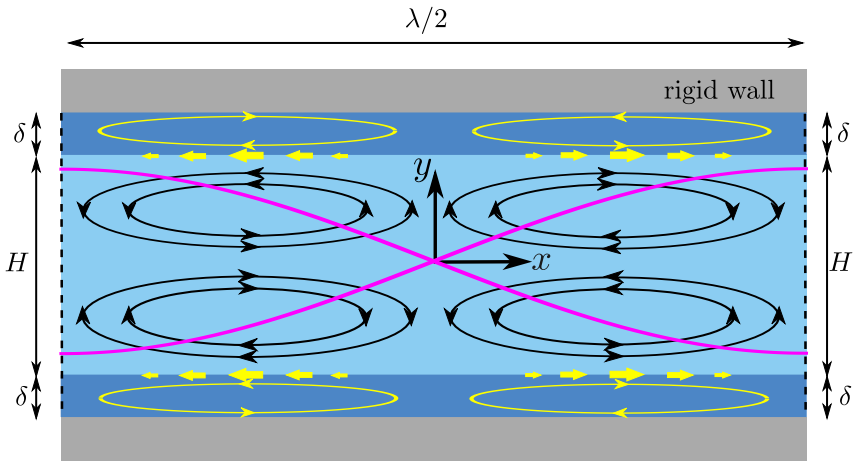

Figure 2.1: Sketch of Rayleigh-Schlichting streaming between infinite parallel plates and height H. A bulk sound pressure wave p_1 (magenta) is established in the bulk fluid (light blue). The sound wave gives rise to streaming rolls $\boldsymbol{v}_2$ (yellow) in the viscous boundary layer (dark blue) of thickness δ (not drawn to scale). This flow roll will in turn produce bulk flow rolls $\boldsymbol{v}_2$ (black) rotating in the opposite direction. The figure is adapted from [24].

δ of this boundary layer, depends only on the fluid viscosity η, mass density ρ and actuation frequency ω [23, 24]

$$\delta = \sqrt{\frac{2\eta}{\omega\rho}} \simeq 0.4\,\mu\text{m}\,, \tag{2.16}$$

where the value is calculated for water at ambient temperature, actuated at a frequency of $f = 2\,\text{MHz}$. The viscous boundary layer stresses can give rise to additional velocity fields, which in time-average are non-zero. These fields are called the acoustic streaming fields, or Rayleigh-Schlichting streaming [26, 27], and are found by calculating the second-order fluid velocity field $\boldsymbol{v}_2$ [24].

One example is for a bulk wave of wavelength $\lambda = 2\pi/k$ between infinite parallel plates, separated by a distance H, see figure 2.1. In the limit $\delta \ll H \ll \lambda$, Rayleigh and Schlichting showed that squeezed streaming rolls would occur within the boundary layer with height δ and width $\lambda/4 \gg \delta$, denoted by yellow in Fig. 2.1. Because these flow rolls are confined to the narrow viscous boundary layers, one can view the top of the flow roll facing the bulk fluid as an effective boundary condition for the bulk streaming velocity $\boldsymbol{v}_2^{\text{bulk}}$. In this sense, the horizontal velocity of this effective boundary condition, denoted by the yellow arrows, acts as a 'conveyor belt' that in turn drives a new flow roll in the bulk of the fluid (black), see Fig. 2.1. The effective boundary condition is found to be [23]

$$v_{x,2}(x) = \frac{3}{8}\frac{v_1^2}{v_\text{s}}\sin(2kx)\,, \tag{2.17}$$

where v_1 is the amplitude of the first-order oscillating velocity field. We will take the effective boundary condition velocity as a the typical streaming velocity $v_\text{str} = v_{x,2}$. Muller *et al.* [24] show in a numerical study that streamin0g effects are very dependent upon the detailed geometry, and the imposed boundary conditions. It is therefore difficult to make quantitative predictions about the streaming field for an arbitrary geometry.

Acoustic radiation force

Acoustic radiation force is another second order acoustic effect. This effect is of great interest in the scope of this thesis, as it is the driving mechanism for the dynamics of the suspended particles. The acoustic radiation force on a particle stems from the scattering of an incoming sound wave on the particle, thus transferring momentum from the wave to the particle. In the limit of weak scatterers, where the scattered field amplitude, are much smaller than the incoming field amplitude, closed form expressions can be found.

We assume a single compressible spherical particle of diameter $2a$ is suspended in an unbounded liquid. The particle and the liquid has mass density ρ_p and ρ_0, respectively, and compressibility κ_p and κ_0. A standing plane sound wave with wavelength $\lambda = 2\pi/k$ is established in the liquid, and thereby imposed on the particle.

To make analytical headway, we go to the Rayleigh limit, in which the particle is assumed to have a radius much smaller than the wavelength of the acoustic wave $a \ll \lambda$. Gor'kov [28] considers such a system for an arbitrary acoustic field $\{\boldsymbol{v}_1, p_1\}$ in the limit of an inviscid fluid. By considering the average flux of momentum through an arbitrary closed surface, Gor'kov shows how a non-zero time average force is exerted on the particle by the fluid. Since we are in the inviscid limit, Gor'kov finds that acoustic radiation force on the particle can be expressed in terms of an acoustic energy potential [28]

$$U_\mathrm{ac} = V_\mathrm{p}\left[\frac{f_1}{2}\kappa_0\left\langle p_1^2\right\rangle - \frac{3f_2}{4}\rho_0\left\langle\left|\boldsymbol{v}_1^2\right|\right\rangle\right], \tag{2.18}$$

where V_p is the particle volume, and f_1 and f_2 are the mono- and dipole-scattering coefficients, respectively. The coefficients stem from the multipole expansions of the scattered wave, and depend only on the material parameters of the particle and the liquid. Because we are in Rayleigh limit, higher order scattering terms, can be omitted [29]. From Eq. (2.18), the time-averaged acoustic radiation force is simply found by taking the gradient

$$\boldsymbol{F}_\mathrm{ac} = -\boldsymbol{\nabla} U_\mathrm{ac}\,. \tag{2.19}$$

In analogy with Fig. 2.1, a viscous boundary layer also forms around the spherical particle. This implies that at distances $\lesssim \delta$ from to the surface of the particle, viscosity will affect the flow around the sphere and modify the result by Gor'kov in inviscid limit of Eq. (2.18).

Viscous effects was taken into account by Settnes and Bruus [29]. For the case of standing waves, they found that the viscous corrections only enters in the scattering coefficients f_2, and introduces and imaginary $f_2 = f_2^\mathrm{Re} + f_2^\mathrm{Im}$. Settnes and Bruus finds [29]

$$f_1 = 1 - \frac{\kappa_\mathrm{p}}{\kappa_0}\,, \quad f_2^\mathrm{Re} = \mathrm{Re}\left[\frac{2\left[1-\Gamma(\delta/a)\right]\left(\dfrac{\rho_\mathrm{p}}{\rho_0}-1\right)}{2\dfrac{\rho_\mathrm{p}}{\rho_0}+1-3\Gamma(\delta/a)}\right], \tag{2.20a}$$

$$\text{with}\quad \Gamma(\delta/a) = -\frac{3}{2}\mathrm{Re}\left[1+\mathrm{i}\left(1+\frac{\delta}{a}\right)\right]\frac{\delta}{a}, \tag{2.20b}$$

where for $\Gamma = 0$ we recover the inviscid result by Gor'kov [28]. Furthermore, we note from Eq. (2.20b) that the viscous corrections are most pronounced for small particles $\delta \sim a$, and that the compressibilities enter only in the monopole coefficient f_1. The physical interpretation is that for the monopole term to give rise to a force, a difference in compressibility between particle and fluid must exist $\kappa_\mathrm{p} \neq \kappa_0$. The larger the contrast, the larger the force. Similarly, we note that the mass density and viscosity enters only in the dipole coefficient f_2^Re. Analogous to the

relative compressibility in f_1 we see that the larger the difference in mass density, the larger is the radiation force arising from the dipole term. It should be mentioned that no account has been taken in this treatment to include effects of thermal conductivity.

With the equations (2.18)-(2.20b), only explicit expressions for $\boldsymbol{v}_1$ and p_1 at the location of the particle, are needed to calculate the acoustic radiation force $\boldsymbol{F}_{\text{ac}}$ on a spherical particle subjected to a standing wave in the Rayleigh limit.

2.3 Effective viscosity and particle mobility

In the remaining part of this chapter, we leave the acoustofluidic theory, and return to the regime of low Reynolds number flows. In this context, we consider the acoustic fields $\boldsymbol{v}_1$ and p_1, as 'background fields' that only exists to supply the acoustic radiation force $\boldsymbol{F}_{\text{ac}}$, but does otherwise not interacting with particle and fluid dynamics. In what follows, we investigate some of the changes in the viscous hydrodynamic properties that arise in concentrated particle suspensions.

When a number of particles is suspended in a liquid, it is well known in hydrodynamics that the viscosity of the suspension changes [18, 30]. This phenomenon is well studied in sedimentation experiments [31] where a number of suspended particles, settles due to gravity at the bottom of the container over time. Sedimentation experiments are popular in this context, because they allow for simple ways to estimate the local particle concentration and sedimentation rate as function of starting concentration. Furthermore, as the fluid conveniently remains mostly at rest during the sedimentation, the theoretical treatment of the suspended particles can be greatly simplified.

Two different aspects of this phenomenon arise in particle suspensions. The first, called the *mobility* aspect affects individual particles, due to the nearby presence of other particles. More restrictive boundary conditions are imposed in the vicinity of the particle to represent the no-slip boundaries of the neighbouring particles. This introduces additional viscous stresses in the liquid, resulting in an altered drag force on the single particle. The second, called the *effective medium viscosity* aspect, is that the effective viscosity of the suspension as a whole, changes with the particle concentration, again due to additional viscous stresses.

The theoretical treatment of viscosity changes, depends highly upon for which concentration regime a solution is sought. Moreover, for a given regime of concentrations, many different approaches exists, using different model assumptions and results in different viscosity modifications. Some models are derived empirically, semi-empirically or analytically [30]. Therefore, no single method is commonly accepted as the best one in literature. Due to this, it is important to bear in mind that these models are estimates at best, as to how the viscosity changes as function of particle concentration. As we focus on highly concentrated systems ($\phi > 0.01$), we will here review one of the models describing viscosity changes in highly concentrated regimes. The model of choice is called the *cell model* or the *free surface model*, and is developed by Happel and Brenner in [18] (see section 8-4 and 9-4). Before separately dealing with these two aspects, we will make some general remarks about the so-called cell model.

2.3.1 The cell model

In the *cell* model (also called the *free surface* model), one assumes that the particles and the host liquid can be approximated by identical unit cells that is repeated throughout the liquid container. For simplicity, we assume the cell to be spherical, consisting of two concentric spheres, with inner radius a, representing the particle, and outer radius b, representing the neighbouring

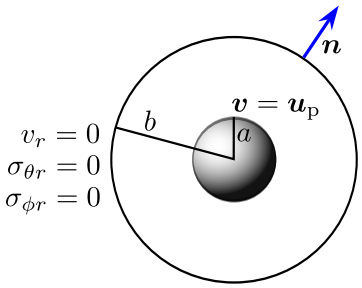

Figure 2.2: Principal sketch of the cell model by Happel and Brenner [18, 32]. Inner particle radius a, where a no-slip boundary conditions between particle and liquid is imposed. Outer cell boundary radius b, where no normal flow and no tangential stress boundary conditions are imposed.

cells. This is sketched in Fig. 2.2.

The boundary of the cell at $r = b$ is assumed to be frictionless, thus the entire disturbance due to the particle is confined to the fluid within the cell. Relating the particle volume concentration ϕ to the volumes of the cell and the particle we find

$$\phi = \frac{V_\mathrm{p}}{V_\mathrm{cell}} = \left(\frac{a}{b}\right)^3 . \tag{2.21}$$

Assuming a steady creeping flow, the governing equations (2.3a) and (2.3b) reduce to the Stokes Eq., and the incompressible mass continuity equation

$$\eta \nabla^2 \boldsymbol{v} = \boldsymbol{\nabla} p \,, \tag{2.22a}$$

$$\boldsymbol{\nabla} \cdot \boldsymbol{v} = 0 \,. \tag{2.22b}$$

The spherical particle centred in origo with radius a, gives rise to a no-slip boundary condition. Assuming that the particle moves with velocity $\boldsymbol{u}_\mathrm{p}$, the boundary condition becomes

$$\boldsymbol{v} = \boldsymbol{u}_\mathrm{p} \quad \text{for} \quad r = a \,. \tag{2.23}$$

The cell boundary was assumed frictionless, implying that tangential stresses vanish

$$\left.\begin{aligned} \sigma_{\theta r} &= \eta \left(\frac{1}{r}\partial_\theta v_r + \partial_r v_\theta - \frac{v_\theta}{r} \right) = 0 \\ \sigma_{\phi r} &= \eta \left(\frac{1}{r \sin\theta}\partial_\phi v_r + \partial_r v_\phi - \frac{v_\phi}{r} \right) = 0 \end{aligned}\right\} \quad \text{for} \quad r = b \,, \tag{2.24}$$

where (r, θ, ϕ) are the spherical co-ordinates, and $\boldsymbol{\sigma}$ is the Cauchy stress tensor, following the convention given in [33]. Lastly, we require that no fluid enters or leaves the cell

$$v_r = 0 \quad \text{for} \quad r = b \,. \tag{2.25}$$

In the light of this boundary condition, we consider for a moment the physical correctness of this demand on the fluid velocity. As an example we imagine pressing some fluid through a fixed assemblage of spheres. In such an experiment, we we reason that fluid must enter and leave the cells in some way, thereby violating the boundary condition in Eq. (2.25). This physical inconsistency of the chosen boundary condition for the cell model will be discussed at a later point in Section 7.3.2.

Solving the Stokes equation in spherical co-ordinates

To solve this problem in spherical co-ordinates, we employ Lambs general solution to the creeping flow problem [34]

$$\boldsymbol{v} = \sum_{n=-\infty}^{\infty} \left(\boldsymbol{\nabla} \times (\boldsymbol{r} f_n) + \boldsymbol{\nabla} g_n + \frac{n+3}{2\eta(n+1)(2n+3)} r^2 \boldsymbol{\nabla} p_n - \frac{n}{\eta(n+1)(2n+3)} \boldsymbol{r} p_n \right) . \quad (2.26a)$$

$$p = \sum_{n=-\infty}^{\infty} p_n \, , \quad (2.26b)$$

where f_n, g_n and p_n, are solid spherical harmonic functions. To find the solution to the particular flow problems, boundary conditions are later used to determine the various coefficients of the harmonic terms. For more details, see appendix B.

2.3.2 Change of particle mobility

In the first aspect we look at the change of the dynamics of the single particle. The question of interest is how the drag force on the particle $\boldsymbol{F}_\mathrm{d}$ deviates from the usual Stokes drag force. The particle moves with velocity $\boldsymbol{u}_\mathrm{p} - \boldsymbol{v}$ relative to the fluid, and the drag force exerted on it from liquid is

$$\boldsymbol{F}_\mathrm{d} = -\frac{6\pi\eta a}{\chi(\phi)} \left(\boldsymbol{u}_\mathrm{p} - \boldsymbol{v} \right) . \quad (2.27)$$

Here $\chi(\phi)$ is introduced as a dimensionless factor which we call the *relative mobility*, and is a function of the local volume concentration ϕ. Since we assume constant force equilibrium on the microparticles between the acoustic radiation force and the drag force $\boldsymbol{F}_\mathrm{d} = -\boldsymbol{F}_\mathrm{ac}$. Therefore, we can instead formulate the change of the particle mobility, when subjected to an external force

$$\boldsymbol{u}_\mathrm{p} - \boldsymbol{v} = \underbrace{\frac{\chi(\phi)}{6\pi\eta a}}_{\text{mobility}} \boldsymbol{F}_\mathrm{ac} \, . \quad (2.28)$$

To derive the drag force on the particle, it is necessary to first determine the fluid velocity $\boldsymbol{v}$ and pressure p. To solve for these fields Happel and Brenner applies the boundary conditions in Eqs. (2.23)-(2.25) and finds that only harmonic functions of order -2 and 1 are retained in the specific solution. For details, we refer the reader to appendix B.1. To calculate the force on a sphere, one must integrate the Cauchy stress tensor over the surface of the sphere

$$\boldsymbol{F}_\mathrm{d} = \int_\mathrm{sph} \mathrm{d}A \; \boldsymbol{\sigma} \cdot \boldsymbol{n} \, . \quad (2.29)$$

By performing this integral for spherical harmonic functions, Happel and Brenner finds the modified drag force (see appendix B.1),

$$\boldsymbol{F}_\mathrm{d} = -6\pi\eta a \left[\frac{2}{3} \frac{3 + 2\phi^{5/3}}{2 - 3\phi^{1/3} + 3\phi^{5/3} - 2\phi^2} \right] \left(\boldsymbol{u}_\mathrm{p} - \boldsymbol{v} \right) , \quad (2.30)$$

from which we identify the relative particle mobility as

$$\chi(\phi) = \frac{3}{2} \frac{2 - 3\phi^{1/3} + 3\phi^{5/3} - 2\phi^2}{3 + 2\phi^{5/3}} \, . \quad (2.31)$$

We note that $\chi(\phi)$ reduces to 1 for $\phi = 0$, which is expected in the dilute limit. In Fig. 2.3(a) we have plotted the relative particle mobility $\chi(\phi)$ over several decades of volume concentration ϕ. Note that the particle mobility decreases rapidly for increasing volume concentration ϕ.

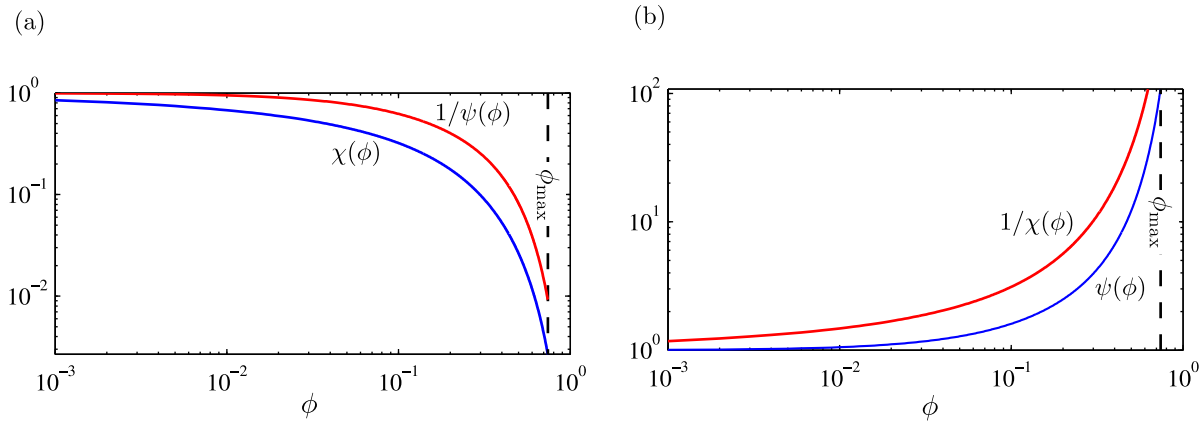

Figure 2.3: Plots of the relative particle mobility $\chi(\phi)$ in (a) and the relative effective medium viscosity $\psi(\phi)$ (b). Note that the functions resemble to have an inverse relationship.

2.3.3 Change of effective medium viscosity

For the other aspect , namely the change of *effective medium viscosity*, we must treat the flow problem in a slightly different way to reach an analytical solution. This estimate uses the idea of the cell model described previously and was derived by Happel [32] in 1957. The basic idea is that the mechanical work W performed by the surroundings on the boundary of the cell at $r = b$, must dissipate over time inside the cell. All dissipative losses are assumed to be due to friction in the fluid, i.e. viscous losses. As we assume the system to be in steady state, the work put in per time $\mathrm{d}W/\mathrm{d}t$, must be dissipated by viscosity by the same rate. This suggests that the input power is proportional to the effective viscosity

$$\frac{\mathrm{d}W}{\mathrm{d}t} \propto \eta_{\mathrm{eff}} \,. \tag{2.32}$$

In analogy with the relative mobility function $\chi(\phi)$ defined in the previous section, we define the *relative effective medium viscosity*

$$\psi(\phi) \equiv \frac{\eta_{\mathrm{eff}}}{\eta} \,. \tag{2.33}$$

The total velocity and pressure fields inside the cell are assumed to consist of an undisturbed background field (0), without the particle. Plus a disturbance field (1) that serves as a correction to the fields when the particle is placed in the cell

$$\boldsymbol{v} = \boldsymbol{v}^{(0)} + \boldsymbol{v}^{(1)} \,, \quad p = p^{(0)} + p^{(1)} \,. \tag{2.34}$$

The undisturbed field, consists of a shearing motion, with constant y-derivative of the fluid velocity in the x-direction $q = \partial_y v_x^{(0)}$. The background field is

$$(v_x^{(0)},\, v_y^{(0)},\, v_z^{(0)}) = \frac{q}{2}\,(y,\, x,\, 0) \,. \tag{2.35}$$

The purpose of the background field is not in itself to uphold the boundary conditions given in Eqs. (2.23) and (2.24). But primarily to facilitate a closed solution to the full disturbed flow problem, and secondly solve the linear governing Eqs. (2.22) on their own.

Disturbance field

The sphere of radius a is again placed in origo, but does not move $\boldsymbol{u}_\mathrm{p} = \mathbf{0}$. Because the background field has a non-zero fluid velocity at the particle surface at $r = a$, the disturbance field must exactly cancel this velocity to satisfy the no-slip condition. From Eq. (2.35) we get

$$(v_x^{(1)},\, v_y^{(1)},\, v_z^{(1)}) = -\frac{q}{2}\,(y,\, x,\, 0) \quad \text{for} \;\; r = a\,. \tag{2.36}$$

Furthermore, the disturbance field must satisfy the boundary condition of zero tangential stress and zero normal fluid velocity at the boundary of the cell, as given in Eqs. (2.24) and (2.25).

Applying these boundary conditions, Happel finds [32] $f_n = 0$ for all n, and retain harmonics of order -3 and +2, for which he also finds the coefficients (see Eqs. (9)-(12) in Happel [32])

Next, the work per time put into the cell at the boundary can be calculated as an integral over the cell surface, using the *total* fields

$$\frac{\mathrm{d}W}{\mathrm{d}t} = \oint_\mathrm{cell} \boldsymbol{v}\cdot\boldsymbol{\sigma}\cdot\mathrm{d}\boldsymbol{A} = \int_0^{2\pi}\mathrm{d}\phi\int_0^{\pi}\mathrm{d}\theta\; b^2\sin\theta \begin{pmatrix} v_r^{(0)} \\ v_\theta^{(0)} + v_\theta^{(1)} \\ v_\phi^{(0)} + v_\phi^{(1)} \end{pmatrix} \cdot \begin{pmatrix} \sigma_{rr}^{(0)} + \sigma_{rr}^{(1)} \\ \sigma_\theta^{(0)} \\ \sigma_\phi^{(0)} \end{pmatrix} \tag{2.37}$$

where we recall that $v_r^{(1)}|_{r=b}$ is zero by virtue of the imposed boundary condition. Expressing the result of the integral in terms of the particle volume concentration ϕ, Happel finds

$$\frac{\mathrm{d}W}{\mathrm{d}t} = V_\mathrm{cell}\, q\, \eta \underbrace{\left[1 + \frac{55}{10}\phi\left(\frac{4\phi^{7/3} + 10 - \frac{84}{11}\phi^{2/3}}{10(1-\phi^{10/3}) - 25\phi(1-\phi^{4/3})}\right)\right]}_{\eta_\mathrm{eff}}, \tag{2.38}$$

from which the relative effective medium visocosity is easily identified as

$$\psi(\phi) = \left[1 + \frac{55}{10}\phi\left(\frac{4\phi^{7/3} + 10 - \frac{84}{11}\phi^{2/3}}{10(1-\phi^{10/3}) - 25\phi(1-\phi^{4/3})}\right)\right] \tag{2.39}$$

We note that $\psi(\phi)$ reduces to 1 for $\phi = 0$. This corresponds to the viscous dissipation of an infinitely dilute particle suspension, i.e. the dissipation rate at unmodified fluid viscosity $\eta = \eta_\mathrm{eff}$. In Fig. 2.3(b) we have plotted $\psi(\phi)$ over several decades of ϕ, and note that the effective viscosity increases by almost a factor of 100 for very concentrated suspensions. Moreover, it is worthy of note that $\chi(\phi)$ and $\psi(\phi)$ share an almost inverse relationship, see Fig. 2.3. With the results of relative particle mobility $\chi(\phi)$ and effective viscosity $\psi(\chi)$ found in Eqs. (2.31) and (2.39), we conclude our investigation of viscosity changes in particle suspensions and turn to the issue of model building, with the results derived throughout this chapter.

2.4 Concluding remarks

In this chapter we have outlined the fundamental equations, governing the behaviour of the particles and the liquid, assuming particles can be described by a continuous concentration field. We have applied the governing equations in two areas. First, by deriving the governing equations for the first-order acoustic fields in the inviscid limit ($\eta = 0$) using perturbation theory.

We briefly discussed two important second order effects, namely the acoustic streaming and the acoustic radiation force $\boldsymbol{F}_{\mathrm{ac}}$. In the other area, we applied governing equations in reviewing a model for calculating the enhanced drag forces on the particles $\boldsymbol{F}_{\mathrm{d}}$ and effective medium viscosity η_{eff}, when a number of particles are suspended in the liquid, which give rise to additional viscous stresses.

With these two main results, we are ready to construct a physical model, from which we can derive the particle suspension dynamics.

Chapter 3

Model system

The principle aim of this thesis-work is calculate and predict the behaviour of microparticle suspensions undergoing acoustophoresis. Ideally, this would involve solving for the positions of *all* particles, subject to forces from both the induced ultrasound as well as drag from the surrounding liquid. This while simultaneously solving the Navier-Stokes equation for the host liquid, satisfying both the no-slip conditions of the channel walls and the surfaces of all particles. This ideal and non-simplifying approach is extremely difficult and infeasible. We therefore make a series of simplifications in order to make theoretical progress. To do this, we first define the outer circumstances: geometry, experimental system, etc. Using the outer circumstances of the physical system, we define a set a set of physically reasonable assumptions, essentially defining our model system. These assumptions will allow the formulation of a set of governing equations and corresponding boundary conditions, for which numerical solutions can be found. As we go along, we physically motivate the implementation of several hydrodynamic particle-particle interaction mechanisms, implementing them step by step.

3.1 System description and geometry

The model system consists of a long straight rectangular silicon microchannel, with an attached glass lid. The channel has width W, height H and length L. Typically, the width W of the channel is sub millimetre size, where the total channel length L can be a few centimetres in length [8, 35]. In Fig. 3.1 we sketch some length ℓ of the channel. Attached to the channel is a piezoelectric transducer that is operated harmonically with an AC voltage, typically of the order 1-10 V [36]. The transducer mechanically actuates the channel, which in turn causes the liquid to oscillate. This can cause an acoustic resonance of the liquid [20] that gives rise to a standing pressure wave, oscillating at MHz frequency, as seen by the crossing magenta lines in Fig. 3.1. Inside the channel are a number of micrometre sized particles with typical diameters $2a$ from 1 to 20 µm which are suspended in a Newtonian liquid, e.g. water. From scattering of the oscillating sound waves, the particles feel the acoustic radiation force $\boldsymbol{F}_{\mathrm{ac}}$ discussed in Section 2.2.2.

3.1.1 Computation domain

Because the channel is chosen to have an aspect ratio of approximately $H \approx \frac{1}{2}W$, and we primarily aim to describe behaviour along the length of the channel, we neglect any variations along the height of the channel. Thus making the computational domain two-dimensional. For all calculations, we assume the height co-ordinate to be in the center plane, halfway between the

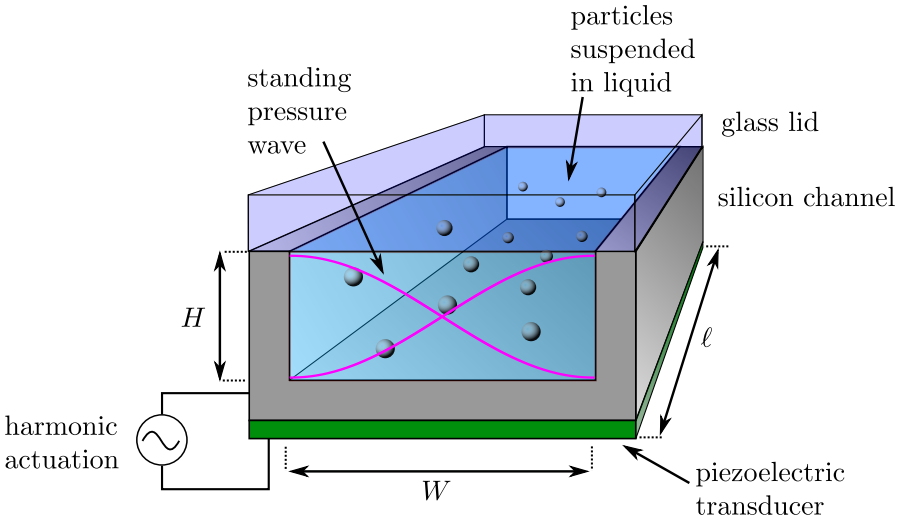

Figure 3.1: Sketch of some length ℓ of the acoustofluidic channel used in experiments, used as basis for derivations throughout the thesis. The width W of the channel is sub millimetre size, where the full channel length L can be a few centimetres [8, 35]. The mechanical actuation is realised with a piezoelectric transducer, by applying a harmonic AC voltage. The mechanical actuation can give rise to an acoustic resonance in the fluid which produces an oscillating standing pressure wave, shown by the crossing magenta lines. By scattering of these sound waves the particles feel an acoustic radiation force $\boldsymbol{F}_{\text{ac}}$.

channel bottom and the glass lid, such that we minimize wall effects from the top and bottom walls. To simplify further we assume all behaviour to be periodic with length ℓ, confining the computation domain Ω to have width W and length ℓ. The choice of periodicity introduces symmetry boundary conditions on some of the physical quantities. In Fig. 3.2 the computationn Ω is sketched.

Boundary conditions

Because the walls in our chosen systems, consists of silicon and glass, it is reasonable to approximate the walls to be rigid. Physically this means that no displacement will be observed when the wall is subjected to a pressure p. Instead, pressure can build up at the wall. For the fluid velocity $\boldsymbol{v}$, the wall introduces the usual no-slip condition. Lastly, no particles can enter or leave through the wall, which implies a no-flux boundary condition for the particles. The wall boundary conditions for the respective fields become

$$\text{hard wall BC:} \quad \left.\begin{aligned} \boldsymbol{\nabla} p \cdot \boldsymbol{n} &= 0 \\ \boldsymbol{v} &= \boldsymbol{0} \\ \boldsymbol{J}_{\text{p}} \cdot \boldsymbol{n} &= 0 \end{aligned}\right\} \quad \text{for} \quad \boldsymbol{r} \in \partial\Omega_{\text{wall}} \tag{3.1}$$

Because we have assumed identical cells of channel length ℓ, no fluid nor particles can flow from one cell to the other, implying that all normal components of the fluid velocity $\boldsymbol{v}$ and particle current density $\boldsymbol{J}_{\text{p}}$ mush vanish at symmetry boundaries. Furthermore, a standard condition at symmetry lines requires all tangential stresses in the fluid to vanish, else the symmetry line would deform.

$$\text{periodic BC:} \quad \left.\begin{aligned} \boldsymbol{v} \cdot \boldsymbol{n} &= 0 \\ \boldsymbol{J}_{\text{p}} \cdot \boldsymbol{n} &= 0 \\ \boldsymbol{\sigma} \cdot \boldsymbol{n} - (\boldsymbol{n} \cdot \boldsymbol{\sigma} \cdot \boldsymbol{n})\boldsymbol{n} &= \boldsymbol{0} \end{aligned}\right\} \quad \text{for} \quad \boldsymbol{r} \in \partial\Omega_{\text{sym-bdy}}\,. \tag{3.2}$$

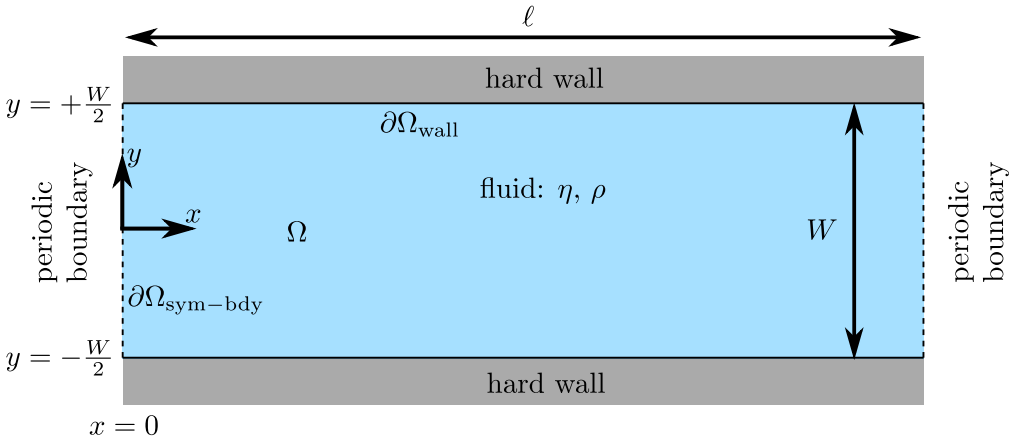

Figure 3.2: Top view: Sketch of the two-dimensional computational domain Ω, consisting of the fluid with viscosity η and mass density ρ. The horizontal boundaries consists of hard walls (grey), and vertical periodic boundaries (dashed lines) to the sides where the micro channel continues.

We have now defined the model system consisting of the geometry and the resulting boundary conditions. Thus, we are now ready to find the specific acoustic radiation force $\boldsymbol{F}_{\text{ac}}$.

3.2 Acoustic fields in the liquid

Starting out with no particles in the liquid, we derived in Section 2.2.1 that the fluid velocity and pressure could be calculated with first-order perturbation theory. Because the piezoelectric tranducer is actuated with an AC voltage of angular frequency ω, harmonic time dependence of all fields was assumed. This allowed describing the acoustic fields by finding only the first order pressure p_1. In the inviscid limit, the governing equation for the pressure p_1 was shown to be a Helmholtz equation (2.13) with wavenumber k. To solve the Helmholtz Eq. (2.13), we split up the wavenumber k in the x and y-direction

$$k^2 = k_x^2 + k_y^2 \,. \tag{3.3}$$

This allows for solving the Helmholtz equation for the pressure p_1 with a simple product of sines

$$p_1(x, y, t) = p_1^{\text{a}} \sin(k_x x) \sin(k_y y + \Theta)\, \mathrm{e}^{-\mathrm{i}\omega t} \,, \tag{3.4}$$

where p_1^{a} is the amplitude of the pressure field, later to be determined, and Θ is the phase of the pressure wave. We note that the pressure p_1 has the form of a standing wave, which decomposed in the x- and y-direction, have wavelengths $\lambda_x = 2\pi/k_x$ and $\lambda_y = 2\pi/k_y$. We define the ratio between the wavelengths as

$$\boxed{\beta \equiv \frac{\lambda_y}{\lambda_x} = \frac{k_x}{k_y} \,,} \tag{3.5}$$

which will turn out to be an important parameter. In an acostofluidic setup identical to the one modelled in this thesis, Barnkob *et al.* [37] also proposed this form of the first-order pressure p_1.

To satisfy the hard wall boundary condition Eq. (3.1), we see that the pressure p_1 is only allowed certain wavenumbers k_y. In the transverse direction across the width W of the channel,

the pressure must consist of a multiple of half wavelengths $\lambda_y/2$, corresponding to the allowed wavemumbers

$$k_y = n\frac{\pi}{W}\,, \quad n = 1,\, 2,\, 3,\, \ldots\,, \tag{3.6}$$

with the corresponding phase

$$\Theta = \frac{\pi}{2} \;\text{ for }\; n = 0, 2, 4, \ldots \quad \text{and} \quad \Theta = 0 \;\text{ for }\; n = 1, 3, 5, \ldots \tag{3.7}$$

The y-dependence of pressure p_1 in the transverse direction was largely validated by Augustsson *et al.* [36, 37]. They showed that one standing half wave across the width of the channel to be experimentally stable over time and reproducible. For all the following calculations, we will assume this type of pressure p_1 with wavenumber $k_y = \pi/W$ and phase $\Theta = 0$. A sketch of the one half-wave standing pressure wave p_1 is shown Fig. 3.1, denoted by the magenta crossing lines.

For the lateral (x) direction, Augustsson *et al.* found the pattern of p_1 to be irregular, with no one single value for the lateral wavelength λ_x. However, as with the transverse pressure characterization, Augustsson *et al.* showed the lateral variations to also be stable over time and reproducible. The length scale of the lateral variations, was found to span from a few channel widths W, up to around $20W$. No clear explanation is had for the irregular lateral pressure variations as this could have many sources: imperfect channel variations, inhomogeneous mechanical actuation, temperature gradients over the chip, etc.

To make theoretical headway we neglect the irregularities and choose a lateral wavelength of $\lambda_x = 3\lambda_y$ implying a value of $\beta = \frac{1}{3}$. We choose this value because it gives reasonable lateral modulation of the acoustic fields and is realistic to realise experimentally [36].

First-order fluid velocity $\boldsymbol{v}_1$

Using the simple relation between first-order fluid velocity $\boldsymbol{v}_1$ and pressure p_1 in Eq. (2.14) we get from Eq. (3.4)

$$\boldsymbol{v}_1(x, y, t) = -\mathrm{i}\frac{p_1^{\mathrm{a}}}{\rho_0\omega}\left[k_x \cos(k_x x)\sin(k_y y)\boldsymbol{e}_x + k_y \sin(k_x x)\cos(k_y y)\boldsymbol{e}_y\right] \mathrm{e}^{-\mathrm{i}\omega t}\,. \tag{3.8}$$

We note that Eq. (3.8) is complex-valued, and one should take the real part of Eq. (3.8) to find the physical part of the first-order velocity. Strictly speaking, the first-order velocity fields $\boldsymbol{v}_1$, does not satisfy the symmetry boundary conditions of Eq. (3.2) of no normal fluid velocity $\boldsymbol{v}_1 \cdot \boldsymbol{n} = 0$. However, since the acoustic fields are minute oscillations happening typically at MHz frequency, no net fluid enters or leaves the boundary in time average. In this context, we view the acoustic fields as background fields consisting of minute oscillations that serve only as the driving force for the dynamics of the suspended particles.

3.2.1 Acoustic resonances and viscous dissipation

In the above approach to finding the acoustic fields, no account was taken for viscosity which implies zero losses of mechanical energy. However, as the piezo-electric transducer is continuously delivering mechanical energy to the liquid a steady state, due to dissipation, must at some point be reached. We call the density of the mechanical in the liquid the *acoustic energy density* E_{ac} and it manifests as increasingly higher amplitudes of the fluid velocity $\boldsymbol{v}_1$ and pressure p_1. At resonance, a peak value for E_{ac} is reached, and the condition for resonance is exactly that of multiple of standing half-waves across the channel width W, corresponding to the allowed

wave numbers in Eq. (3.6). The physical interpretation of the resonance is that the propagation time for the sound wave across the channel, must corresponds to multiple of half wavelengths. Because acoustofluidic channel widths are typically sub millimetre size [8, 35],and the isentropic speed of sound in water is $v_\mathrm{s} \approx 1500\,\mathrm{m/s}$, the resonance frequencies often lies in the MHz range.

Muller *et al.* [22] studied the effect of including viscosity in finding the first order fields $\boldsymbol{v}_1$ and p_1. It was found that the inviscid description presented above, deviates only significantly from the viscous account close to the wall, in the viscous boundary layer. For our system, we found in Section 2.2.2 that this layer extends $\delta = 0.4\,\mu\mathrm{m}$ from the channel walls, making the inviscid ($\eta = 0$) description of the acoustic fields an excellent approximation for our purposes.

3.3 Acoustic radiation force field

In order to identify the specific time averaged acoustic radiation force $\boldsymbol{F}_\mathrm{ac}$ discussed in Section 2.2.2, we use the result by Settnes and Bruus [29], given in Eqs. (2.18)-(2.20b). We introduce the angle θ between $\boldsymbol{e}_x$ and $\boldsymbol{k}$

$$\cos(\theta) = \frac{k_x}{k}\ , \quad \sin(\theta) = \frac{k_y}{k}\ . \tag{3.9}$$

By taking the time averages of the pressure p_1 and velocity $\boldsymbol{v}_1$ in Eqs. (3.4) and (3.8), and inserting them in the expression for U_ac in Eq. (2.18), we find

$$\begin{aligned} U_\mathrm{ac} = 3V_\mathrm{p}\frac{(p_1^\mathrm{a})^2}{4\rho_0 v_\mathrm{s}^2}\Bigg\{ &\frac{1}{3}f_1 \sin^2(k_x x)\sin^2(k_y y) \\ &-\frac{1}{2}f_2^\mathrm{Re}\left[\cos^2(\theta)\cos^2(k_x x)\sin^2(k_y y) + \sin^2(\theta)\sin^2(k_x x)\cos^2(k_y y)\right]\Bigg\}. \end{aligned} \tag{3.10}$$

Part of the pre-factor is recognised as the acoustic energy density [11]

$$E_\mathrm{ac} = \frac{(p_1^\mathrm{a})^2}{4\rho_0 v_\mathrm{s}^2}\,, \tag{3.11}$$

which typically for acoustofluidic devices has values of the order 10 - 100 $\mathrm{J/m^3}$ [11]. To arrive at the acoustic radiation force, we take the gradient $\boldsymbol{F}_\mathrm{ac} = -\boldsymbol{\nabla} U_\mathrm{ac}$ and get

$$\begin{aligned} \boldsymbol{F}_\mathrm{ac}(\boldsymbol{r}) = 3V_\mathrm{p}E_\mathrm{ac}k_y\Bigg\{ & \\ -\beta\sin(2k_x x)&\left[\frac{1}{3}f_1\sin^2(k_y y) + \frac{1}{2}f_2^\mathrm{Re}\left\{\cos^2(\theta)\sin^2(k_y y) - \sin^2(\theta)\cos^2(k_y y)\right\}\right]\boldsymbol{e}_x \\ -\sin(2k_y y)&\left[\frac{1}{3}f_1\sin^2(k_x x) - \frac{1}{2}f_2^\mathrm{Re}\left\{\cos^2(\theta)\cos^2(k_x x) - \sin^2(\theta)\sin^2(k_x x)\right\}\right]\boldsymbol{e}_y\Bigg\}. \end{aligned} \tag{3.12}$$

We recall from Section 2.2.2 that f_1 and f_2^Re is given in terms of material parameters, see Eq. (2.20). We note from Eq. (3.12) that the acoustic radiation force in the lateral direction $F_{\mathrm{ac},x}$, scales with $\beta = \frac{1}{3}$, which implies that we expect effects in the lateral direction to be less pronounced. In Fig. 3.3, a plot is shown of the radiation force $\boldsymbol{F}_\mathrm{ac}$, where the magnitude denoted the color and the arrows denote the direction. We note that the maximum amplitude is found at the central lateral co-ordinate $x = \frac{1}{2}W/\beta$. This will only be the case for $\beta < 1$, which implies for

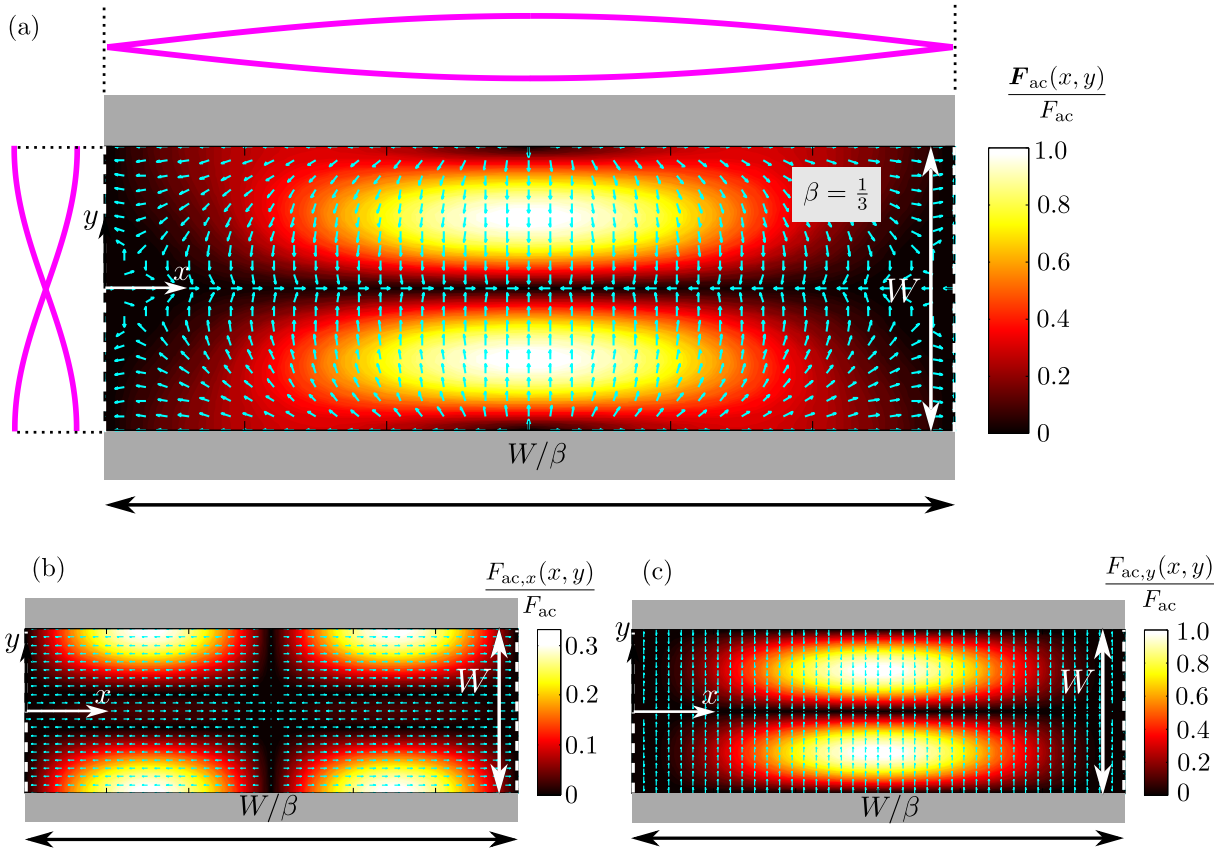

Figure 3.3: Vector plots of the acoustic force field $\boldsymbol{F}_{\mathrm{ac}}$, from Eq. (3.12), plotted in terms of the force amplitude F_{ac} in Eq. (3.13). The blue arrows denote the direction of the force, and the color denotes the magnitude. The grey bars mark the channel walls, and the periodic boundaries are denoted by dashed lines. The magenta lines denote the standing pressure waves p_1 in the channel.(a) Full vector field $\boldsymbol{F}_{\mathrm{ac}}$. (b) x-component of field $F_{\mathrm{ac},x}$ (c) y-component of field $F_{\mathrm{ac},y}$.

the angle $\frac{\pi}{4} < \theta \leq \frac{\pi}{2}$. Under these conditions, we find the maximum amplitude of the acoustic radiation force, by inserting $x = \frac{1}{2}W/\beta$ in Eq. (3.12)

$$F_{\mathrm{ac}} = 3V_{\mathrm{p}}E_{\mathrm{ac}}k_y\Phi_{\mathrm{2D}}\,, \tag{3.13}$$

where we have defined Φ_{2D} as the pseudo 'two-dimensional' acoustic contrast factor

$$\Phi_{\mathrm{2D}} = \frac{1}{3}f_1 + \frac{1}{2}f_2^{\mathrm{Re}}\sin^2(\theta) \quad \text{for} \quad \frac{\pi}{4} < \theta \leq \frac{\pi}{2}\,. \tag{3.14}$$

Because the acoustic radiation force is the driving mechanism for the particle dynamics, we will use the force amplitude F_{ac} as the characteristic force on the particles $F^* = F_{\mathrm{ac}}$. In Fig. 3.3, a plot of the acoustic radiation force $\boldsymbol{F}_{\mathrm{ac}}$ from Eq. (3.12) is shown.

The acoustic contrast factor

An important concept to touch upon, is that of the acoustic contrast factor, which was defined in its pseudo 'two-dimensional' form in Eq. (3.14). In the one dimensional case of a standing half-wave across the channel width, we have no modulation in the lateral direction of the channel. In this case, we have that $k_x = 0$ which implies $\beta \to 0$ and $\sin^2(\theta) \to 1$. In this case we recover the regular acoustic contrast factor $\Phi = \frac{1}{3}f_1 + \frac{1}{2}f_2^{\mathrm{Re}}$ [29]. This factor expresses how sound waves

scatter on the particles compared to the suspending medium. For acoustically hard particles ($\Phi > 0$), the sound waves scatters 'harder' on the particles compared to the liquid, and the radiation force drives the particles towards the pressure nodes, see Fig. 3.3. And vice versa for acoustically soft particles ($\Phi < 0$).

In this thesis, we model a system of polystyrene particles in water at ambient temperature. Inserting the mass densities and compressibilities of water and polystyrene given in Table A.1, we find the acoustic contrast factor from Eq. (2.20) as $\Phi = 0.165$. Because we have chosen $\beta = 1/3$, the angle $\theta = 1.249$, which means that the 'two-dimensional' contrast factor in this case is $\Phi_{2D} = 0.163$. This implies that the particles will be attracted towards the pressure nodes in the system.

3.4 Single particle dynamics

Having derived the acoustic radiation force $\boldsymbol{F}_{\mathrm{ac}}$ in the previous section, we can now explore the resulting particle dynamics from this driving force.

First we consider the dilute limit, where only a few particles are suspended in the liquid, allowing us, at first, to neglect interaction effects. We therefore look at the motion of one single particle with diameter $2a$, and mass density ρ_{p}. We assume the particle to be suspended in quiescent liquid ($\boldsymbol{v} = \boldsymbol{0}$), being initially at rest at some co-ordinate

$$\boldsymbol{r}_{\mathrm{p}} = (x_0, y_0)\ , \quad \mathrm{d}_t \boldsymbol{r}_{\mathrm{p}} = \boldsymbol{u}_{\mathrm{p}} = \boldsymbol{0} \quad \text{for} \ \ t = 0\,. \tag{3.15}$$

Next, we imagine the ultrasound is swicthed on at $t = 0$ which we approximate to be established instantaneously. In the experiment, the ultrasonic resonance is established after[1] ~ 0.3 ms [37]. We neglect this build-up time.

As the particle begins to move due to the acoustic radiation force $\boldsymbol{F}_{\mathrm{ac}}$, the liquid acts on the particle with an equal and opposing Stokes drag force $\boldsymbol{F}_{\mathrm{d}}$. The two forces will quickly balance, resulting in a steady particle speed $\boldsymbol{u}_{\mathrm{p}}$ which is exactly the *acoustophoretic particle migration*. This has been sketched in figure 3.4. Typical acoustophoretic speeds for micron sized particles in water is of the order $u_{\mathrm{p}} \sim 1$ mm/s, and lower [36].

Governing equation for single particle dynamics

The equation of motion for the particle is given by Newtons second law Eq. (2.1), which becomes

$$\begin{aligned} m_{\mathrm{p}} \mathrm{d}_t^2 \boldsymbol{r}_{\mathrm{p}} &= \boldsymbol{F}_{\mathrm{ac}} + \boldsymbol{F}_{\mathrm{d}} \\ &= \boldsymbol{F}_{\mathrm{ac}} - 6\pi\eta a \boldsymbol{u}_{\mathrm{p}}\,, \end{aligned} \tag{3.16}$$

where the acoustic radiation force $\boldsymbol{F}_{\mathrm{ac}}$ is given by Eq. (3.12), and we note that the unmodified Stokes drag force is used for the drag force. Moreover, we neglected the fact that polystyrene particles is not neutrally buoyant in water $\rho_{\mathrm{p}} > \rho$. With a mass density difference of 5% (see table A.1), the gravitational forces on the particles will be minute compared to the other forces involved.

At the typical particle values: $2a = 10\,\mu$m and $u_{\mathrm{p}} = 1$ mm/s, the movement of the particle is happening at low Reynolds number, $Re = \rho a u_{\mathrm{p}}/\eta \approx 10^{-9} \ll 1$. This implies that viscous forces are highly dominant for the micro particle dynamics. In this case we find the characteristic

[1] This follows from knowing the Q factor to be 200-500 [37], meaning that after 200-500 oscillation cycles at MHz frequency, the steady state resonance mode is reached.

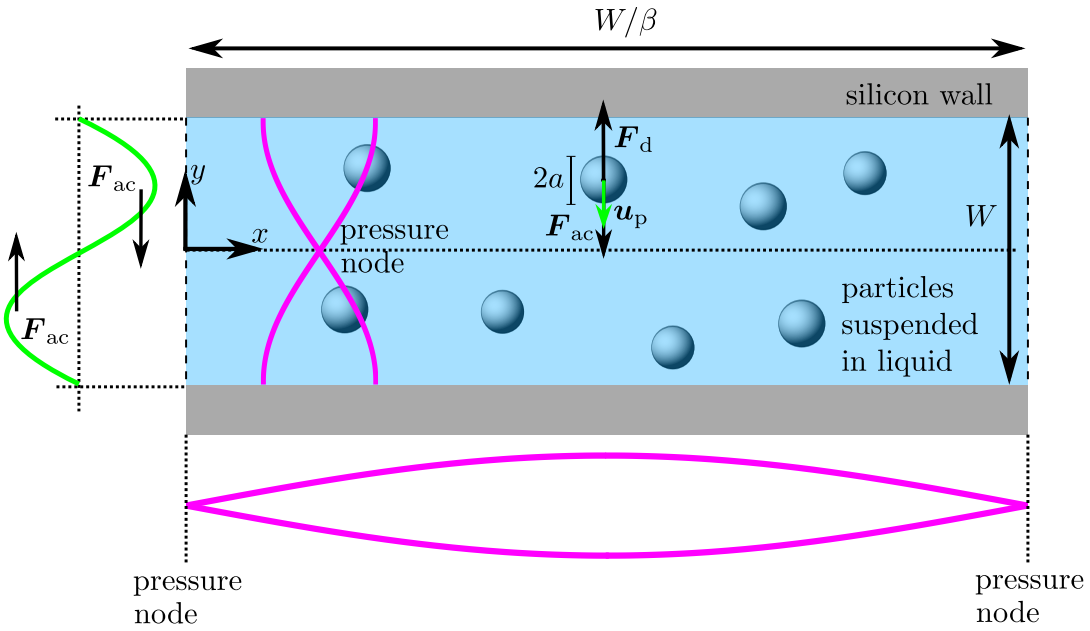

Figure 3.4: Sketch of the acoustofluidic channel in the xy plane, with vertical symmetry lines, denoted by dashed lines. The liquid-suspended particles, of diameter $2a$ are pushed toward the pressure nodes by the acoustic radiation force $\boldsymbol{F}_{\mathrm{ac}}$, denoted by the green curve to the left. The liquid acts on the particles with an equivalent and opposing drag force $\boldsymbol{F}_{\mathrm{d}}$ which rapidly results in a steady particle speed $\boldsymbol{u}_{\mathrm{p}}$ (green arrow). Lateral pressure nodes are had $x = \{0, W/\beta\}$, and a transverse pressure node is had $y = 0$ both denoted by dotted lines. The dashed lines denote the periodic boundaries.

acceleration time by solving Eq. (3.16) in one dimension with a constant external force. This yields an exponential decay time τ_{acc} before the velocity $\boldsymbol{u}_{\mathrm{p}}$ reaches terminal speed. This time [38] is of the order $\tau_{\mathrm{acc}} = \frac{2}{9}\rho_{\mathrm{p}} a^2/\eta \sim 10\,\mu\mathrm{s}$. Because this timescale is very short, we will often neglect effects of particle inertia and disregarding the acceleration term in Eq. (3.16).

3.4.1 Transverse particle movement

To make theoretical progress, we note from Eq. (3.12) that the acoustic radiation force $\boldsymbol{F}_{\mathrm{ac}}$, is weaker by a factor $\beta = 1/3$ in the lateral direction. We will therefore, as a first approximation, disregard the forces in the x-direction.

Barnkob *et al.* [39] calculated the dynamics of a single particle suspended in a quiescent fluid, in the case of no forces in the x-direction $F_{\mathrm{ac},x} = 0$. From Fig. 3.3(b) we see that at $x = \frac{1}{2}W/\beta$ this is fulfilled. By assuming that the fluid is undisturbed and neglecting the inertial term on the left hand side of Eq. (2.1), Barnkob *et al.* [39] finds for the particle

$$x(t) = \frac{W}{2\beta}\,, \quad y(t) = \frac{W}{\pi}\arctan\left[\tan\left(k_y(y_0 + W/2)\right)\exp\left(\frac{t}{t^*}\right)\right]\,, \tag{3.17}$$

where

$$\boxed{t^* = \frac{3\eta}{4\Phi_{2\mathrm{D}} k_y^2 a^2 E_{\mathrm{ac}}}\,.} \tag{3.18}$$

For typical values, the characteristic time scale t^* varies between 0.1-10 s. In this context, t^* should be seen as the characteristic migration time for a particle, in a undisturbed flow. Thus, t^*

will be our fundamental timescale for the movement of particles not interacting in any way with each other, and will be widely used for comparison when including particle-particle interaction.

3.4.2 Critical particle size $2a_{\mathrm{str}}$

Here it is important to note that the derivation of Barnkob *et al.* [39], is for a particle where acoustic streaming effects are negligible, see Section 2.2.2. As the acoustic streaming gives rise to a drag force on the particles $\boldsymbol{F}_{\mathrm{d}}$, it must scale with the radius a. The acoustic radiation force $\boldsymbol{F}_{\mathrm{ac}}$, scales with volume $V_{\mathrm{p}} \propto a^3$. Therefore, there will exist a turnover particle size $2a$, above which, the radiation force $\boldsymbol{F}_{\mathrm{ac}}$ dominates over streaming. Muller *et al.* [24], finds the critical particle size, by balancing streaming drag forces and acoustic radiation force

$$2a_{\mathrm{str}} = \sqrt{\frac{12}{\Phi}\frac{v_{\mathrm{s}}\, v_{\mathrm{str}}}{v_1^2}}\delta \approx 2\,\mu\mathrm{m} \qquad \text{(polystyrene in water)}\,, \tag{3.19}$$

where we recall that v_{s} is the isentropic speed of sound, v_1 is the amplitude of the first-order acoustic velocity field, v_{str} is the characteristic streaming velocity (Eq. (2.17)) and δ is the viscous boundary layer thickness (Eq. (2.16)). A typical streaming velocity, for the system described here, is $v_{\mathrm{str}} \approx 6\,\mu\mathrm{m/s}$ [24].

As we in this thesis, will make no attempts to incorporate streaming effects, all derivations of particle dynamics will be valid only for particle sizes well above $2a_{\mathrm{str}}$.

3.5 Non-interacting many particle dynamics

Having outlined the description for a single particle, we now model the full ensemble of particles in the micro-channel. To do this, one should ideally account for all N particles and the liquid simultaneously. As this is highly infeasible, we abandon the idea of the discrete nature of each particle, and see them as one scalar concentration field.

3.5.1 Continuous particle distribution

Consider some volume of fluid V containing a number of particles N. The average number per volume is simply $c_0 = N/V$. If we let N and V tend to zero then we can approximate the distribution of particles with a continuous concentration field, the so-called *number concentration*

$$c(\boldsymbol{r}, t) = \frac{\mathrm{d}N(\boldsymbol{r}, t)}{\mathrm{d}V} \qquad \text{(point particles)}\,. \tag{3.20}$$

This means that for a given small volume of liquid $\mathrm{d}V$, we have exactly $\mathrm{d}N(\boldsymbol{r}, t) = c(\boldsymbol{r}, t)\mathrm{d}V$ particles inside $\mathrm{d}V$. As the particle volumes V_{p} are non-zero, fluctuations in particle number will be present, when looking at small enough liquid volumes. It is therefore important to clarify that the concentration field approximation in Eq. (3.20), can only give us information on the average values over a large ensemble of experiments, and not the statistical concentration fluctuations that will be present in the experiment.

However, this approximation allows us to describe inhomogeneous particle distributions, changing in both time and space, with just one scalar field $c(\boldsymbol{r}, t)$, and it therefore serves as a very useful approach in our calculations.

3.5.2 The particle volume concentration ϕ

In working with the density of particles, the natural field to use is the "number per volume", or simply "number concentration" $c(\boldsymbol{r}, t)$ introduced in Eq. (3.20). However, as we in this thesis work with particle-particle interactions, it turns out that the another useful way to describe the local concentration of particles is by the *particle volume concentration* ϕ, or simply *volume concentration*. This concept was used already in section 2.3, but here, we will formally introduce the concept.

The volume concentration is defined as 'the total fractional volume of particles to total channel volume'. Using the assumption of a average starting concentration of $c_0 = N/V$, so must the particle have an initial average volume concentration

$$\phi_0 = \frac{N\, V_\mathrm{p}}{V} = V_\mathrm{p}\, c_0\,. \tag{3.21}$$

The particle volume concentration must likewise take on local values, following that of

$$\boxed{\phi(\boldsymbol{r}, t) = V_\mathrm{p}\, c(\boldsymbol{r}, t)\,.} \tag{3.22}$$

It is important to clarify that we will use number concentration c in derivations and volume concentration ϕ when presenting results, seeing as the latter is easier to physically visualise.

Closest particle packing

In the optimal case of closest particle packing the particles arrange in the hexagonal close packed structure, giving the maximum allowed volume concentration anywhere

$$\phi_\mathrm{max} = \frac{\pi}{3\sqrt{2}} \approx 0.74\,. \tag{3.23}$$

The average particle-particle distance $d_\mathrm{p-p}$

Another instructive calculation is to calculate the average particle-particle distance, from surface to surface, given some volume concentration ϕ. We denote this distance $d_\mathrm{p-p}$.

We assume the particles are homogeneously distributed, and described by a hexagonal close packed structure. We reason that for point particles, the total volume taken up per particle must scale inversely with the number concentration $1/c$, and cubed with particle-particle distance $d_\mathrm{p-p}^3 \propto 1/c$. But seeing as the particles are finite in extent, the particle-particle distance must be corrected with the particle diameter

$$d_\mathrm{p-p} = \alpha c_0^{-1/3} - 2a\,, \tag{3.24}$$

where is α is an unknown proportionality constant. From Eq. (3.22) we know the relation between c and ϕ, and the particle volume is $V_\mathrm{p} = \frac{4}{3}\pi a^3$. We exploit that when the particle are optimally packed ϕ_max, the particle-particle distance $d_\mathrm{p-p}$ is zero

$$0 = \alpha \left(\frac{\phi_\mathrm{max}}{V_\mathrm{p}}\right)^{-1/3} - 2a\,, \tag{3.25}$$

which simply implies for $\alpha = 2a\,(\phi_\mathrm{max}/V_\mathrm{p})^{1/3}$. The particle-particle distance becomes

$$\frac{d_\mathrm{p-p}}{2a} = \left(\frac{\pi}{3\sqrt{2}}\right)^{1/3} \phi^{-1/3} - 1 \approx 0.90\phi^{-1/3} - 1\,. \tag{3.26}$$

Eq. (3.26) is plotted in a LogLog plot in Fig. 3.5

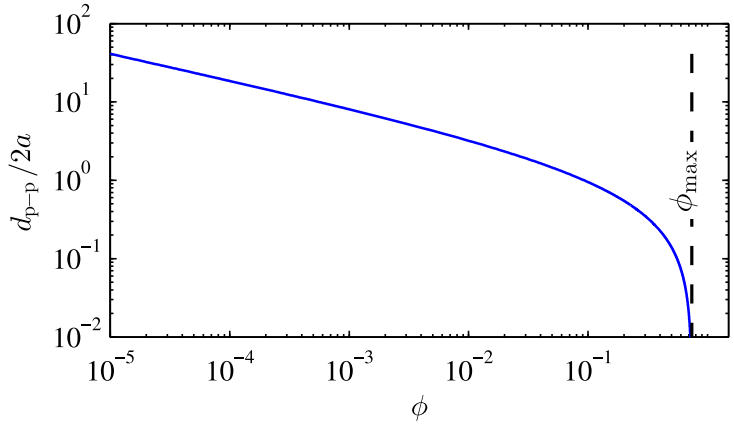

Figure 3.5: LogLog plot of the particle-particle distance $d_{\mathrm{p-p}}$ in terms of particle diameters $2a$, here as function of volume concentration ϕ.

3.5.3 Resulting governing equations

To derive the dynamics of the particles in terms of the concentration field $c(\boldsymbol{r}, t)$, we use the particle continuity equation defined in Eq. (2.2). Because we are describing single particle behaviour, but for the full ensemble of N particles, we include only effects of the acoustic radiation force $\boldsymbol{F}_{\mathrm{ac}}$ and diffusion

$$\partial_t c = -\boldsymbol{\nabla} \cdot [\boldsymbol{J}_{\mathrm{diff}} + \boldsymbol{J}_{\mathrm{ac}}] \,. \tag{3.27}$$

The diffusion current is given by Ficks law [5] $\boldsymbol{J}_{\mathrm{diff}} = -D\boldsymbol{\nabla} c$. Here, D is the diffusion constant, which we approximate by the Einstein expression [38] $D = k_{\mathrm{B}}T/(6\pi\eta a)$. At ambient temperature, the thermal energy $k_{\mathrm{B}}T = 4.1 \times 10^{-21}\,\mathrm{J}$, which gives diffusion constant of the order $D = 2.8 \times 10^{-21}\,\mathrm{m}^2/\mathrm{s}$ for $2a = 5\,\mu\mathrm{m}$.

To derive the particle current density from the acoustic radiation force $\boldsymbol{J}_{\mathrm{ac}}$, we use the general relation $\boldsymbol{J}_{\mathrm{p}} = c\boldsymbol{u}_{\mathrm{p}}$. To find the contribution from acoustic forces alone, we use the velocity caused only by the radiation force $\boldsymbol{J}_{\mathrm{ac}} = c\boldsymbol{u}_{\mathrm{ac}}$. Assuming constant force equilibrium on the particle, we get from Eq. (3.16)

$$\boldsymbol{u}_{\mathrm{ac}} = \frac{\boldsymbol{F}_{\mathrm{ac}}}{6\pi\eta a} \,. \tag{3.28}$$

In this description no account has been taken for the disturbance of the liquid by the particles. I.e we assume the liquid to remain at rest $\boldsymbol{v} = \boldsymbol{0}$, even though particles are continuously dragged through it. At sufficiently high particles concentrations, this will of course no longer be true, and we will account for this effect in the next section.

Inserting the particle currents from diffusion $\boldsymbol{J}_{\mathrm{diff}}$ and the acoustic radiation force $\boldsymbol{J}_{\mathrm{ac}}$ in Eq. (3.27), we find

$$\partial_t c = -\boldsymbol{\nabla} \cdot \left[-D\boldsymbol{\nabla} c + \frac{1}{6\pi\eta a} \boldsymbol{F}_{\mathrm{ac}}\, c \right] \,, \tag{3.29}$$

where we note that the unmodified Stokes drag force is used as no interactions are included. We will solve the particle dynamics in the present form, expressed in c, but all the results will be stated in the particle volume concentration ϕ, by simply using Eq. (3.22).

Influence of diffusion

To estimate the expected influence of the diffusion term $\boldsymbol{J}_{\mathrm{diff}}$, we make a simple scaling argument. For the diffusion term $\boldsymbol{J}_{\mathrm{diff}} = -D\boldsymbol{\nabla} c$, we again use the Einstein relation for the diffusion

constant $D = k_\mathrm{B}T/(6\pi\eta a)$ and assume a steep concentration gradient $\boldsymbol{\nabla} \sim \frac{20}{W}$. For the acoustic drift term $\boldsymbol{J}_\mathrm{ac} = \boldsymbol{F}_\mathrm{ac}\, c/(6\pi\eta a)$, we see from Eq. (3.13) that the term must scale with $J_\mathrm{ac} \approx 3cV_\mathrm{p}E_\mathrm{ac}k_y\Phi_\mathrm{2D}/(6\pi\eta a)$. Comparing the two terms at ambient temperature and assume a rather low energy density $E_\mathrm{ac} = 10\ \mathrm{J/m^3}$ and a small particle $2a = 1\,\mu\mathrm{m}$ we find

$$\frac{J_\mathrm{ac}}{J_\mathrm{diff}} \approx \frac{\pi^2 a^3 \Phi_\mathrm{2D} E_\mathrm{ac}}{5k_\mathrm{B}T} \approx 10^2\,. \tag{3.30}$$

From this it is clear that even for small particle sizes and low acoustic energy density, diffusion effects are expected to be very small.

Resulting Boundary conditions

The boundary conditions for the particle dynamics are stated in Eqs. (3.1) and (3.2). Both at the periodic boundaries and at the hard walls, see Fig. 3.2, no-flux conditions must be met $\boldsymbol{J}_\mathrm{p} \cdot \boldsymbol{n} = 0$. We note from Eq. (3.12) that the normal components of the acoustic radiation force $\boldsymbol{n} \cdot \boldsymbol{F}_\mathrm{ac} = 0$ automatically goes to zero at the respective boundaries. This leaves the no-flux condition to be satisfied only the normal derivatives of concentration

$$\boldsymbol{n} \cdot \boldsymbol{\nabla} c = 0 \quad \text{for} \quad \boldsymbol{r} \in \partial\Omega\,. \tag{3.31}$$

3.6 Interacting many particle dynamics

Until now, we have assumed that no particle-particle interaction takes place. In this section we will include three particle-particle interaction effects.

3.6.1 Global interaction through the fluid velocity

As the particles move through the channel the liquid acts on the particles with the Stokes drag force, slowing them down. Due to Newtons third law, the particles must act with an equal and opposing force on the liquid. This transfer of momentum from the particles to the liquid have so far been neglected. In the limit of dilute particle suspensions, this momentum transfer is minute and was therefore disregarded in the non-interacting case. Going to the regime of concentrated particle suspensions, we reason that the momentum transfer must at some point become significant. The resulting fluid velocity $\boldsymbol{v}$, will globally change the drag forces $\boldsymbol{F}_\mathrm{d}$ on the particles, which in turn changes the particle dynamics. In this way, one of the interaction effects can be modelled as hydrodynamic particle-particle interactions, mediated by the liquid.

One way to think of this interaction, is by the following simple physical picture: As a particle is dragged through the liquid by the acoustic radiation force $\boldsymbol{F}_\mathrm{ac}$, small perturbations to the fluid is created in its wake. If the suspension is sufficiently dense, neighbouring particles will feel these perturbations, and they are slightly dragged along by the wake of the first particle.

To derive the force on the fluid, we consider a small volume of fluid $\mathrm{d}V$. In this volume, we have $\mathrm{d}N(\boldsymbol{r},t) = c(\boldsymbol{r},t)\,\mathrm{d}V$ particles. The liquid exerts the drag force $\boldsymbol{F}_\mathrm{d}$ on each particle. Therefore, the particles must each exert the force $-\boldsymbol{F}_\mathrm{d}$ on the fluid. Because each particle is considered to be in a force equilibrium between the drag force and the acoustic radiation force $\boldsymbol{0} = \boldsymbol{F}_\mathrm{d} + \boldsymbol{F}_\mathrm{ac}$, the force on the fluid by each particle is $\boldsymbol{F}_\mathrm{ac}$. Having $\mathrm{d}N(\boldsymbol{r},t)$ particles in the fluid volume $\mathrm{d}V$, the total force on $\mathrm{d}V$ is $\mathrm{d}N(\boldsymbol{r},t)\,\boldsymbol{F}_\mathrm{ac}$. In hydrodynamics, we work with force per volume. The external force density on the fluid exerted by the particles simply becomes

$$\boldsymbol{f}_\mathrm{ext} = \frac{\mathrm{d}N(\boldsymbol{r},t)\,\boldsymbol{F}_\mathrm{ac}}{\mathrm{d}V} = c(\boldsymbol{r},t)\,\boldsymbol{F}_\mathrm{ac}\,. \tag{3.32}$$

This inserted in the Navier-Stokes Eq. (2.3a), which then gives rise to non-zero fluid velocities $\boldsymbol{v}$. This changes the drag force $\boldsymbol{F}_\mathrm{d}$, as it is given by the movement of the particle *relative* to the surrounding fluid

$$\boldsymbol{F}_\mathrm{d} = -6\pi\eta a(\boldsymbol{u}_\mathrm{p} - \boldsymbol{v})\,. \tag{3.33}$$

The model of letting the particles act on the liquid with a bulk force density is adopted from Mikkelsen and Bruus [38].

3.6.2 Local particle-particle interactions through viscosity

In section 2.3, we discussed two effects on viscosity changes when making concentrated particle suspensions. Effectively, this can be seen as particle-particle interactions, as properties of the governing equations change with the number concentration ϕ.

Interactions through effective viscosity

Seeing the particles and the fluid as one effective medium, one could view the effect of the particles as increasing the effective medium viscosity η_eff. In section 2.3.3, we used an approximative model by Happel and Brenner [18], and found the effective viscosity as function of particle volume concentration $\eta_\mathrm{eff}(\phi)$, see Eq. (2.39). Because this effective viscosity governs the total effective medium of both particles and liquid, η_eff must enter only in the Navier-Stokes Eq. (2.3a).

Interaction through effective particle mobility

When a particle is subjected to an external force $\boldsymbol{F}$, the usual approach is to balance $\boldsymbol{F}$ by an opposing Stokes drag force $\boldsymbol{F}_\mathrm{d}$, resulting in the velocity $\boldsymbol{u}_\mathrm{p}$, as we did in Eq. (3.33). In a concentrated suspension where the particles lie close together, we imagine exerting the same force $\boldsymbol{F}$ on a particle. Because the no-slip condition on the surface of all particles must satisfied at all times, additional viscous stresses build up in the liquid between the particles. Thus, resulting in a lower response $\boldsymbol{u}_\mathrm{p}$ of the particle. In section 2.3.2, we reviewed a model also by Happel and Brenner [18], for this decrease in *effective particle mobility*, due to hydrodynamic particle-particle interactions. The result is a modified drag force, now a function of the volume concentration

$$\boldsymbol{F}_\mathrm{d}(\phi) = -\frac{6\pi\eta a}{\chi(\phi)}(\boldsymbol{u}_\mathrm{p} - \boldsymbol{v})\,, \tag{3.34}$$

where $\chi(\phi)$ is the dimensionless function found in Eq. (2.31). The change in particle mobility can then by inserted in the particle continuity Eq. (2.2)

3.6.3 Resulting governing equations

In analogy with section 3.5.3, we find the contributions to the particle current density $\boldsymbol{J}_\mathrm{p}$. The diffusion is again given by Ficks law [5] $\boldsymbol{J}_\mathrm{diff} = -D\boldsymbol{\nabla}c$, and the particle current from the acoustic radiation force is again found by considering the general relation $\boldsymbol{J}_\mathrm{p} = c\boldsymbol{u}_\mathrm{p}$. The particle velocity $\boldsymbol{u}_\mathrm{p}$ associated with acoustic radiation force and fluid convection is found from Eq. (3.34) which yields two contributions to $\boldsymbol{J}_\mathrm{p}$

$$\boldsymbol{J}_\mathrm{conv} + \boldsymbol{J}_\mathrm{ac} = \boldsymbol{v}\,c + \frac{\chi(\phi)}{6\pi\eta a}\boldsymbol{F}_\mathrm{ac}\,c\,. \tag{3.35}$$

The resulting particle continuity equation becomes

$$\begin{aligned}\partial_t c &= -\boldsymbol{\nabla}\cdot[\boldsymbol{J}_{\text{diff}} \quad + \boldsymbol{J}_{\text{conv}} \quad + \boldsymbol{J}_{\text{ac}}] \\ &= -\boldsymbol{\nabla}\cdot\left[-D\boldsymbol{\nabla}c \quad + \boldsymbol{v}\,c \quad + \frac{\chi(\phi)}{6\pi\eta a}\boldsymbol{F}_{\text{ac}}\,c\right] \qquad (3.36a)\\ &= -\boldsymbol{\nabla}\cdot[-D\boldsymbol{\nabla}c \quad + \boldsymbol{v}\,c \quad + \chi(\phi)\boldsymbol{u}_{\text{ac}}\,c] \qquad (3.36b)\end{aligned}$$

In the entries for volume concentration we use the relation $\phi = V_{\text{p}}\,c$, for converting to number concentration c, and doing this we note that Eq. (3.36) is non-linear. In Eq. (3.36b) we have introduced the particle velocity due to acoustic drift alone in the dilute limit $\boldsymbol{u}_{\text{ac}}$. Since both terms scale with c, we can physically think of the convective term $\boldsymbol{J}_{\text{conv}}$ and the acoustic drift term $\boldsymbol{J}_{\text{ac}}$ as a matter of comparing the two velocities: $\boldsymbol{v}$ and $\chi(\phi)\boldsymbol{u}_{\text{ac}}$. From Section 2.3.2, we recall that the relative particle mobility decreases rapidly with high concentration $\chi \ll 1$. This implies that we expect the convective term $\boldsymbol{v}\,c$ to become increasingly important in the high concentration regime. The physical interpretation is that as the relative particle mobility goes down, it becomes increasingly difficult for the particles to move relative to the surrounding fluid. This makes the particles and the fluid follow each other increasingly, and harder to separate, as the concentration increases.

Governing the fluid dynamics

Since the fluid is no longer quiescent $\boldsymbol{v} \neq \boldsymbol{0}$, we have to involve the Navier-Stokes and mass continuity equations. Because the fluid velocity in this case is comparable to typical particle speeds $u_{\text{p}} \sim 1\,\text{mm/s}$, changing very slowly with time $\sim t^* \sim 1\,\text{s}$, compared to the oscillating ultrasound fields, we can assume the fluid to be incompressible. Furthermore, as mentioned in section 3.4, the Reynolds number is small $Re \approx W u_{\text{p}}\rho/\eta \lesssim 10^{-1} \ll 1$ which allows us to cancel the non-linear term in the Navier-Stokes equation. The Navier-Stokes and mass continuity Eqs. (2.3a) and (2.3b) become

$$\rho\partial_t\boldsymbol{v} = -\boldsymbol{\nabla}p + \underbrace{\eta\,\psi(\phi)}_{\eta_{\text{eff}(\phi)}}\nabla^2\boldsymbol{v} + c\,\boldsymbol{F}_{\text{ac}}\,, \qquad (3.37)$$

$$\boldsymbol{\nabla}\cdot\boldsymbol{v} = 0\,. \qquad (3.38)$$

In this approach to find the fluid velocity $\boldsymbol{v}$ and pressure p, no account has been taken for effects of acoustic streaming, discussed in section 2.2.2. Thus, any influence of the streaming on the particle dynamics, are by default not included in this treatment. For the analysis of the particle dynamics to be valid, particle sizes must therefore be above the critical particle size $2a > 2a_{\text{str}} \approx 2\,\mu\text{m}$, described in section 3.4.2.

Characteristic values

To find the characteristic values of the fluid velocity v^* and pressure p^*, we consider the resulting Navier-Stokes Eq. (3.37), and the external forces on the liquid $c\,\boldsymbol{F}_{\text{ac}}$. From the vector plot of the acoustic radiation force $\boldsymbol{F}_{\text{ac}}$ in figure 3.3, we see that significant forces will be on the liquid in the y-direction, from each side of the channel sidewalls and towards $y = 0$. This could imply that large hydrostatic pressures will build up, relieving much of the external forces $c\boldsymbol{F}_{\text{ac}}$. Assuming for the gradient of the pressure $\boldsymbol{\nabla} \sim 2/W$, we choose the characteristic pressure as $p^* = \frac{1}{2}W\,c_0\,F_{\text{ac}}$. For the fluid velocity, we reason that, since it is the particles that is essentially driving the fluid, we assume the fluid and particle velocities to be comparable. We therefore

choose the characteristic fluid velocity to be equal to the single particle acoustic drift velocity $\boldsymbol{u}_{\mathrm{ac}}$ in the dilute regime $v^* = u_{\mathrm{ac}} = F_{\mathrm{ac}}/(6\pi\eta a)$ see Eq. (3.28). This will be valid in the regime where the momentum transfer from the particles to the fluid is significant, i.e. at high volume concentration ϕ_0.

Boundary conditions

For the fluid velocity and pressure, we get the resulting boundary equations from Eqs. (3.1) and (3.2)

$$\text{hard wall:}\quad \boldsymbol{v} = \boldsymbol{0}\quad \text{(no-slip)}\quad \text{for}\quad \boldsymbol{r} \in \partial\Omega_{\mathrm{wall}} \tag{3.39}$$

$$\text{periodic BC:}\qquad \left.\begin{array}{rl} v_x = 0 & \text{(no in/out-flow of fluid)} \\ \partial_x v_y = 0 & \text{(no tangential stress)} \end{array}\right\} \quad \text{for}\quad \boldsymbol{r} \in \partial\Omega_{\mathrm{sym-bdy}}\,. \tag{3.40}$$

We note that the boundary condition for the pressure p is no longer there. The pressure can in a sense adjust freely, balancing the forces in the Navier-Stokes Eq. (3.37). We only demand the level of the pressure remains fixed in the center of the domain Ω

$$\text{level set:}\quad p = 0 \quad \text{for}\quad (x,y) = \left(\frac{1}{2}W/\beta, 0\right)\,. \tag{3.41}$$

In analogy with the arguments in Section 3.5.3, we note from the resulting governing equations (3.36a), (3.37) and (3.38) that only the diffusion particle current $\boldsymbol{J}_{\mathrm{diff}}$, does not in itself satisfy the boundary conditions for the particle current density $\boldsymbol{J}_{\mathrm{p}}$, see Eqs. (3.1) and (3.2). Both the convective term $\boldsymbol{J}_{\mathrm{conv}}$ and the acoustic term $\boldsymbol{J}_{\mathrm{ac}}$, have normal components that by virtue of the acoustic radiation force $\boldsymbol{F}_{\mathrm{ac}}$ and the fluid velocity $\boldsymbol{v}$ go to zero at the boundary, i.e. $\boldsymbol{F}_{\mathrm{ac}} \cdot \boldsymbol{n} = \boldsymbol{v} \cdot \boldsymbol{n} = 0$ is automatically satisfied at all part of the boundary, thus satisfying the no-flux condition of the terms $\boldsymbol{J}_{\mathrm{conv}}$ and $\boldsymbol{J}_{\mathrm{ac}}$. Therefore, the boundary equation for the concentration field, becomes once more

$$\boldsymbol{n} \cdot \boldsymbol{\nabla} c = 0 \quad \text{for}\quad \boldsymbol{r} \in \partial\Omega\,. \tag{3.42}$$

Scaling argument

In order to understand what parameters that later will turn out to be important, for the scaling of hydrodynamic interaction effects, we consider the particle continuity Eq. (3.36a) and Navier-Stokes Eq. (3.37).

We note that the 'driving' terms $\boldsymbol{J}_{\mathrm{ac}}$ and $c\boldsymbol{F}_{\mathrm{ac}}$ in Eqs. (3.36a) and (3.37) both contain the factor $k_y E_{\mathrm{ac}} \Phi_{\mathrm{2D}}$, stemming from force amplitude F_{ac} (Eq. (3.13)). We can therefore factor out these quantities. The same goes for the fluid viscosity η that enters directly in $\boldsymbol{J}_{\mathrm{ac}}$, and in the Laplace term in the Navier-Stokes Eq. (3.37).

This leaves us to conclude that the two scaling parameters of interest are the initial volume concentration ϕ_0 and the size of the particle which we choose as the diameter $2a$.

3.7 Lists of assumptions and characteristic quantities

To use as a reference tool, we have in Tables 3.1 and 3.2, summarised all the assumptions and characteristic values of relevance used throughout the thesis.

Table 3.1: Full list of assumptions used throughout the thesis

Assumption for	**Ref.**	**Assumption**
Acoustic fields	Eq. (2.11)	We assume harmonic time dependence of first order velocity $\boldsymbol{v}_1$ and pressure p_1.
Acoustic fields	Eq. (3.1)	Assume hard walls to find p_1 in the Helmholtz eq.
Acoustic fields	Eqs. (2.13) and (2.14)	To find $\boldsymbol{v}_1$ and p_1 we neglect viscosity in bulk fluid, and disregard the viscous boundary layers
Acoustic fields	Section 3.4	We neglect the fact that the ultrasonic forces builds up over $\sim$100 ms, and approximate the acoustic fields to be established instantaneously.
Acoustic fields	Section 3.2	We neglect the irregular lateral changes along the length of the channel and assume $\lambda_x = 3\lambda_y$ ($\beta = \frac{1}{3}$)
Acoustic fields	Section 7.2	We disregard the fact that high particle concentrations might alter the effective sound-propagation properties of the medium, as the volume fraction of particles increases. This effect is discussed in Section 7.2
Radiation force	Section 3.3	Assume the Rayleigh limit $2a \ll \lambda = 2\pi/k$.
Radiation force	Section 2.2.1	We disregard any effects of thermal conductivity on the acoustic radiation force
Radiation force	Section 7.2	We neglect radiation forces from particle-particle wave scattering, called Bjerknes forces. Discussed in Section 7.2
Particle dynamics	Eq. (3.20)	We assume that the particles can be described by a continuous field c, disregarding their spatial size.
Particle dynamics	Section 3.1.1	We disregard any variations in the z-direction
Particle dynamics	Section 3.4.2	Disregard effects of acoustic streaming effects, implying that our consideration are valid for particles sizes $> a_{\text{str}}$
Particle dynamics	Section 3.4	We neglect inertial effects of the particles.
Particle dynamics	Section 3.4	We neglect gravitational forces on both the particles and the liquid, because we know that polystyrene is almost neutrally buoyant. Mass density discrepancy of approximately 5% , see Table A.1.

Table 3.2: Overview over the characteristic quantities used in the thesis, listed with typical values.

Quantity	Characteristic value	Expression	Typical value
Particle conc.	Initial number concentration	$c^* = c_0$	1×10^{15}
	Initial volume concentration	$\phi^* = \phi_0 = V_\mathrm{p}\, c_0$	0.1
Length	Half channel width	$L^* = W/2$	200 µm
Force on particles	Acoustic rad. force	$F^* = F_\mathrm{ac} = 3V_\mathrm{p} E_\mathrm{ac} k_y \Phi_\mathrm{2D}$	2 pN
Time	Particle Convection time	$t^* = \dfrac{3\eta}{4\Phi_\mathrm{2D} k_y^2 a^2 E_\mathrm{ac}}$	1 s
Particle velocity	Maximum particle velocity	$u_\mathrm{p}^* = u_\mathrm{ac} = \frac{F_\mathrm{ac}}{6\pi\eta a}$	1 mm/s
Fluid velocity	Maximum particle velocity	$v^* = u_\mathrm{ac} = \frac{F_\mathrm{ac}}{6\pi\eta a}$	1 mm/s
Pressure	Force Balance in NS Eq. (3.37)	$p^* = \frac{W}{2} c_0\, F_\mathrm{ac}$	0.1 Pa

3.8 Concluding remarks

We have now proposed physical models, both for non-interacting case, as well as the interacting case. These two models can now be compared to investigate the effects of particle-particle interactions, under the assumptions taken. Since the governing equations are inhomogeneous non-linear coupled differential equations, we perform a a numerical implementation in the next section, in order to solve the set of equations.

Chapter 4

Numerical implementation in COMSOL

In this chapter we introduce a numerical method called the *finite element method* (FEM). This method is used for solving partial differential equations in many branches of engineering and science. The strength of FEM is the ability to provide approximate solutions to complex differential equations that are otherwise hard to solve. These solutions are called *weak solutions*. Our model is implemented in the FEM framework using COMSOL MULTIPHYSICS, which is a piece of commercially available software [40]. The specific COMSOL model will be described, and mesh convergence analysis will be performed to justify the reliability of the numerical results. Lastly we briefly discuss the numerical stability of the model.

4.1 The finite element method

The basic idea in the *finite element method*, is to discretize the problem in a finite set of localized basis functions. The principle of using basis functions to span a solution, is well known from e.g. Fourier analysis and spherical harmonic functions. In FEM, the computation domain is not restricted to highly symmetrical geometries, as compared to other methods. But instead, allows for solving equations with several inter-dependent variables in complex geometries. The theory in this section is based on [41, 42].

As a starting point we consider the case of a general differential equation problem for the function $g(\boldsymbol{r})$

$$\mathcal{L}\left\{g(\boldsymbol{r})\right\} = F(\boldsymbol{r})\,, \tag{4.1}$$

where $\mathcal{L}$ is a linear differential operator and $f(\boldsymbol{r})$ is some source term. Next, we define the defect

$$d(\boldsymbol{r}) \equiv \mathcal{L}\left\{g(\boldsymbol{r})\right\} - F(\boldsymbol{r})\,. \tag{4.2}$$

By definition, the defect is zero for an exact solution of Eq. (4.1). This type of solution is called a *strong solution*. Next, the computation domain Ω is discretized in a finite number of grid points, see Fig. 4.1, and a basis function function is defined for each node in the grid. This is illustrated in figure 4.1 where we see a linear basis function for the nth node $\hat{g}_n$. The basis functions fulfil the criteria of being 1 at their own node, and 0 everywhere else, and the sum of basis functions must be continuous and piecewise differentiable. In Fig. 4.1 the basis function $\hat{g}_n$ is chosen to be linear. However, basis functions of higher order polynomials can also be used. The order depends partly on the wanted precision between grid points, but is primarily

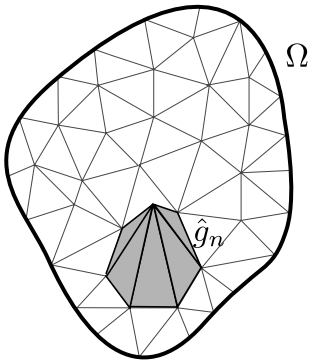

Figure 4.1: Discretezation of the computation Ω in triangular elements. The nth basis function $\hat{g}_n$ is 1 at the nth node, and 0 everywhere else. The figure is adapted from [41]

determined by the order of derivatives involved in the problem. It is assumed that $g(\boldsymbol{r})$ can be approximately expanded in terms of the spatially discretized basis functions

$$g(\boldsymbol{r}) = \sum_n a_n \, \hat{g}_n \,, \tag{4.3}$$

where a_n is the expansion coefficients for $g(\boldsymbol{r})$. Mathematically, a_n is nothing but the value of $g(\boldsymbol{r})$ at the nth grid node. To find a solution for $g(\boldsymbol{r})$, we demand that the projection of all basis functions onto the defect is zero

$$\langle \hat{g}_m, d(\boldsymbol{r}) \rangle = 0 \quad \text{for all } m \,. \tag{4.4}$$

Here we have defined the inner product between two real functions as $\langle X(\boldsymbol{r}), Y(\boldsymbol{r}) \rangle \equiv \int_\Omega \mathrm{d}V \, X(\boldsymbol{r}) Y(\boldsymbol{r})$. By inserting the definition of the defect $d(\boldsymbol{r})$ in Eq. (4.4), we get

$$\sum_n a_n \, \langle \hat{g}_m, \mathcal{L} \hat{g}_n \rangle = \langle \hat{g}_m, F \rangle \quad \text{for all } m \,. \tag{4.5}$$

Noting that we have two summation indices (n, m) in Eq. (4.5), and because the inner product is linear, we can formulate the problem as a matrix equation

$$\boldsymbol{K} \, \boldsymbol{a} = \boldsymbol{f} \,, \tag{4.6}$$

where $\boldsymbol{K} = \{K_{mn}\}$ is called the stiffness matrix [41], and $\boldsymbol{a} = \{a_n\}$ contains the coefficients that are varied to satisfy the above equations. Solving this matrix equation, is called finding a *weak solution* to Eq. (4.1), and is exactly what COMSOL does. The discrepancy between *weak* and *strong* solutions lies in the fact that we only use a finite set of basis functions. As the set is finite, the function space of the differential equation (4.1), is only approximately spanned. This means that the demand of the defect being orthogonal to all the basis functions $\hat{g}_m$, implies that it is only approximately zero $d(\boldsymbol{r}) \approx 0$. This stands in contrast to strong solutions, where the defect is exactly zero $d(\boldsymbol{r}) = 0$.

4.1.1 Boundary conditions in the weak formulation

To implement boundary conditions in the weak formulation, we recall that all three main governing equations are in essence continuity equations: Navier-Stokes Eq. (momentum), mass continuity Eq. (fluid) and particle continuity Eq. (particles). We therefore assume the form of a continuity equation

$$\boldsymbol{\nabla} \cdot \boldsymbol{\Gamma} = F \,. \tag{4.7}$$

Again, we take the inner product between Eq. (4.7) and the basis function $\hat{g}_m$

$$\langle \hat{g}_m, \boldsymbol{\nabla} \cdot \boldsymbol{\Gamma} - F \rangle = \int_\Omega \mathrm{d}V \, (\hat{g}_m \, \boldsymbol{\nabla} \cdot \boldsymbol{\Gamma} - \hat{g}_m \, F) = 0 \quad \text{for all } m \,. \tag{4.8}$$

Integrating the divergence term in Eq. (4.8) by parts, and using the Gauss theorem for integrals, we convert some of the integral to an integral over the boundary

$$\oint_{\partial\Omega} \mathrm{d}A \, \boldsymbol{n} \cdot \boldsymbol{\Gamma} + \int_\Omega \mathrm{d}V \, (- [\boldsymbol{\nabla} \hat{g}_m] \cdot \boldsymbol{\Gamma} - \hat{g}_m F) = 0 \quad \text{for all } m \,. \tag{4.9}$$

Neumann boundary conditions

In the case of Neumann boundary conditions where the flux of $\boldsymbol{\Gamma}$ is a known function $h(\boldsymbol{r})$ on the domain boundary

$$h(\boldsymbol{r}) = \boldsymbol{n} \cdot \boldsymbol{\Gamma} \quad \text{for } \boldsymbol{r} \in \partial\Omega \qquad \text{(Neumann)} \,, \tag{4.10}$$

$h(\boldsymbol{r})$ can be inserted directly in Eq. (4.9).

Dirichlet boundary conditions

In the case of Dirichlet boundary condition, it is instead the value of $g(\boldsymbol{r})$ that is a known function $j(\boldsymbol{r})$ on the boundary

$$j(\boldsymbol{r}) = g(\boldsymbol{r}) \quad \text{for } \boldsymbol{r} \in \partial\Omega \qquad \text{(Dirichlet)} \,. \tag{4.11}$$

The Dirichlet condition can be implemented in the weak formulation, by introducing a constraint to the problem $R(g(\boldsymbol{r})) = 0$. To implement the constraint we introduce a field $\lambda(\boldsymbol{r})$ that only exists on the domain boundary $\partial\Omega$. The so-called Lagrange multiplier. The Lagrange multiplier, is expanded in a new set of basis functions

$$\lambda(\boldsymbol{r}) = \sum_m b_n \, \hat{\lambda}_m(\boldsymbol{r}) \,. \tag{4.12}$$

We require all basis functions of the Lagrange multiplier to to be orthogonal to the constraint

$$\left\langle \hat{\lambda}_m, \, R \right\rangle = 0 \quad \text{for all } m \,. \tag{4.13}$$

Since the Lagrange multiplier $\lambda(\boldsymbol{r})$ only lives on the boundary, we can add the product of the constraint R and the Lagrange multiplier $\lambda(\boldsymbol{r})$, to Eq. (4.7)

$$\boldsymbol{\nabla} \cdot \boldsymbol{\Gamma} = F + \sum_n \lambda(\boldsymbol{r}) \hat{g}_n(\boldsymbol{r}). \tag{4.14}$$

Here R has taken the form of the original set of basis functions $\{\hat{g}_n\}$. The Dirichlet boundary condition of Eq. (4.14), is then satisfied by varying the b_n coefficients of the Lagrange multiplier.

4.2 Weak form model implementation

Before we rewrite the governing equations into weak form, we first introduce the logarithm of the concentration

$$s = \log\left(\frac{c}{c_0}\right) \,. \tag{4.15}$$

Because the particle number concentration c can assume very large numerical values, it is easier for COMSOL to numerically handle the logarithmic scaled concentration s. We will substitute s for c in the following.

4.2.1 Weak form for non-interacting many particle dynamics

To arrive at the weak form for the particle continuity equation in the non-interacting case, we rewrite Eq. (3.29) using the logarithm of the concentration $s = \log(c/c0)$. Inserting the definition for s in

$$\partial_t s = D\left(|\boldsymbol{\nabla} s|^2 + \nabla^2 s\right) - \frac{1}{6\pi\eta a}\left(\boldsymbol{\nabla}\cdot\boldsymbol{F}_{\mathrm{ac}} + \boldsymbol{F}_{\mathrm{ac}}\cdot\boldsymbol{\nabla} s\right), \tag{4.16}$$

Taking the inner product between the basis function $\hat{s}_n$ and the defect $d(s)$ of Eq. (3.29) we get the weak form governing equation for the non-interacting case

$$\begin{aligned} 0 = \langle \hat{s}_n, d(s)\rangle = &\oint_{\partial\Omega} \mathrm{d}\ell\, \boldsymbol{n}\cdot\left[\hat{s}_n\left(-D\boldsymbol{\nabla} s + \frac{1}{6\pi\eta a}\boldsymbol{F}_{\mathrm{ac}}\right)\right] \\ &+ \int_\Omega \mathrm{d}A\left[\hat{s}_n\left(\partial_t s - D\,|\boldsymbol{\nabla} s|^2 + \frac{1}{6\pi\eta a}\boldsymbol{F}_{\mathrm{ac}}\cdot\boldsymbol{\nabla} s\right) - \left(-D\boldsymbol{\nabla} + \frac{1}{6\pi\eta a}\boldsymbol{F}_{\mathrm{ac}}\right)\cdot\boldsymbol{\nabla}\hat{s}_n\right]. \end{aligned} \tag{4.17}$$

We note that, because the domain Ω is two-dimensional, the surface integral over $\partial\Omega$ is converted into a line integral, and the volume integral over Ω is converted into a surface integral.

4.2.2 Weak form for interacting many particle dynamics

Repeating the process, from the previous section, we insert the logarithm of the concentration s in the particle continuity equation, now only for the interacting case. From Eq. (3.36a), we find

$$\partial_t s = D\left(|\boldsymbol{\nabla} s|^2 + \nabla^2 s\right) - \left(\boldsymbol{\nabla}\cdot\boldsymbol{v} + \boldsymbol{v}\cdot\boldsymbol{\nabla} s\right) - \frac{1}{6\pi\eta a}\left(\boldsymbol{\nabla}\cdot\left[\frac{1}{\chi}\boldsymbol{F}_{\mathrm{ac}}\right] + \left[\frac{1}{\chi}\boldsymbol{F}_{\mathrm{ac}}\right]\cdot\boldsymbol{\nabla} s\right). \tag{4.18}$$

Again, we take the inner product between the basis function $\hat{s}_n$ and the defect $d(s)$ of Eq. (4.18), to find the weak form governing equation for the interacting case

$$\begin{aligned} 0 = \langle \hat{s}_n, d(s)\rangle = &\oint_{\partial\Omega} \mathrm{d}\ell\, \boldsymbol{n}\cdot\left[\hat{s}_n\left(-D\boldsymbol{\nabla} s + \boldsymbol{v} + \frac{1}{6\pi\eta a\chi}\boldsymbol{F}_{\mathrm{ac}}\right)\right] \\ + \int_\Omega \mathrm{d}A\Bigg[&\hat{s}_n\left(\partial_t s - D\,|\boldsymbol{\nabla} s|^2 + \boldsymbol{v}\cdot\boldsymbol{\nabla} s + \frac{1}{6\pi\eta a\chi}\boldsymbol{F}_{\mathrm{ac}}\cdot\boldsymbol{\nabla} s\right) - \left(-D\boldsymbol{\nabla} + \boldsymbol{v} + \frac{1}{6\pi\eta a\chi}\boldsymbol{F}_{\mathrm{ac}}\right)\cdot\boldsymbol{\nabla}\hat{s}_n\Bigg]. \end{aligned} \tag{4.19}$$

The mass continuity equation is not affected by the variable change from c to s, but the Navier Stokes equation is slightly modified. We get from Eq. (3.37)

$$\rho\partial_t\boldsymbol{v} = -\boldsymbol{\nabla} p + \eta\,\psi\nabla^2\boldsymbol{v} + c_0\,\mathrm{e}^s\,\boldsymbol{F}_{\mathrm{ac}} \tag{4.20}$$

For the weak form implementation of the Navier-Stokes equation Eq. (4.20) and the mass continuity Eq. (3.36a), we use the COMSOL *creeping flow* module that has these equations pre-programmed, along with a number of typical boundary conditions [40].

4.3 COMSOL model

The governing equations (4.17) and (4.19) are implemented as explained above in a two-dimensional rectangular domain Ω, of the type shown in figure 3.2. Symmetry of the problem suggests that one could simulate only a quarter of the rectangle. But due to particle accumulation in the channel center over time, it is more stable to simulate the full rectangular domain, ensuring no particle accumulation at the boundaries. The simulation domain used in COMSOL is shown in figure 4.2. The letters (a)-(g) denote the points, lines and areas where various properties and boundary conditions are imposed. The details are summarised in table 4.1.

Table 4.1: Overview of the imposed mesh sizes and boundary conditions in the computation domain Ω shown in figure 4.2. The mesh setting shown in this table, corresponds to the finest mesh ($k_{\text{mesh}} = 1$).

	Type	Mesh size	Growth rate	Imposed boundary condition
(a)	Bulk	d_{mesh}	1.1	$s = 1$, $\boldsymbol{v} = \mathbf{0}$, $p = 0$ for $t = 0$
(b)	Wall boundary	$d_{\text{mesh}}/1.66$	1.1	$\partial_y s = 0$, $\boldsymbol{v} = \mathbf{0}$
(c)	Symmetry boundary	$d_{\text{mesh}}/1.66$	1.1	$\partial_x s = 0,\ v_x = 0,\ \partial_x v_y = 0$
(d)	Symmetry center-line	$d_{\text{mesh}}/3.33$	1.02	$\partial_x s = 0$
(e)	Auxiliary line			
(f)	Symmetry center-line	$d_{\text{mesh}}/3.33$	1.02	$\partial_y s = 0$
(g)	Symmetry. center-point	$d_{\text{mesh}}/16.6$		$p = 0$

Mesh grid setup

For our COMSOL model we use a triangular mesh grid. The size of each element is controlled by defining its side length, and can vary across different areas in the domain. We therefore introduce a fixed length $d_{\text{mesh}} = \frac{W}{90}$, which is used to scale the various mesh sizes. The mesh structure used in the model is shown in figure 4.2. Naturally, the boundaries (b) and (c) require fine meshing, along with the symmetry lines (d) and (f). But the finest mesh is given in the center symmetry point (g), where the highest particle concentrations occurs. Furthermore, we define growth rates for the different parts of the domain. Growth rates control the maximum allowable rate with which adjacent mesh elements can grow.

By trial and error, mesh grid sizes and growth rates was chosen as shown in table 4.1.

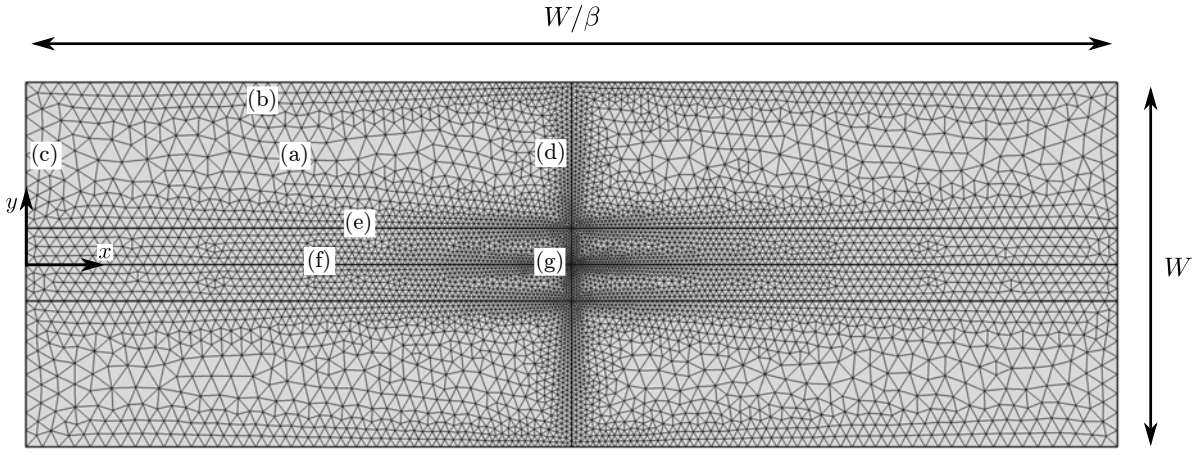

Figure 4.2: Top view: Two dimensional domain Ω of width W and length W/β used in the COMSOL model. (a)-(g) shows the different points, lines and areas, where boundary conditions and mesh sizes are imposed, see details in table 4.1. The mesh grid is shown for a very coarse mesh, being 10 times larger ($k_{\text{mesh}} = 10$), than that used in the calculations where $k_{\text{mesh}} = 1$. (a) Bulk, (b) wall boundary, (c) symmetry boundary, (d) and (f) symmetry center lines, (e) auxiliary line, (g) symmetry center point.

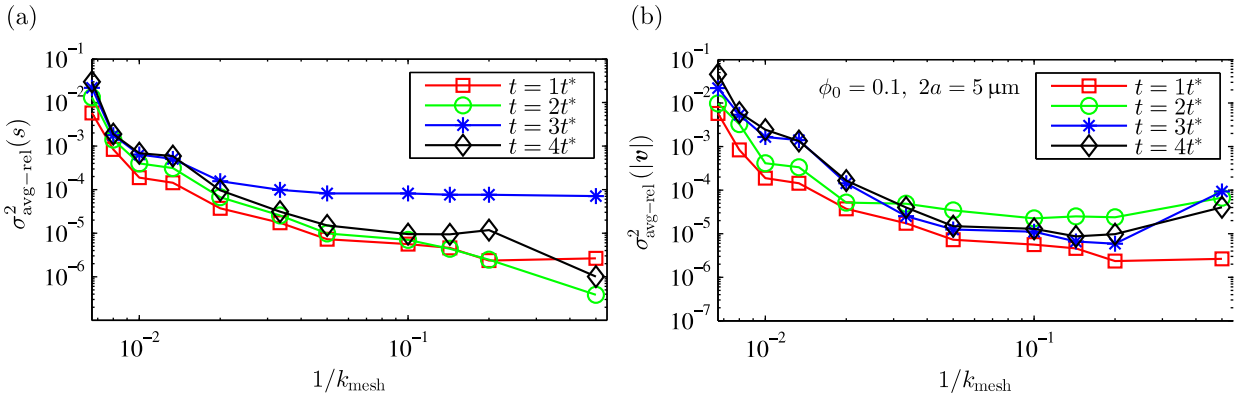

Figure 4.3: Mesh convergence plots of (a) the logarithmic concentration field s, and (b) the fluid velocity field $\boldsymbol{v}$. Plotted in terms of the relative variance $\sigma^2_{\text{avg-rel}}$, defined in Eq. (4.21). Both fields are plotted for four different times, and for the values $\{\phi_0, 2a\} = \{0.1, 5\,\mu\text{m}\}$. Note how the error on the fields increases slightly with increasing times.

4.4 Mesh convergence

The basic idea of mesh convergence analysis is to to check whether the numerical results have converged. If a sufficiently fine mesh grid is used, and convergence is achieved, the numerical results are independent of the mesh size d_{mesh}. Oppositely, if the mesh size is too coarse, spatial details cannot be resolved, making the numerical results a function of the mesh grid size d_{mesh}. It is therefore very important to identify the mesh size where numerical convergence is achieved.

To vary the different mesh sizes simultaneously, we introduce a dimensionless mesh scaling factor k_{mesh}, where $k_{\text{mesh}} = 1$ corresponds to the mesh presented in Table 4.1, implying a linear relation between k_{mesh} and the general mesh size.

To check the mesh convergence of an arbitrary field $X(\boldsymbol{r}, t)$, we introduce the average relative variance of the field $\sigma^2_{\text{avg-rel}}(X)$, where we use the solution with the finest mesh $X^{\text{end}}(\boldsymbol{r}, t)$ as reference, corresponding to $k_{\text{mesh}} = 1$

$$\sigma^2_{\text{avg-rel}}(X) \equiv \frac{\int_\Omega \mathrm{d}A\ \left(X - X^{\text{end}}\right)^2}{\int_\Omega \mathrm{d}A\ \left(X^{\text{end}}\right)^2}\,. \tag{4.21}$$

As our fields are time dependent, we need to run mesh convergence analyses for different times. In figures 4.3 and 4.4(a) we have plotted mesh convergence plots of logarithmic concentration s, velocity $\boldsymbol{v}$ and pressure p respectively. All plotted for the high volume concentration and intermediate particle size $\{\phi_0, 2a\} = \{0.1, 5\,\mu\text{m}\}$.

We note from the figures that mesh convergence is achieved for all fields, for mesh sizes well above $k_{\text{mesh}} > 1$. The logarithmic concentration field s, exhibits the largest relative variance of approximately $10^{-4} - 10^{-5}$, which implies that relative errors is seen at the second or third digits. Furthermore, we note that relative error increases with simulation times. This is expected, because more and more particles, accumulate close to $y = 0$, causing higher numerical errors as time passes.

4.4.1 Validity regimes

As we saw in the previous section, the relative error increases with simulation times, due to the accumulation of particles at $y = 0$. As the mesh convergence analysis was only run for one

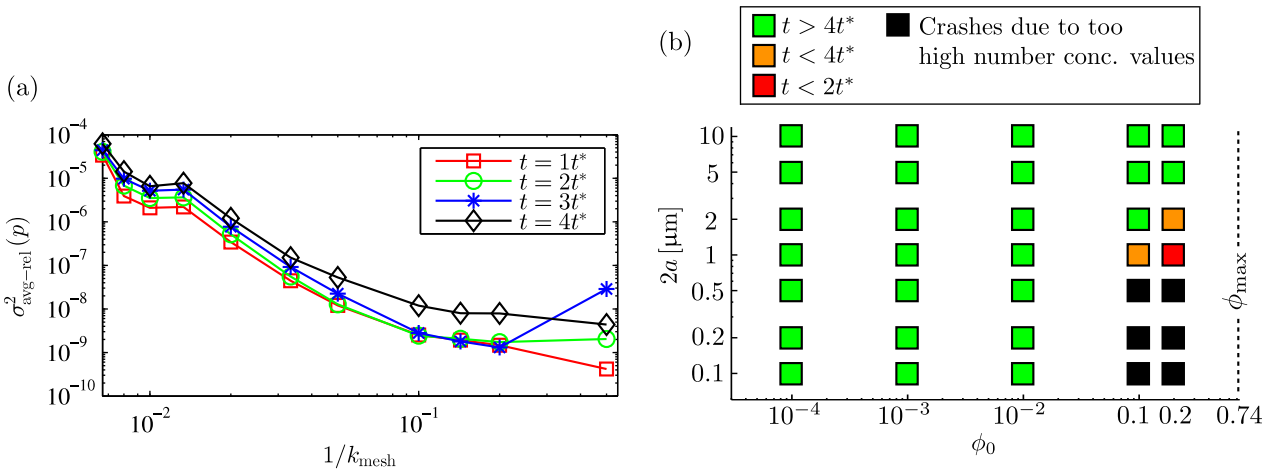

Figure 4.4: (a) Plot of the mesh convergence for the pressure field p, in terms of the relative variance $\sigma^2_{\text{avg-rel}}$, defined in Eq. (4.21). Plotted for four different times, and for the values $\{\phi_0, 2a\} = \{0.1, 5\,\mu\text{m}\}$. Note that the relative error goes up as we simulate for higher times. (b) Plot of numerically valid regimes for the numerical COMSOL model. The color coding denotes either rejection or approval of simulations for parameter sets $\{\phi_0, 2a\}$, based on the validity criteria defined in the text. Green: No problems observed for times well beyond $> 4t^*$, Orange: validity was achieved for times $t < 4t^*$, Red: validity was achieved for times $t < 2t^*$, Black: Numerical convergence was not achieved, due to the build-ups of too high numerical concentration gradients, eventually resulting in simulation crash.

set of parameters $\{\phi_0, 2a\}$, we need to know in what regimes of these values, we can expect the numerical model to be valid. We have therefore run simulations for various sets of initial volume concentration and particle size $\{\phi_0, 2a\}$, seen in Fig. 4.4(b). To determine the numerical validity, we rejected solutions where the structure of mesh elements was visible, or solutions that were clearly unphysical. Furthermore, COMSOLs internal convergence parameters correlated well with our performed mesh convergence analysis. On the basis of these criteria, we approved or rejected the numerical validity of various sets of values of $\{\phi_0, 2a\}$ for simulations times up to $t = \{2, 4\}\, t^*$. These times are chosen since most of the transient particle dynamics has happened within times of a few t^*. In Fig. 4.4(b) we have color coded the either rejected or approved simulations with parameter sets $\{\phi_0, 2a\}$: Green: No problems observed for times well beyond $> 4t^*$, Orange: validity was achieved for times $t < 4t^*$, Red: validity was achieved for times $t < 2t^*$, Black: Numerical convergence was not achieved, due to the build-ups of too high numerical concentration gradients, eventually resulting in simulation crash.

From Fig. 4.4(b) we see that the numerical model experiences difficulties only in the high concentration regimes $\phi_0 > 0.1$, and only for particle sizes $2a < 1\,\mu\text{m}$. This is due to the earlier mentioned fact of large particle accumulation at $y = 0$. Also, as the volume concentration goes up, and the particle size goes down, COMSOL is forced, in this formulation, to handle larger numerical values, eventually causing errors. In other words, significant numerical errors can be observed for this model for all parameter sets if simulating to long enough times. For experimentally relevant values of $\{\phi_0, 2a\}$, all behaviour of interest of the respective fields have occurred within times $\sim 10t^*$, implying that sufficient levels of numerical convergence are obtained for the purposes of our theoretical investigation.

4.5 Concluding remarks

In this chapter we implemented a numerical framework for solving our resulting governing equations, with the respective boundary conditions. We conclude that numerical convergence of the model is obtained for our purposes of investigation. Moreover, we showed that limits to the numerical convergence can be reached if simulating to long enough times. As such, we are now ready to extract results from the numerical model, but to ensure the physical correctness of the numerical model, we will in the next chapter compare the numerical model with with experimentally validated results in the non-interacting limit.

Chapter 5

Results - Non-interacting particle dynamics

In this chapter, we explore the particle dynamics in the case of no particle-particle interactions. Because acoustofluidic setups of the type we model in this thesis are very well characterised in the limit of dilute particle suspensions [24, 25, 36, 39, 43], this chapter serves two main purposes. Firstly, we use our numerical results in this limit to test against known theory and experimental results. This will give an indication to the physical reliability of the model in a well-known limit. Secondly, the results in this chapter serves as a benchmark to compare against for results including particle-particle interaction effects. This is vital, as we in this thesis aim to characterise, how particle-particle interactions will affect the particle dynamics, compared to the well known dilute limit.

5.1 Analytical model in the one-dimensional case

To make progress with analytical modeling, we first look at the concentration in only one dimension. Later this can be used to compare with numerical results.

The aim of this model, is to derive an expression for the particle concentration as function of time $c(\boldsymbol{r}, t)$ at $x = \frac{1}{2}W/\beta$, where there are no acoustic forces in the x-direction, see figure 3.3. In this case of no forces in the lateral direction, we can extend the result by Barnkob *et al.* [39], and obtain an analytical solution.

5.1.1 Concentration profile at $x = \frac{1}{2}W/\beta$

In section 3.4.1, we reviewed the result of Barnkob *et al.* [39], where they calculate the movement of a single particle in a transverse standing pressure wave.

Consider first a particle at y to time t, we calculate the starting position y_0 by inverting Eq. (3.17)

$$y_0(y,t) = \frac{W}{\pi} \arctan\left[\tan\left(k_y[y + W/2]\right) \exp\left(-\frac{t}{t^*}\right)\right] \qquad \text{for} \quad x = \frac{1}{2}W/\beta\,. \tag{5.1}$$

At $t = 0$, we assume the distribution of particles to be uniform $c(\boldsymbol{r}, 0) = c_0$. Next, we consider a thin cross-sectional slice of half the channel of length $\mathrm{d}x$, close to $x = \frac{1}{2}W/\beta$, with half-width $W/2$ and height H, sketched from a top-view in figure 5.1.

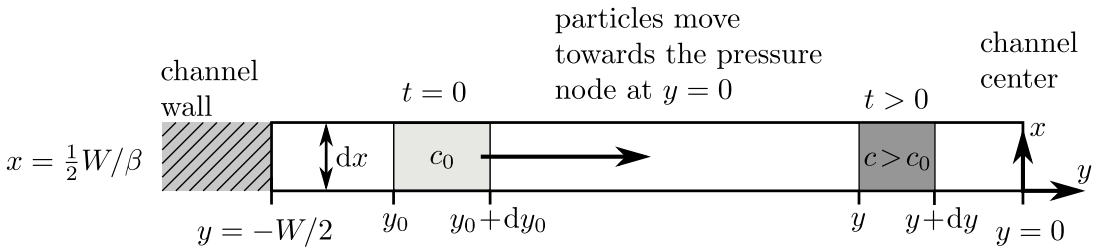

Figure 5.1: Sketch of top-view of a slice of the micro-channel of thickness $\mathrm{d}x$, height H and half channel width $W/2$, at the position $x = \frac{1}{2}W/\beta$. The number of particles $\mathrm{d}N$ between y_0 and $y_0 + \mathrm{d}y_0$ at time $t = 0$, must be conserved between y and $y + \mathrm{d}y$, at a later time t. Knowing the initial particle concentration c_0, the concentration at a later time $c(y, t)$ is found by relating $\mathrm{d}y_0$ and $\mathrm{d}y$.

We now consider another particle, starting just in front of the first particle in Eq. (5.1), with starting position $y_0 + \mathrm{d}y_0$, see fig. 5.1. The two particles, span a small volume element $\mathrm{d}V = H\,\mathrm{d}x\,\mathrm{d}y_0$. As the initial concentration is $c(\boldsymbol{r}, t) = c_0$ everywhere, the number of particles between the two particles, placed at y_0 and $y_0 + \mathrm{d}y_0$, can be calculated as

$$\mathrm{d}N = c_0\,\mathrm{d}V = c_0\,H\,\mathrm{d}x\,\mathrm{d}y_0 \qquad \text{for} \quad x = \frac{1}{2}W/\beta \quad \text{and} \quad t = 0\,. \tag{5.2}$$

As we are neglecting inertial effects, we know that the number of particles spanned by the two particles, is conserved at later time t, now positioned between $y(y_0, t)$ and $y(y_0 + \mathrm{d}y_0, t)$. This allows us to evaluate $\mathrm{d}y$ at position y at time t

$$\mathrm{d}N = c(y,t)\,H\,\mathrm{d}x\;[y(y_0 + \mathrm{d}y_0, t) - y(y_0, t)] = c(y,t)\,H\,\mathrm{d}x\,\mathrm{d}y(y_0, t)\,\big|_{y_0(y,t)}\;. \tag{5.3}$$

Equating the two expressions for the conserved number of particles $\mathrm{d}N$ Eqs. (5.2) and (5.3), we find that the concentration profile simply becomes the inverse derivative of $y(y_0, t)$

$$c(y,t) = c_0 \left(\frac{\mathrm{d}}{\mathrm{d}y_0} y(y_0, t)\Big|_{y_0(y,t)} \right)^{-1} \tag{5.4}$$

From Eq. (5.4), we note that if $\mathrm{d}y < \mathrm{d}y_0$ the concentration goes up $c(y, t) > c_0$, which is physically reasonable as the same number of particles is distributed over a smaller volume, and vice versa for $\mathrm{d}y > \mathrm{d}y_0$.

Carrying out the derivative in Eq. (5.4), inserting $y_0(y, t)$ from Eq. (5.1), and changing variable to the volume concentration $\phi(\boldsymbol{r}, t)$, we find

$$\phi\,(y,t) = 2\phi_0 \left[\sinh\left(\frac{t}{t^*}\right) \sin^2\left\{ \arctan\left[\tan\left(k_y(y + W/2)\right) \exp\left(\frac{-t}{t^*}\right) \right] \right\} + 1 \right] \quad \text{for} \quad x = \frac{1}{2}W/\beta\,. \tag{5.5}$$

Because this result is an extension of Barnkob *et al.* 's result in Eq. (3.17), which was largely validated experimentally [39], Eq. (5.5) can be used for comparison with the numerical results from COMSOL.

5.2 Two-dimensional analytical model

In the previous section we extended the result by Barnkob *et al.* [39] to find the non-interacting volume concentration as function of time $\phi(y, t)$ at $x = \frac{1}{2}W/\beta$. This was possible because we

neglected forces on the particles forces in the x-direction. In this section, we further extend this analysis, to be valid at other x co-ordinates.

Again, we neglect the lateral forces (which are down by a factor $\beta = 1/3$, see Eq. (3.12)). We note that y-dependence of $F_{\mathrm{ac},y}$, remains constant along the x-direction $\sin(2k_y y)$, see Eq. (3.12). Therefore, we can view the x-dependence of $F_{\mathrm{ac},y}$, as, simply a matter of modulating the amplitude of the radiation force $F_{\mathrm{ac}}(x)$, along the x-direction. From the vector field plot of $\boldsymbol{F}_{\mathrm{ac}}$ in figure 3.3, we see that the maximum force amplitudes occur at $(x, y) = \left(\frac{1}{2}W/\beta, \pm\frac{1}{4}W\right)$. Inserting $y = -W/4$ in Eq. (3.12), we find for the force amplitude of $F_{\mathrm{ac},y}$

$$F_{\mathrm{ac},y}(x) = 3V_{\mathrm{p}}E_{\mathrm{ac}}k_y \underbrace{\left[\frac{1}{3}f_1 \sin^2(k_x x) - \frac{1}{2}f_2^{\mathrm{Re}}\left\{\cos^2(\theta)\cos^2(k_x x) - \sin^2(\theta)\sin^2(k_x x)\right\}\right]}_{\Phi_{2\mathrm{D}}(x)} . \quad (5.6)$$

As indicated by the underbrace, we can view the x-dependence of $F_{\mathrm{ac},y}(x)$ as a 'pseudomodulation' of the 'two-dimensional' contrast factor $\Phi_{2\mathrm{D}}(x)$. Because $\Phi_{2\mathrm{D}}$ enters directly in the characteristic time scale t^*, see Eq. (3.18), we introduce the x-dependence directly into the characteristic time scale

$$\begin{aligned} t^*(x) &= \frac{3\eta}{4\Phi_{2\mathrm{D}}(x)k_y^2 a^2 E_{\mathrm{ac}}} \\ &= \frac{3\eta}{4k_y^2 a^2 E_{\mathrm{ac}}}\left[\frac{1}{3}f_1 \sin^2(k_x x) - \frac{1}{2}f_2^{\mathrm{Re}}\left\{\cos^2(\theta)\cos^2(k_x x) - \sin^2(\theta)\sin^2(k_x x)\right\}\right]^{-1} . \end{aligned} \quad (5.7)$$

This x-dependence, can be directly inserted in Eq. (5.5), giving the two dimensional concentration field if lateral forces $F_{\mathrm{ac},x}$ and diffusion are neglected $D = 0$

$$\phi(\boldsymbol{r}, t) = 2\phi_0\left[\sinh\left(\frac{t}{t^*(x)}\right)\sin^2\left\{\arctan\left[\tan\left(k_y(y + W/2)\right)\exp\left(\frac{-t}{t^*(x)}\right)\right]\right\} + 1\right] . \quad (5.8)$$

5.3 Concentration fields - non-interacting

In this section, we will compare the results from the analytical models from the two previous sections 5.1 and 5.2, with the numerical COMSOL model explained in section 4.2.2 and 4.3.

5.3.1 Concentration profiles at $x = \frac{1}{2}W/\beta$.

In the mesh convergence section 4.4, we showed that the numerical model has reached numerical convergence. However, in order to rely physically on the results we now compare our numerical model with the analytical results derived in Eqs. (5.5) and (5.8).

In Eq. (5.5) we derived the concentration profile $\phi(y, t)$ at $x = \frac{1}{2}W/\beta$, neglecting diffusion effects. This is plotted for different times $t = \{0.5, 1.0, 1.5, 2.0\}\, t^*$ in figure 5.2, where the dashed lines denote the analytical theory from Eq. (5.5), and the full lines denote the numerical solution by COMSOL of Eq. (3.29), in (a) without diffusion $D = 0$, and in (b) with diffusion $D > 0$.

In general, we see excellent agreement between the numerical and analytical model. Because diffusion is minute and no interaction effects are included, the concentration $\phi(\boldsymbol{r}, t)$ is independent of particle size ($2a$) and initial concentration ϕ_0. The first thing we note, is that the characteristic timescale t^* (see table 3.2) captures the behaviour of the particles. Within a few t^*, a large fraction of the particles have gathered at the transverse pressure node at $y = 0$. In

(a), where diffusion is neglected ($D = 0$), we expect to have the most direct comparison between analytics and numerics. We note a slight discrepancy between the two, emerging at $t = 2t^*$. This could be due to the fact that the initial particle dynamics close to $t = 0$ are slightly different in the analytical and numerical case. In the analytical expression Eq. (5.5) the acoustic radiation force $F_{\mathrm{ac},y}$ is applied exactly at $t = 0$, which stands in contrast to the numerical solution of Eq. (3.29), where the acoustic radiation force is applied with a step-function in time, centred around $t = 0$, to improve numerical stability. The stepping time is set to be much smaller than $t_{\mathrm{step}} \sim 10^{-4}t^* \ll t^*$, but this difference might account for the slight discrepancy between the analytical and numerical result for $t = 2t^*$ in Fig. 5.2(a).

In (b), diffusion is included ($D > 0$) for a particle of size $2a = 10\,\mu\mathrm{m}$. As expected , we generally see diffusion to play a minute role for the particle dynamics. However, at large concentrations, we expect diffusion to slightly "spread out" the particles, in contrast to the acoustic forces, trying to focus them. This is observed in (b) for $t = 2t^*$, where the peak value of ϕ is slightly lower than compared to its counterpart in (a). We believe the precise overlap between the analytical and numerical when including diffusion, to be a coincidence in this case.

5.3.2 Non interacting concentration fields

Having found good agreement between analytics and numerics at line of $x = \frac{1}{2}W/\beta$, we now turn to the full two-dimensional concentration fields $\phi(\boldsymbol{r}, t)$.

In Eq. (5.8), we calculated the concentration $\phi(\boldsymbol{r}, t)$ analytically, by neglecting transverse forces on the particles $F_{\mathrm{ac},x}$. It is of interest to see how well the analytical model in Eq. (5.8), compares against the numerical solution of Eq. (3.29), where effects of lateral forces $F_{\mathrm{ac},x}$ are easily included.

In Fig. 5.3 we have plotted the analytical result for $\phi(\boldsymbol{r}, t)/\phi_0$ from Eq. (5.8) for evolving times, and in Fig. 5.4 is shown its numerical counterpart of $\phi(\boldsymbol{r}, t)/\phi_0$ from solving Eq. (3.29), plotted for the same time values. Comparing the two figures, we see very little difference between the two. This implies that including only the transverse forces $F_{\mathrm{ac},y}$ on the particles when $\beta \leq 1/3$, captures much of the particle dynamics in the non-interacting case. However, we note the effects of the lateral forces $F_{\mathrm{ac},x}$ which is pushing the particles to the sides, This slightly visible in Fig. 5.4 (numerical) compared to Fig. 5.3 (analytical).

Inspecting Figs. 5.3 and 5.4, we see the particles accumulate in a ribbon of width $\sim 0.2W$, centred around $y = 0$. To the sides of the domain close to $x = 0$ and $x = W/\beta$, where the acoustic radiation force amplitudes go to zero, no focusing of particles takes place. This is expected, since no interaction takes place between particles.

Because we have observed the differences between the analytical and the numerical model to be very modest, we will now try quantify their differences more accurately, by introducing an integral criterion.

5.3.3 Non-interacting particle focusing

We define the number of particles in a ribbon of width $0.2W$, centred around $y = 0$ to time t as $N_{\mathrm{cen}}(t)$. This is sketched in figure 5.5(a). Normalising by the total number of particles $N = \frac{\phi_0}{V_{\mathrm{p}}} H\, W^2/\beta$, we define

$$\frac{N_{\mathrm{cen}}(t)}{N} \equiv \frac{H \int_{\mathrm{cen}} \mathrm{d}A\, \phi(\boldsymbol{r}, t)/V_{\mathrm{p}}}{N} = \frac{\beta V_{\mathrm{p}}}{\phi_0\, W^2} \int_0^{W/\beta} \mathrm{d}x \int_{-W/2}^{+W/2} \mathrm{d}y\, \phi(\boldsymbol{r}, t)\,. \tag{5.9}$$

Physically, $N_{\text{cen}}(t)/N$ expresses the fractional number of particles in the center ribbon of width $0.2W$. In figure 5.5(b), we have plotted $N_{\text{cen}}(t)/N$ for both the analytical and the numerical model. For times $t < 2t^*$, the number of particles in the center ribbon $N_{\text{cen}}(t)$ cannot almost not be told apart in the two models. However, for larger times $t > 2t^*$, we see that the numerical model, accumulates slightly fewer particles in the ribbon. This is due to the fact that the lateral forces on the particles $F_{\text{ac},x}$ pushes some of the particles to the side, away from $x = \frac{1}{2}W/\beta$, where the transverse forces $F_{\text{ac},y}$ are strongest. This makes the particles in the numerical model focus slower.

5.4 Concluding remarks

In this chapter, we have benchmarked the numerical COMSOL model against analytical models, in the regime of no particle-particle interactions. Excellent agreement between numerics and analytics was shown. Because the analytical model is an extension of an experimentally validated result [39], confidence can be gained in the COMSOL model proposed in this thesis. With these result in mind, we are now ready to investigate the results of the particle dynamics in the regime where particle-particle interactions become significant, and we can no longer rely on analytical results.

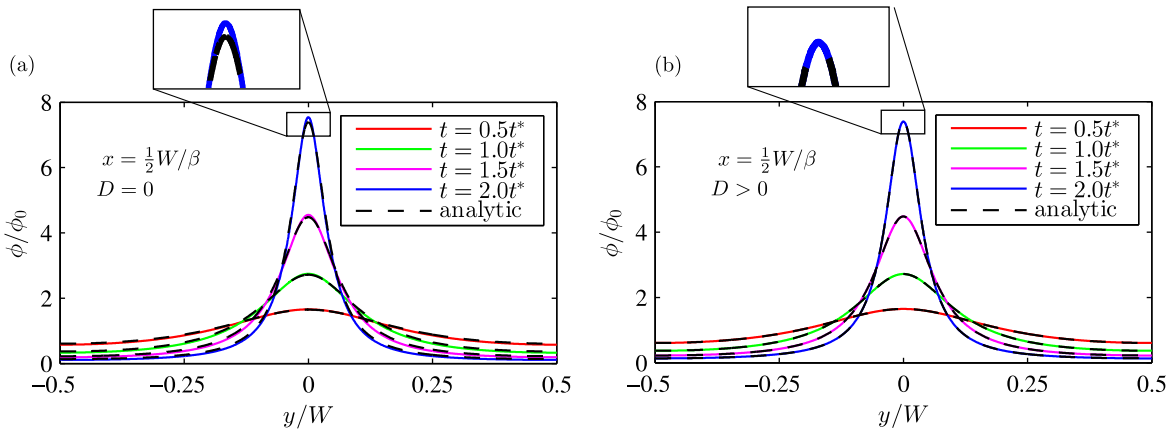

Figure 5.2: Plot of the volume concentration $\phi(y,t)$ at $x = \frac{1}{2}W/\beta$, compared to initial conc. ϕ_0, in the non-interacting case. The dashed lines, denote the analytical model (Eq. (5.5)), and the full lines denote the numerical solution of Eq. (3.29), plotted for different times. (a) Diffusion is neglected ($D = 0$), allowing for direct comparison between analytics and numerics. Note the slight discrepancy between the cases, emerging at $t = 2t^*$. (b) Diffusion effects are included for a particle of size $2a = 10\,\mu\text{m}$.

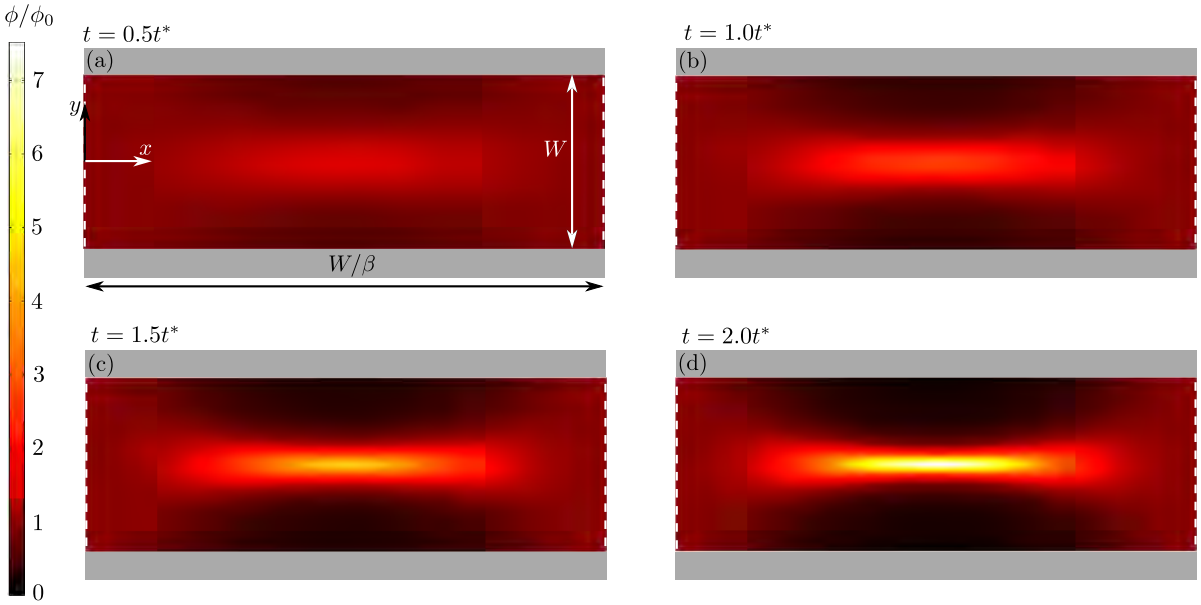

Figure 5.3: Analytical model of the concentration $\phi(\boldsymbol{r},t)/\phi_0$ for times $t = \{0.5, 1.0, 1.5, 2.0\}\,t^*$, derived in Eq. (5.8). The derivation disregards any forces on the particles in the lateral direction $F_{\text{ac},x}$, and neglects diffusion. The grey bars denote the channel walls, and the white dashed lines denote the periodic boundaries. Note the close resemblance with Fig. 5.4

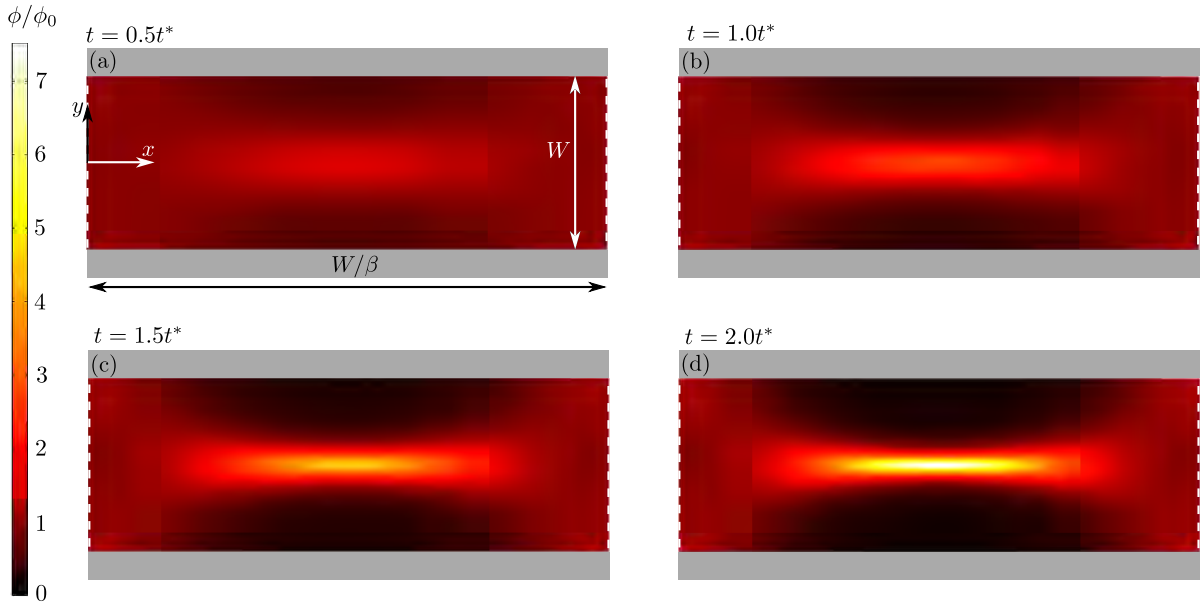

Figure 5.4: Numerical model of concentration $\phi(\boldsymbol{r}, t)/\phi_0$ for times $t = \{0.5, 1.0, 1.5, 2.0\}\, t^*$. The plots are derived numerically in COMSOL from solving Eq. (3.29), with boundary conditions in Eq. (3.31). The grey bars denote the channel walls, and the white dashed lines denote the periodic boundaries. As time goes, the particles accumulate in a ribbon of thickness $\sim 0.2W$, centered around $y = 0$. Note the close resemblance with Fig. 5.3

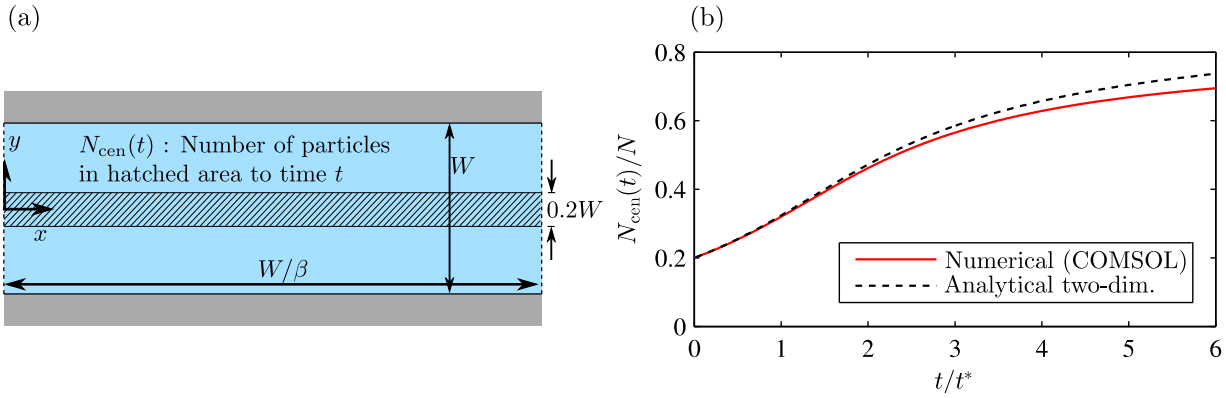

Figure 5.5: (a) Graphical illustration of the number of particles $N_{\text{cen}}(t)$, defined in Eq. (5.9), and N is the total number of particles. (b) Plot of the fractional number of particles in the center ribbon $N_{\text{cen}}(t)/N$, defined in Eq. (5.9), and shown in (a), as function of time. The dashed line denotes the analytical model, found by integrating Eq. (5.8) and the dashed line denotes the integral of the numerical solution of Eq. (3.29). We see that for times $t < 2t^*$, almost no difference in focusing is observable.

Chapter 6

Results - Interacting particle dynamics

In this chapter we investigate the interacting particle dynamics, with the particle-particle interaction effects, we discussed and modelled in Section 3.6. To understand the behaviour of the various fields: concentration ϕ, fluid velocity $\boldsymbol{v}$ and pressure, we plot, for comparison all fields to the time $t = t^*$. As discussed in Section 3.6.3, we expect the initial volume concentration ϕ_0 and the particle size $2a$ to be the important scaling parameters for the hydrodynamic interaction effects. For this reason, we initially plot all fields in the four regimes sketched in Fig. 6.1.

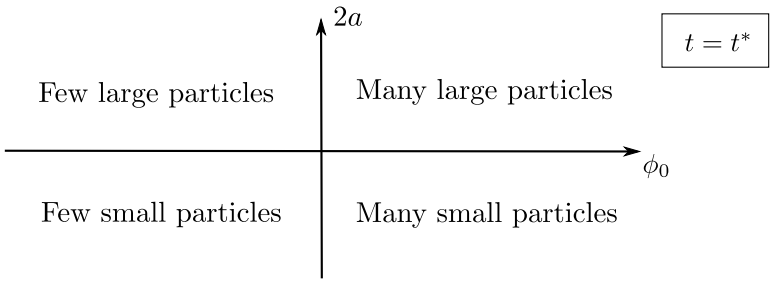

Figure 6.1: Principal co-ordinate system, spanning the important scaling parameters in the study of interaction effects in the particle dynamics.

The four regimes, will be spanned by the values

$$\text{spanning values:} \quad \phi_0 = \{10^{-5}, 0.1\} \quad \text{and} \quad 2a = \{1, 10\}\,\mu\text{m}\,. \tag{6.1}$$

In Section 3.4.2 we defined the critical streaming particle size $2a_{\text{str}} \approx 2\,\mu\text{m}$. For particle larger than this value, acoustic streaming effects could be neglected. Since experimentally relevant particle sizes are approximately $< 10\,\mu\text{m}$, we take this as the upper particle size. Since we want to investigate a significant differences in particle size, we choose $2a = 1\,\mu\text{m}$ as the smallest particle size, even if it is strictly below $2a_{\text{str}}$. It is therefore important to disclaim that streaming effects will significantly influence the particle dynamics in an actual experiment for $2a = 1\,\mu\text{m}$. However, it remains relevant in the sense of understanding the nature of interaction effects of different particle sizes. For the initial volume concentration ϕ_0, we choose $\phi_0 = 0.1$ as maximum, because higher volume concentrations can causes clogging of the microchannel in the experimental setup. At $\phi_0 = 10^{-5}$, the average particle-particle distance is $d_{\text{p-p}}/2a = 41$ (see Fig. 3.5), and we expect particle-particle interactions to be negligible. By presenting results for these "extreme" values we aim to understand the differences of the particle dynamics in the

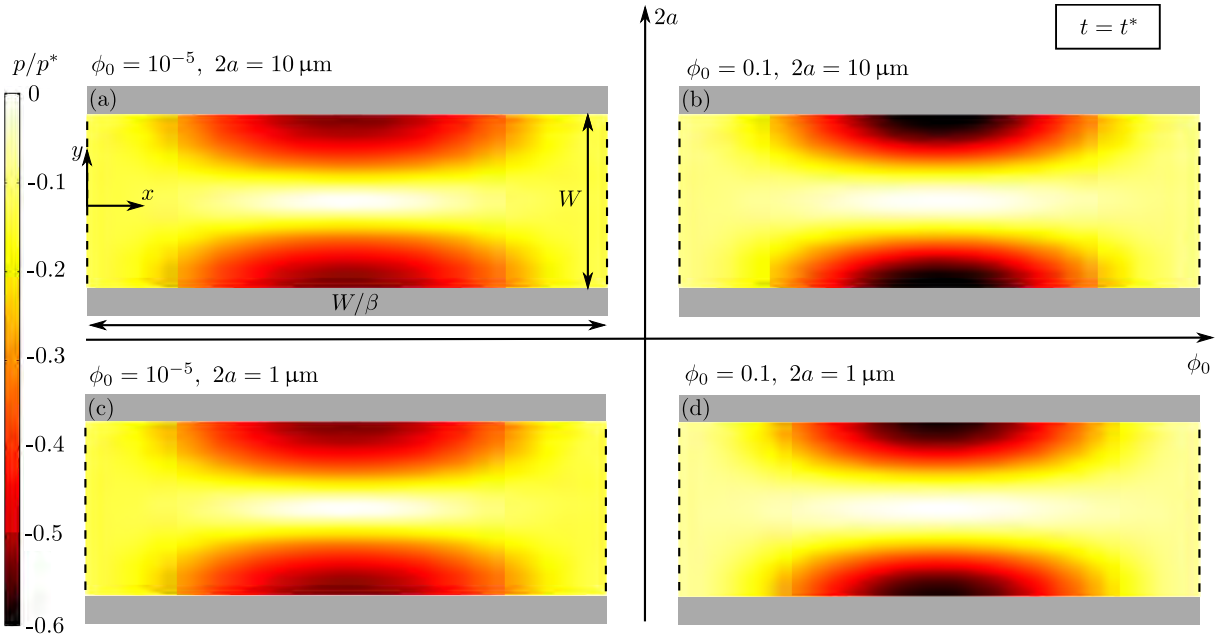

Figure 6.2: Plot of the fluid pressure p, in terms of the characteristic pressure p^*, see Table 3.2. All plots are for the time $t = t^*$. The pressure is shown in four different regimes of volume concentration ϕ_0 and particle size $2a$, see Eq. (6.1). Large pressure gradients build up in the y-direction, relieving the external volume forces on the fluid, exerted by the particles. The grey bars and the vertical dashed lines, denote the channel walls and periodic boundaries, respectively.

interacting versus the non-interaction case. Knowing how the system behaves differently in the interacting regime, we define critical values $(\phi_0^c, 2a^c)$ for which we predict the particle focus time towards the channel center (see Fig. 5.5(a)) to have doubled compared to the dilute limit.

6.1 Fluid velocity and pressure fields

6.1.1 The fluid pressure p

To visualize the resulting pressure fields, we have in Fig. 6.2 plotted the pressure p in the four different regimes, of initial concentration ϕ_0 and particle size $2a$, as indicated in Eq. (6.1). All are plotted at time $t = t^*$.

In general, we see qualitatively very little difference of the pressure p, in the four regimes. Quantitatively, we see that the maximum pressure difference, is slightly bigger in the high concentration regime $\phi_0 = 0.1$. We confirm that large pressure gradients build in the transverse direction, and note that the pressure force $-\boldsymbol{\nabla} p$, points from center $y = 0$, towards the channel walls. This is expected, since we argued in Section 3.6.3 that a lot of the external forces on the fluid $c\boldsymbol{F}_{\text{ac}}$, could be relieved by hydrostatic pressure forces $-\boldsymbol{\nabla} p$. This assumption is further confirmed in the fact that all pressure values lies between $-0.6p^*$ and 0, implying that the essential physics for the pressure p, is captured by the characteristic pressure p^*, see Table 3.2

6.1.2 The fluid velocity $\boldsymbol{v}$

In Fig. 6.3, we have plotted the fluid velocity $\boldsymbol{v}$, for the usual values of initial concentration ϕ_0 and particle size $2a$, listed in Eq. (6.1). Again for times $t = t^*$

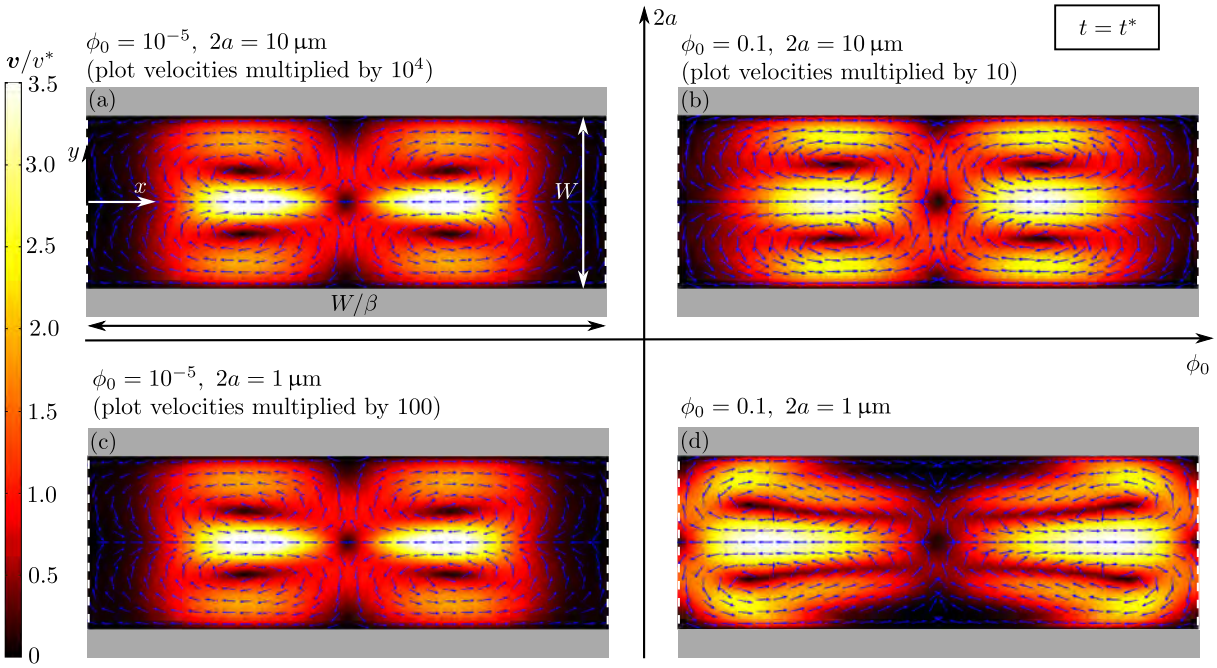

Figure 6.3: Plot of the fluid velocity $\boldsymbol{v}$, in terms of the characteristic fluid velocity v^*, see Table 3.2. The color denotes the magnitude of the velocity, and the blue arrows denote the direction. All plots are for the time $t = t^*$. The velocity is shown in four different regimes of initial concentration ϕ_0 and particle size $2a$, listed in Eq. (6.1). Note that the velocity magnitudes span over 5 decades and the plot velocities in (a), (b) and (c) are multiplied different factors in order to be visible on the figure. The multiplication factors are: (a) 10^4, (c) 100, (b) 10 and (d) 1. Note how the direction of the fluid *convection rolls* in (b) and (d), are from the walls towards the center at $y = 0$, and vice versa in (a) and (c). The grey bars and the vertical dashed lines, denote the channel walls and periodic boundaries, respectively.

In general, we see qualitatively similar behaviour of the fluid velocity $\boldsymbol{v}$ in all four regimes. To understand the pattern of the velocity field $\boldsymbol{v}$, we consider at first, only Fig. 6.3(b). As the particles are pushed towards the transverse pressure node at $y = 0$ (see Fig. 3.4), the particles drag the fluid along. Because the acoustic radiation force is strongest at $x = \frac{1}{2}W/\beta$, a *convection rolls* is established with the fluid flowing from the channel sidewalls and towards the pressure node at $y = 0$. These flow rolls will essentially help the particle transport from the bulk, and towards the center at $y = 0$. Considering all the subfigures in Fig. 6.3, the careful reader might notice that the convection rolls are flowing in opposite directions for $\phi_0 = 10^{-5}$, compared to $\phi_0 = 0.1$: in Fig. 6.3 (a) and (c) the fluid is flowing from the transverse pressure node at $y = 0$, and towards the walls. And vice versa for Fig. 6.3 (b) and (d). This difference is explained in detail in Section 6.3 as it is a result of the transient particle dynamics, taking place in the channel. In Section 6.3, it will also become clear why the shape of the convection roll in (d), is slightly different compared to the others.

In order to compare the fluid velocity magnitudes in Fig. 6.3(a)-(d) we have multiplied the velocity magnitudes in (a),(b) and (c) by factors of $10^4, 10$ and 10^2, respectively, for them to visible in the plot. Quantitatively, we the see the velocity amplitudes in Fig. 6.3 span over five decades of amplitude, in terms of the characteristic fluid velocity, chosen as the maximum particle convection velocity $v^* = u_\mathrm{p}$. The lowest velocities are seen in Fig. 6.3(a), where the amplitudes on the plot are multiplied by 10^4, to make the velocity magnitudes visible. The highest amplitudes are observed in (d), where the velocities approximately reflect the characteristic fluid velocity $v \sim v^*$. As the number of particles goes up, so does the number of point forces acting on the fluid. It therefore reasonable to find the largest fluid velocity magnitudes v, in the regime with large volume concentration ϕ_0, and smallest particle size $2a$, giving the highest number of particles N.

6.2 Concentration fields

In Fig. 6.4, we have plotted the volume concentration ϕ, for the usual values of initial concentration ϕ_0 and particle size $2a$, listed in Eq. (6.1). All for times $t = t^*$.

In general, we see the qualitative similar behaviour of the concentration fields ϕ in of the four regimes (a)-(d). In the center at$x = \frac{1}{2}W/\beta$ where $\boldsymbol{F}_\mathrm{ac}$ are strongest the particle are again pushed towards the transverse pressure node at $y = 0$, and very little activity is observed to the sides at the vertical symmetry lines. In the high concentration regime, see (b) and (d), we observe a qualitative difference between the fields. For the case of small particles in (d) where the fluid convection rolls have high velocities compared to large particles in (b), see Fig. 6.3(b) and (d), the convection rolls have squeezed the concentration profile at $y = 0$ more flat and to the sides compared to (b).

Quantitatively, large differences are observed. We see that in the high concentration regime $\phi_0 = 0.1$, see (b) and (d), the particle focusing is much slower compared to the dilute regime $\phi_0 = 10^{-5}$, in (a) and (c). This is due to the drastically decreased particle mobility. At $\phi = 0.1$, the relative mobility is down by a factor $\chi(0.1) = 0.332$, compared to $\chi(10^{-5}) = 0.97$, see Eq. (2.31). To quantify the influence of the various interaction effects more accurately, we derive the effective particle focusing in Section 6.3 in analogy with Fig. 5.5(b).

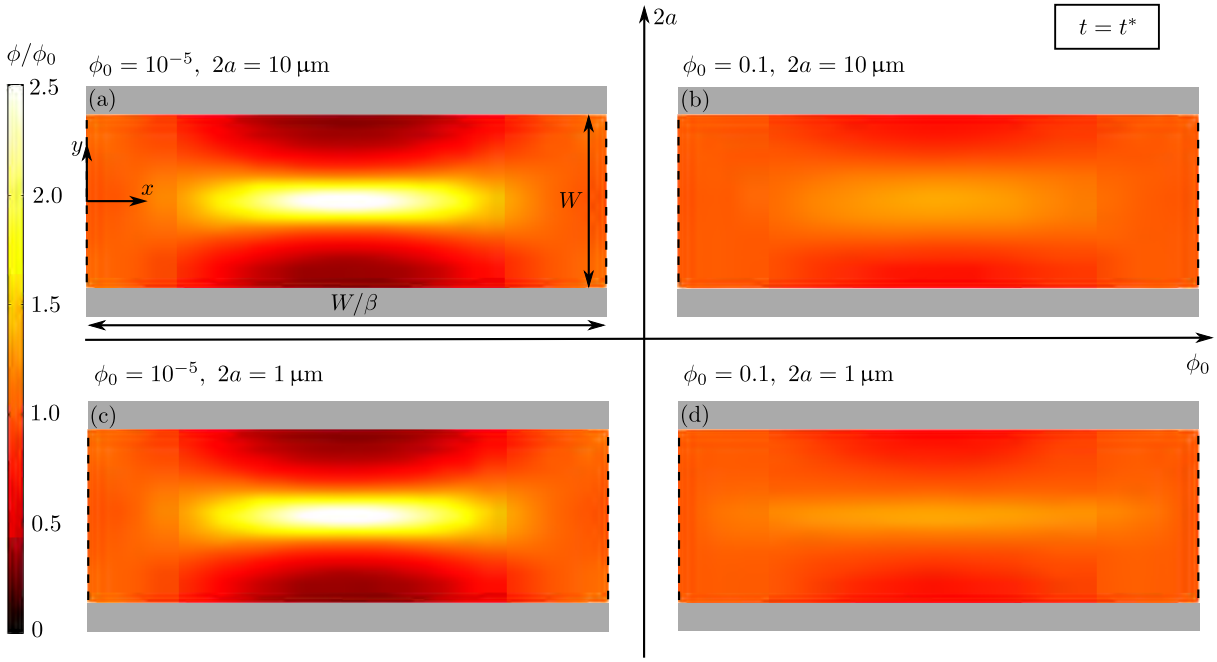

Figure 6.4: Plot of the volume concentration ϕ, in terms of initial concentration ϕ_0. All plots are for the time $t = t^*$. The concentration is shown in four different regimes of volume concentration ϕ_0 and particle size $2a$, see Eq. (6.1). In all caes, particles are pushed towards the transverse pressure node, at $y = 0$. In the high concentration regime $\phi_0 = 0.1$, (b) and (d), particles are seen focus a lot slower, compared to the dilute regime, see (a) and (c). The grey bars and the vertical dashed lines denote the channel walls and the periodic boundaries, respectively.

6.3 Particle dynamics over time

In order to understand the different flow directions and shapes of the fluid velocity fields $\boldsymbol{v}$, discussed in Section 6.1, we must look closer at the transient development of the concentration ϕ and fluid velocity $\boldsymbol{v}$.

We therefore plot corresponding concentration ϕ and fluid velocities $\boldsymbol{v}$, for evolving times $t = \{0.625, 1.25, 1.875, 2.5, 3.125\}t^*$, for the values $(\phi_0, 2a) = (10^{-3}, 5\,\mu\text{m})$. This is shown in Fig. 6.5.

In Fig. 6.5(b) at time $t = 0.625t^*$ we see that a convection roll is established with the fluid flowing in direction from the channel walls, and towards $y = 0$. This is caused by particles, being driven from the bulk of the fluid, towards the center $y = 0$. The effect is seen in (a), where we start to see the bulk fluid, slowly being emptied for particles. As the bulk fluid is continuously emptied for particles (c), the "driving force" $c\boldsymbol{F}_{\text{ac}}$ of the convection roll, begins to weaken, causing the convection roll to slightly change shape, and move to the sides (d). Going back to Fig. 3.3, we closely inspect the radiation force $\boldsymbol{F}_{\text{ac}}$, close to the center point $(x, y) = \left(\frac{1}{2}W/\beta, 0\right)$. On the line where $y = 0$, we see modest forces in the x-direction, towards the center point. As particles are continuously accumulating at exactly this line segment, see Fig. 6.5(e), the force on the fluid in the x-direction towards the center point $c\,F_{\text{ac},x}$, continues to grow in strength. This causes the formation of a new convection roll (f), now flowing in the opppsite direction, compared to earlier (a). As particles are accumulated further (g), the counter-flowing convection rolls gain in strength, and the original convection roll (a) begin to die out (h). Eventually, the

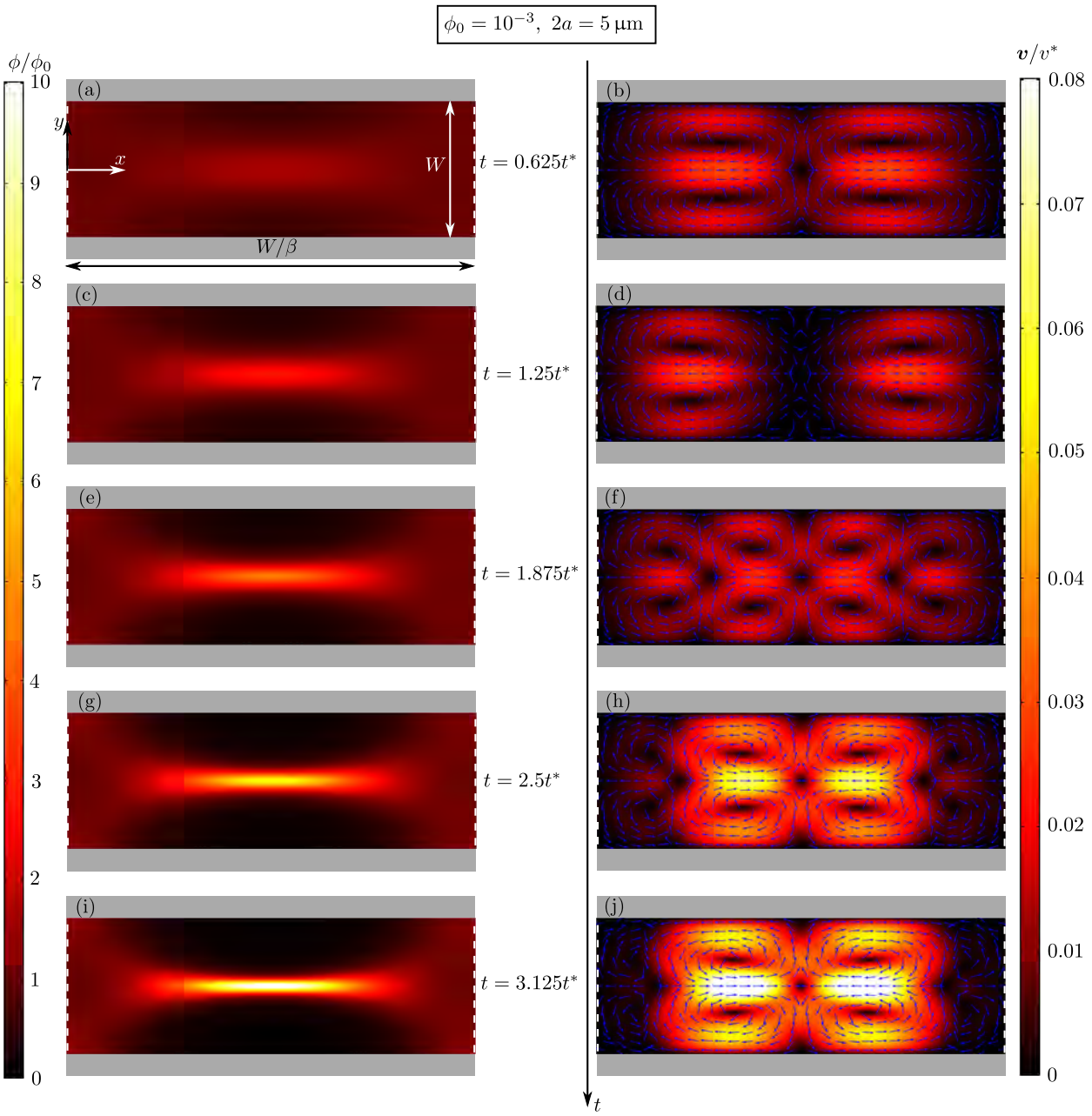

Figure 6.5: Corresponding plots of volume concentration ϕ and fluid velocity $\boldsymbol{v}$, for evolving times $t = \{0.625, 1.25, 1.875, 2.5, 3.125\}t^*$, denoted by the vertical time axis. All plotted for the values of initial concentration and particle size $(\phi_0, 2a) = (10^{-3}, 5\,\mu\text{m})$. At first (a) one convection roll appears due to the forces from the particles. As time passes, the first flow is initially replaced by another counter-flowing convection roll (j), due to the build-up of lateral forces at the transverse pressure node $y = 0$. A full description of the sequence of events seen in the figure is given in the text of Section 6.3. The grey bars and the dashed vertical lines denote the channel sidewalls and periodic boundaries, respectively.

counter-flowing convection roll will overtake the whole velocity field (j).

This transient behaviour explains the difference in convection rolling direction, seen in Fig. 6.3. At time $t = t^*$, the particle focusing in the high concentration regime $\phi_0 = 0.1$, see Fig. 6.4(a), (c) compared to Fig. 6.4(b), (d), has not yet emptied enough particles in the bulk fluid to stop the original flow roll. In terms of convection roll "phases", the velocity fields in Fig. 6.3(b) and (d), are still in the "phase" depicted in Fig. 6.5(a). The different form of the convection roll shape of Fig. 6.3(d), can now also be understood, as it is beginning to move slighty to the side, corresponding to the "phase" shown in Fig. 6.5(d). We saw in Fig. 6.4 that particles focus much faster in the dilute regime $\phi_0 = 10^{-5}$ due to the much higher relative particle mobility $\chi(10^{-5}) = 0.97$ compared to $\chi(0.1) = 0.332$. This explains why the dilute regime velocity fields in Fig. 6.3(a) and (c) already at time $t = t^*$ have focused enough particles to be in the last "convection roll phase", shown in Fig. 6.5(j).

6.4 The Influence of different interaction effects

In Fig. 6.4, we saw that the time scale for particle focusing in the interacting regime, was far slower compared to the non-interacting case. To quantify the differences more precisely, we examine how fast particles are focused to the transverse pressure node at $y = 0$. For this, we reuse the concept of fractional number of particles in the center $N_{\text{cen}}(t)/N$ defined in Eq. (5.9) and sketched in Fig. 5.5(a). By using the same values of initial concentration ϕ_0 and particle size $2a$ as listed in Eq. (6.1), we plot $N_{\text{cen}}(t)/N$ in the four regimes. This will clarify how the various hydrodynamic interaction effects influences the focus time.

Since we have introduced different particle-particle interaction mechanisms, it will be useful to study their impact individually. InFig. 6.6 we have plotted $N_{\text{cen}}(t)/N$ in the four different regimes listed in Eq. (6.1) with separated interaction effects. All plotted for times $t \in [0, 4t^*]$.

Red curves: no interaction effects, solving Eq. (3.29) with quiescent fluid $\boldsymbol{v} = \mathbf{0}$ and unchanged particle mobility $\chi = 1$.
Blue curves: Interacting through decreased particle mobility, solving Eq. (3.36a) with quiescent fluid $\boldsymbol{v} = \mathbf{0}$, but modified particle mobility $\chi < 1$.
Green curves: Particles interaction only through the velocity field, solving Eqs. (3.36a), (3.37) and (3.38) with $\boldsymbol{v} \neq \mathbf{0}$ but unchanged particle mobility and effective viscosity $\chi = \psi = 1$.
Magenta curves: All interaction effects, solving Eqs. (3.36a), (3.37) and (3.38) with $\boldsymbol{v} \neq \mathbf{0}$, $\chi < 1$ and $\psi > 1$.

In the non-interacting regime $\phi_0 = 10^{-5}$ (see (a) and (c)), we wee that all four curves, collapse on the same curve, confirming that the particle transport is well described by the single particle theory in Eq. (3.29). In the interacting regime $\phi_0 = 0.1$ (see (b) and (d)), we clearly see drastic changes in the particle focusing. Comparing the red and the green curves, we see that the coupling to the fluid velocity $\boldsymbol{v}$, has very little influence on the particle focusing before $t < 2t^*$. At larger times, the fluid velocity $\boldsymbol{v}$ does have some influence: because the fluid is "whirling" the particles around, it is able to transport particles from the sides, close to the symmetry lines at $x = \{0, W/\beta\}$, to the center at $x = \frac{1}{2}W/\beta$, where the acoustic radiation forces are strongest, after which they are focused. As expected, this effect is more pronounced for the smaller particles $2a = 1\,\mu\text{m}$ where higher fluid velocities $\boldsymbol{v}$ are had, see Fig. 6.3. Comparing the red and green curves in (d) for times $t < 2t^*$ in (d), we see by careful inspection that the curves cross twice. Before $t < t^*$, the convection roll direction is slightly "aiding" the particle transport towards the transverse pressure node, thus, the green curve has the highest value. This changes after $t \gtrsim t^*$ because the convection roll direction reverses, thereby slightly "slowing" the particle focusing causing the red curve to have the highest value.

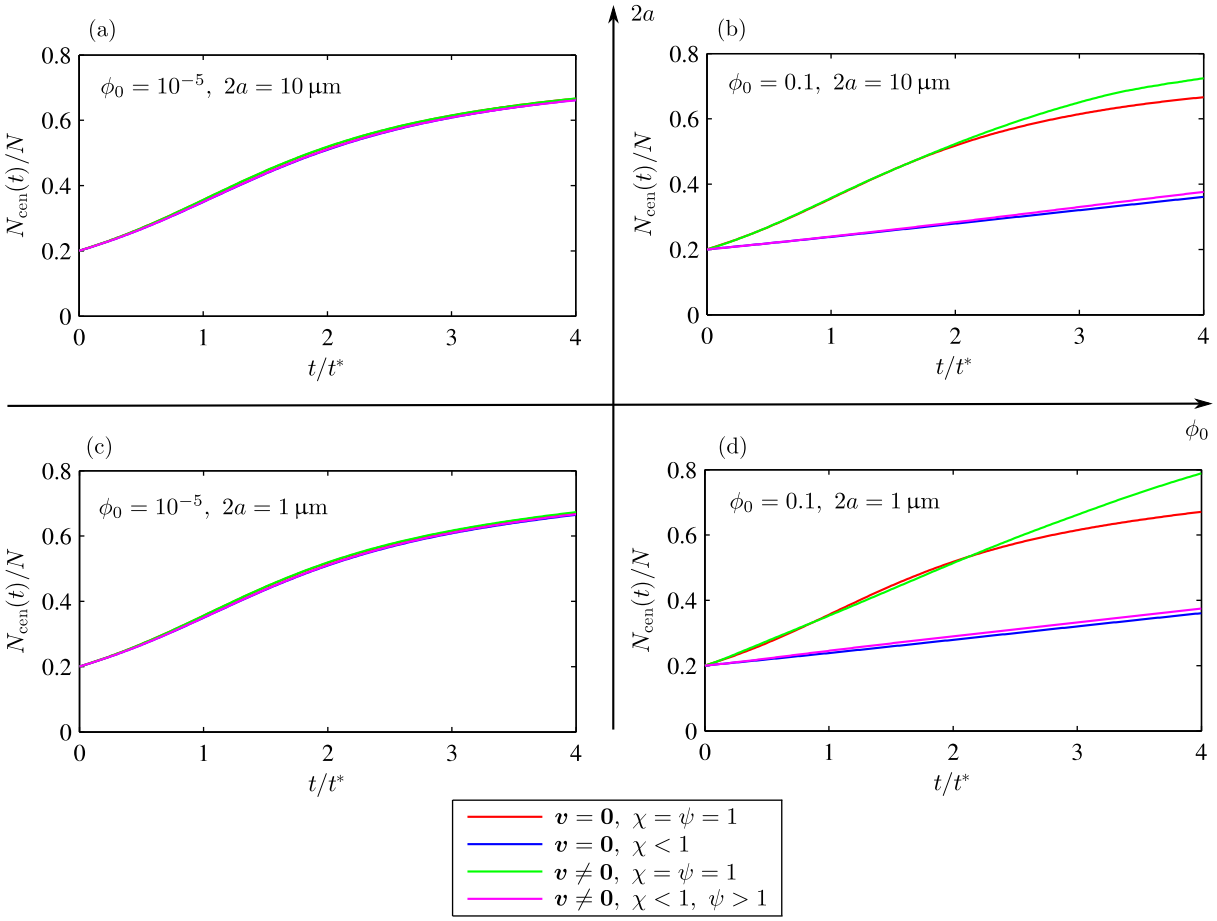

Figure 6.6: Plot showing particle focusing in the center ribbon of width $0.2W$ sketched in Fig. 5.5(a). Plotted as fractional number of total particles $N_{\text{cen}}(t)/N$ defined in Eq. (5.9). (a)-(d) show for the four regimes of initial volume concentration ϕ_0, and particle size $2a$, listed in Eq. (6.1).The different colors represents the inclusion of one or more particle-particle interaction mechanisms. The various curves are: **Red:** no interaction effects, solving Eq. (3.29) with quiescent fluid $\boldsymbol{v} = \mathbf{0}$ and unchanged particle mobility $\chi = 1$. **Blue:** Interacting through decreased particle mobility, solving Eq. (3.36a) with quiescent fluid velocity $\boldsymbol{v} = \mathbf{0}$, but modified particle mobility $\chi < 1$. **Green:** Particles interaction through the velocity field, solving Eqs. (3.36a), (3.37) and (3.38) with $\boldsymbol{v} \neq \mathbf{0}$ but unchanged particle mobility and effective viscosity $\chi = \psi = 1$. **Magenta:** All interaction effects, solving Eqs. (3.36a), (3.37) and (3.38) with $\boldsymbol{v} \neq \mathbf{0}$, $\chi < 1$ and $\psi > 1$.

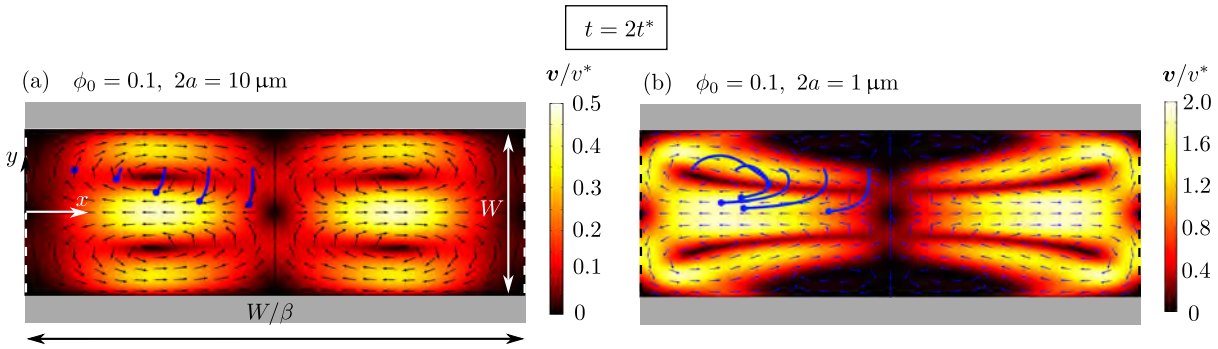

Figure 6.7: Simulation of five particle trajectories for times $t \in [0, 2]\ t^*$ in the regime of high volume concentration $\phi_0 = 0.1$ for two different particle sizes: (a) $2a = 10\,\mu\text{m}$ and (b) $2a = 1\,\mu\text{m}$. The trajectories are denoted by blue lines, and the circle denote their end position at $t = 2t^*$. As background is plotted their respective fluid velocity fields at the last timestep in the simulation $t = 2t^*$. The grey bars and the dashed vertical lines denote the channel sidewalls and the periodic boundaries, respectively. Note the difference fluid velocity magnitudes in the two plots, giving rise to very different particle trajectories.

Inspecting all four curves in (b) and (d), we see that the decreased particle mobility $\chi(0.1) = 0.322$ (blue and magenta) is the most dominant effect for the *net* particle transport in our case. Comparing the red and green curves with the blue and magenta curves in Fig. 6.6(b) and (d), we that the particle focusong speed for times $t < 2t^*$ are looks to down by approximately a factor three. Very little difference is seen between the blue and the magenta curves, which means that including the coupling to the fluid velocity $\boldsymbol{v}$ on top of decreased particle mobility effects ($\chi > 1$) does not yield a large difference in net particle movement.

Particle movement

From Eq. (3.36b), we recall that the convective and acoustic drift contributions to the particle current density $\boldsymbol{J}_\text{p}$, were comparable by the velocities $\boldsymbol{v}$ and $\chi(\phi)\,\boldsymbol{u}_\text{ac}$. Having chosen the characteristic fluid velocity as $v^* = u_\text{ac}$, we note that the fluid velocity in Fig. 6.3(d), reaches values $v = 3.5v^* = 3.5u_\text{ac}$. In this light, it seems counter intuitive that the inclusion of convection effects $\boldsymbol{v} \neq \boldsymbol{0}$, make so little difference in the net focusing of particles, see blue and magenta curves in Fig. 6.6(d). To investigate this intuitive discrepancy, we have simulated the trajectory of five particles in the high concentration regime $\phi_0 = 0.1$ for two particle sizes $2a = \{1, 10\}\,\mu\text{m}$ for the times $t \in [0, 2]\ t^*$. Due to their difference in fluid velocity magnitudes, see Fig. 6.3(b) and (d), different particle trajectories are expected. The particle trajectories for the five particles are plotted in Fig. 6.7 along with the corresponding fluid velocity fields $\boldsymbol{v}$ for time $t = 2t^*$.

From Fig. 6.7, we see that the five particles have quite different different trajectories for the two different particle sizes. In (a) we see the particles primarily move towards the transverse pressure node at $y = 0$, and are only slightly affected by the fluid convection. For the small particles $2a = 1\,\mu\text{m}$ in (b), the picture is quite different, the particles strongly affected by fluid convection, carrying them along while simultaneously being slightly pressed towards $y = 0$. This simulation clearly explains why the net transport of the particles are almost the same, with and without fluid convection. When including fluid convection, additional particles get "whirled in", like the ones we see in Fig. 6.7(b). This stands in contrast to (a), where the outermost particles remains almost stationary. However, as additional particles get "whirled in", a number of particles also get "whirled out" in return, almost cancelling the additional

particle contribution. This gives us the following physical picture. In the weakly convecting case Fig. 6.7(a), the particles experience a steady focusing towards the pressure node, compared to the strongly convecting case Fig. 6.7(b), where the particles are in net, also being transported towards $y = 0$, but are undergoing a "rolling motion", as they do so. This explains why very little difference is seen between the concentration fields in Fig. 6.4(b) and (d) since no velocity information is revealed by concentration values.

The overall conclusion is therefore that the hydrodynamic coupling is crucial for describing the behaviour of small particles in the high concentration regime, but for the purposes of net particle focusing in our geometry, the net effect is minute. We therefore propose a new characteristic time scale for the particle focusing τ^*, involving the change in relative particle mobility

6.4.1 Timescale for particle focusing τ^*

Based on the discussion in the previous section of the observed changes in particle dynamics at high volume concentration, we propose a new characterstic *mobility* timescale for the particle transport, involving the relative mobility decrease of the initial volume concentration

$$\tau^* \equiv \frac{t^*}{\chi(\phi_0)}\,, \tag{6.2}$$

Here, our usual characteristic timescale t^* is given by Eq. (3.18), and the relative particle mobility is given by Eq. (2.31). For our present cases of $\phi_0 = \{10^{-5}, 0.1\}$, the mobility timescales become $\tau^* = \{1.03, 3.1\}t^*$, respectively. Using this timescale instead of t^*, we can collapse all 16 curves from Fig. 6.6, into one plot, see Fig. 6.8.

We use the same color notation as in Fig. 6.6. The line symbols denote the parameter sets of initial concentration ϕ_0, and particle size $2a$. We note that blue and magenta curves for $\phi_0 = 0.1$, were not successfully simulated beyond times $\approx 1.8\tau^*$. This was due to build-ups of too high numerical concentration gradients, making COMSOL unable to simulate for longer times with our current model.

For times shorter than $t < t^*$, the rescaling captures the particles dynamics as all curves almost collapse to a single line. For longer times, we see the blue and magenta lines for $\phi_0 = 0.1$, start deviating slightly from the other curves. This is due to the fact that mobility is not constant in the simulation, but changes with the local volume concentration $\phi(\boldsymbol{r})$. The spatial variations make particles focus overall slower, than predicted by the mobility timescale τ^*. We conclude that the mobility timescale τ^* implemented here captures the overall essence of particle focusing dynamics of the different interaction effects.

6.5 Critical regions for particle-particle interactions

Until now, we have only looked at extreme parameter values for particle size $2a$, and volume concentration ϕ_0. This has allowed us to build intuition as to how concentrated suspensions are expected to behave, compared to the well characterised dilute suspensions. However, we have thus so far no insight into when particle-particle interactions become significant for the particle behaviour. To investigate this, we introduce a particle focus time t_{foc}. We denote the fractional number of particles that the non-interacting particle dynamics Eq. (3.29) is able to focus in $t = 1\,t^*$ as $N_{\text{foc}}/N = N_{\text{cen}}(t^*)/N$, i.e the value of the red curves at $t = t^*$ in Fig. 6.6 which is found to be $N_{\text{foc}}/N = 0.3204$. From this we define the focus time $t_{\text{foc}}(\phi_0, 2a)$ as the time it takes, using the parameter set $\{\phi_0, 2a\}$, to focus N_{foc}/N particles when including all interactions effects, given by the magenta curves in Fig. 6.6. This will reveal how much slower the particle

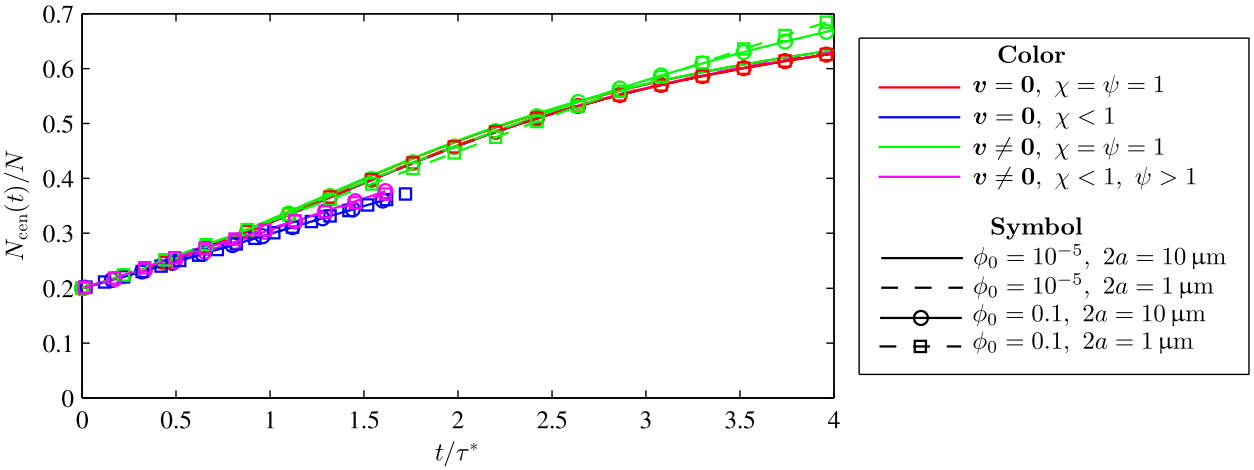

Figure 6.8: Data collapse of all 16 curves from Fig. 6.6 in one plot, using the timescale τ^*, defined in Eq. (6.2). The **colors** denote: **Red:** no interaction effects, solving Eq. (3.29) with quiescent fluid $\boldsymbol{v} = \mathbf{0}$ and unchanged particle mobility $\chi = 1$. **Blue:** Interacting through decreased particle mobility, solving Eq. (3.36a) with quiescent fluid velocity $\boldsymbol{v} = \mathbf{0}$, but modified particle mobility $\chi < 1$. **Green:** Particles interaction through the velocity field, solving Eqs. (3.36a), (3.37) and (3.38) with $\boldsymbol{v} \neq \mathbf{0}$ but unchanged particle mobility and effective viscosity $\chi = \psi = 1$. **Magenta:** All interaction effects, solving Eqs. (3.36a), (3.37) and (3.38) with $\boldsymbol{v} \neq \mathbf{0}$, $\chi < 1$ and $\psi > 1$. The **symbols** denote the specific parameter set of initial volume concentration ϕ_0 and particle size $2a$, see Eq. (6.1). Note that all curves for $\phi_0 = 10^{-5}$ have collapsed on the red line. Note that blue and magenta curves, for $\phi_0 = 0.1$, were not successfully simulated beyond times of $1.8\tau^*$.

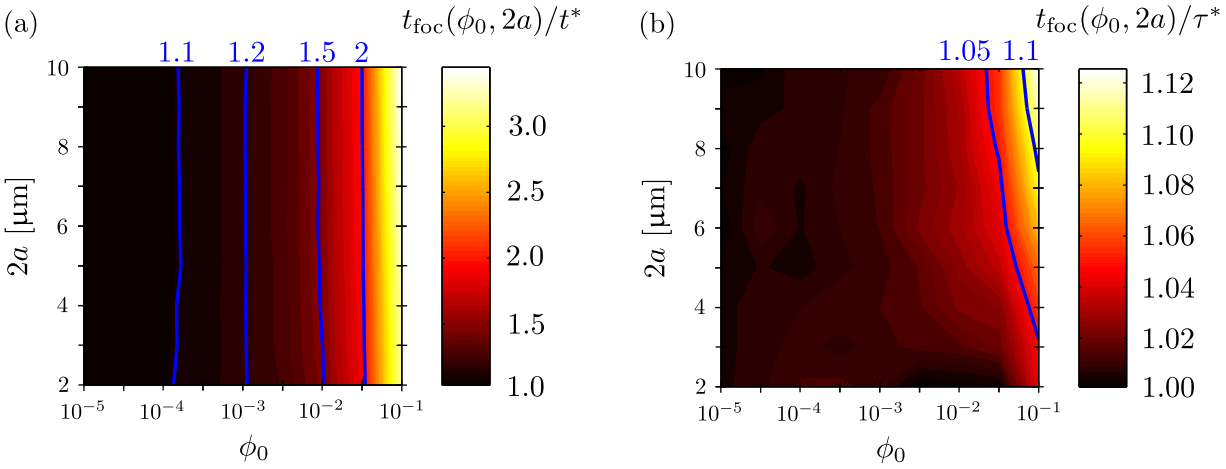

Figure 6.9: Contour plot of the particle focusing time $t_{\text{foc}}(\phi_0, 2a)$, defined as the time it takes to focus the same number of particles, when including all interactions for the values $\{\phi_0, 2a\}$, as the non-interacting particle dynamics is able to in the time $t = t^*$. I.e t_{foc} is the time it takes for the magenta curves in Fig. 6.6, to reach the value of the red curves at $t = t^*$. The plots are based on 81 parameter sweeps of $\{\phi_0, 2a\}$. (a) Plotted in terms of t^*, see Eq. (3.18), and (b) in and in terms of τ^*, see Eq. (6.2). Blue contour lines are shown, revealing when particle-particle interactions become increasingly significant for the particle focusing time. In (b) we begin to see the influence in focus times for different particle sizes $2a$ as we scale the times with the mobility time scale τ^*.

Table 6.1: Summary of the approximate initial volume concentration values ϕ_0 where the the particles focusing time t_{foc} increases to certain values, see Fig. 6.9(a). Given along with the corresponding average particle-particle distance in terms of particle diameter $d_{\text{p-p}}/2a$, see Eq. (3.26).

t_{foc}/t^*	1.1	1.2	1.5	2.0
ϕ_0	2×10^{-4}	1×10^{-3}	1×10^{-2}	3×10^{-2}
$\frac{d_{\text{p-p}}}{2a}$	14	8	3.2	1.9

focusing becomes, compared to the dilute limit, from including the particle-particle interactions assumed in this thesis. Based on $9 \times 9 = 81$ parameter sweeps of $\{\phi_0, 2a\}$, we have in Fig. 6.9 plotted $t_{\text{foc}}(\phi_0, 2a)$, in the regime of interest, though above the critical particle streaming size $2a_{\text{str}} = 2\,\mu\text{m}$.

From Fig. 6.9(a) where t_{foc} is plotted in terms of t^*, we see that the particle size $2a$ has very little influence on the particle on the overall focusing time, making the blue contour lines practically vertical. We note by the blue contour lines that a 10% percent increase in the particle focusing time is achieved at $\phi_0 \approx 2 \times 10^{-4}$, which is remarkable. The initial volume concentrations approximately corresponding to the blue contour lines in Fig. 6.9(a), is listed in Table 6.1, with corresponding average particle-particle distances $d_{\text{p-p}}$ (see Eq. (3.26)). We conclude from the blue contour lines that the critical initial volume concentration where the focus time has initially doubled $t_{\text{foc}} = 2t^*$ is approximately $\phi_0^{\text{c}} \approx 0.03$. No specific critical particle size $2a^{\text{c}}$ can be determined from our findings as the focus time is seen to depend almost solely on the volume concentration ϕ_0.

We confirm from Fig. 6.9(a) that at an initial volume concentration of $\phi_0 = 0.1$, the focusing time have increased approximately a factor three, corresponding to the description of the characteristic mobility time τ^*, defined in Eq. (6.2). To see the difference in particle size, we have in (b), plotted the focusing times in terms of τ^*. In general we see only slight deviations from the scaling by τ^*, by little over 12%. However, we confirm that particle focusing times are slightly faster for smaller particles, as the effect of fluid convection slightly increases the acoustophoretic focusing speed.

6.6 Concluding remarks

In this chapter we presented results for the behaviour interacting particle dynamics. All results was presented in four regimes: dilute and concontrated suspensions, for both small and large particles. As a general result we conclude that the overall particle dynamics slows down for increasing volume concentration ϕ_0. Using the notion of focus time t_{foc}, defined in Section 6.5 , we find that the critical initial volume concentration to be approximately $\phi_0^{\text{c}} = 0.03$. We find the effects of fluid convection to be important in the description of the particle dynamics for concentrated suspensions. However, for the geometry and acoustic fields investigated here the net gain in particle focusing due to convection, proved to be minute. In the next chapter we draw perspective to these results by comparing with experimental data, and we discuss strengths and weaknesses of the model in the light of these findings.

Chapter 7

Comparison with preliminary experiments and discussion

In this chapter we aim to see the results presented so far, as well as the thesis work as a whole, in an objective and broader perspective. In the aim of giving an experimental perspective we have as a part of this thesis work designed and made preliminary experiments in collaboration with an experimental group at Faculty of Engineering at Lund University, as the first basic steps in experimental validation.

We discuss some physical effects that has been omitted in the theoretical treatment, as well the strength and weaknesses of our proposed model framework. On the basis of these discussions, we will make suggestions for further work.

7.1 Comparison with preliminary experiments

As a part of this thesis work, we have collaborated with an experimental group at Faculty of Engeneering at Lund University (LTH), headed by professor Thomas Laurell. In particular we have collaborated with postdoc Kevin Cushing. The design and treatment of these experiments should be seen as the first basic steps, in the experimental investigation of particle-particle interactions of micro-particle acoustophoresis, and are as such an addition to the main modelling work of this thesis. All raw data and experiments were performed by post doc Kevin Cushing, LTH, and all data analysis and processing were performed by the author.

7.1.1 Experimental setup

The experimental setup is identical to that described in Chapter 3, with channel width $W = 373\,\mu\text{m}$, length $L \sim 4$ cm, and height $H = 157\,\mu\text{m}$, see Fig. 3.1. In the experiment we identified a part of the acoustofluidic channel, where the lateral modulation of the acoustic fields takes place over a few channel widths $\sim 3W$. Next, particle suspension were made polystyrene particles of sizes $2a = \{1, 3, 5\}\,\mu\text{m}$ with volume concentrations $\phi_0 = \{0.001, 0.01, 0.1\}$. To properly "see" all the particles in the channel, it proved a good solution to have a small fraction of the particles to be coated with a fluorescent dye. In order to later characterise the many particle dynamics, we first characterised the acoustic fields in the dilute limit

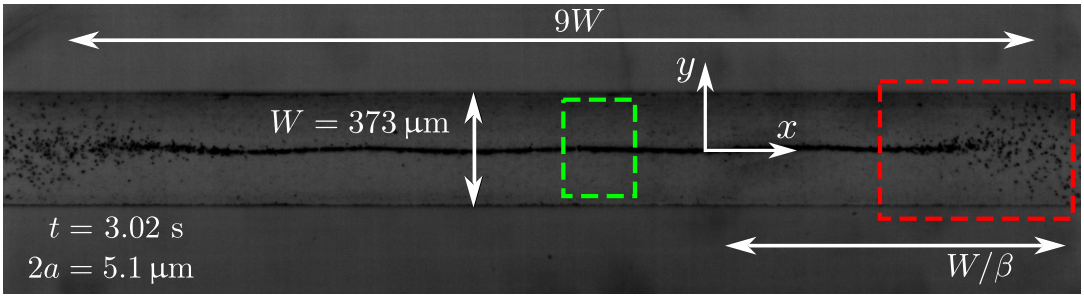

Figure 7.1: Polystyrene particles of size $2a = 5.1\,\mu\text{m}$ are focused to the transverse pressure node in the center, at a chosen location in the channel, giving an estimate of the lateral modulation of the acoustic fields. The image is taken after time $t = 3.02$ s. The full length of the lateral modulation takes place on a length scale of approximately $9W$, and the local modulation is seen to happen on a length scale similar to β/W. The green and red rectangles denote areas we use for investigation in this and the next subsection. Raw image courtesy of Kevin Cushing, LTH.

7.1.2 Characterisation of the acoustic field

The acoustofluidic channel is operated at a peak-to-peak voltage of $V = 7.4$ V at a frequency of $f = 1.96$ MHz. To estimate the lateral modulation of the acoustic fields, we focus a number of polystyrene particles of size $2a = 5.1\,\mu\text{m}$, and examine the particle distribution after $t = 3.02$ s, see Fig. 7.1.

From the particle distribution in Fig. 7.1, we see that the full length of the lateral modulation, happens on a length scale of approximately $9W$. The local modulation of the ultrasound, from strong to weak, see red dashed rectangle in Fig. 7.1, takes place on a length scale, similar to what have been assumed earlier $\sim W/\beta$.

In order to be able to find the characteristic timescale t^* we calculated the acoustic energy density E_{ac} from measurements. To do this, we examined the transient focusing of $2a = 5.1\,\mu\text{m}$ polystyrene particles where the acoustic radiation forces are strongest, denoted by the green dashed rectangle in Fig. 7.1. 14 image frames from $t = 0$ to $t = 350$ ms were analysed in the of area of the green rectangle in Fig. 7.1. A close up of the particle focusing in the green rectangle is shown for two different times in Fig. 7.2(a) and (b).

We used a Matlab toolbox called PTVlab [44] to track and evaluate the velocities of the particles. Since the particle velocities are proportional to the acoustic radiation forces $\boldsymbol{u}_{\text{p}} \propto \boldsymbol{F}_{\text{ac}}$, we can represent the particle velocities by a time independent velocity field, being a function of position only $\boldsymbol{u}_{\text{p}}(x, y)$. In the area of the green dashed rectangle, we averaged the particle velocities over 14 frames, and plotted y-component of the velocity $u_{\text{p},y}(x, y)$ in Fig. 7.2(c). Within the green dashed area we assume two things: 1) No lateral modulation $\partial_x \boldsymbol{u}_{\text{p}}(x, y) \approx \boldsymbol{0}$, and 2) The first-order pressure p_1 has the form of a standing half-wave in the y-direction, as sketched in Fig. 3.1. Thus, the wave numbers become $(k_x, k_y) = (0, \pi/W)$. From Eqs. (3.12) and (3.13) the acoustic radiation force reduces to

$$\boldsymbol{F}_{\text{ac}}(y) = 3\frac{\pi}{W} V_{\text{p}} E_{\text{ac}} \Phi \sin(\pi y/W)\, \boldsymbol{e}_y\,. \tag{7.1}$$

By balancing the acoustic radiation force with the unmodified drag force for a quiescent liquid $\boldsymbol{F}_{\text{d}} = -6\pi\eta a u_{\text{p},y}(y)\, \boldsymbol{e}_y$ (see Eq. (3.16)), we find the acoustic energy density

$$E_{\text{ac}} = \frac{2\eta a u_{\text{p},y} W}{\Phi V_{\text{p}}}\,. \tag{7.2}$$

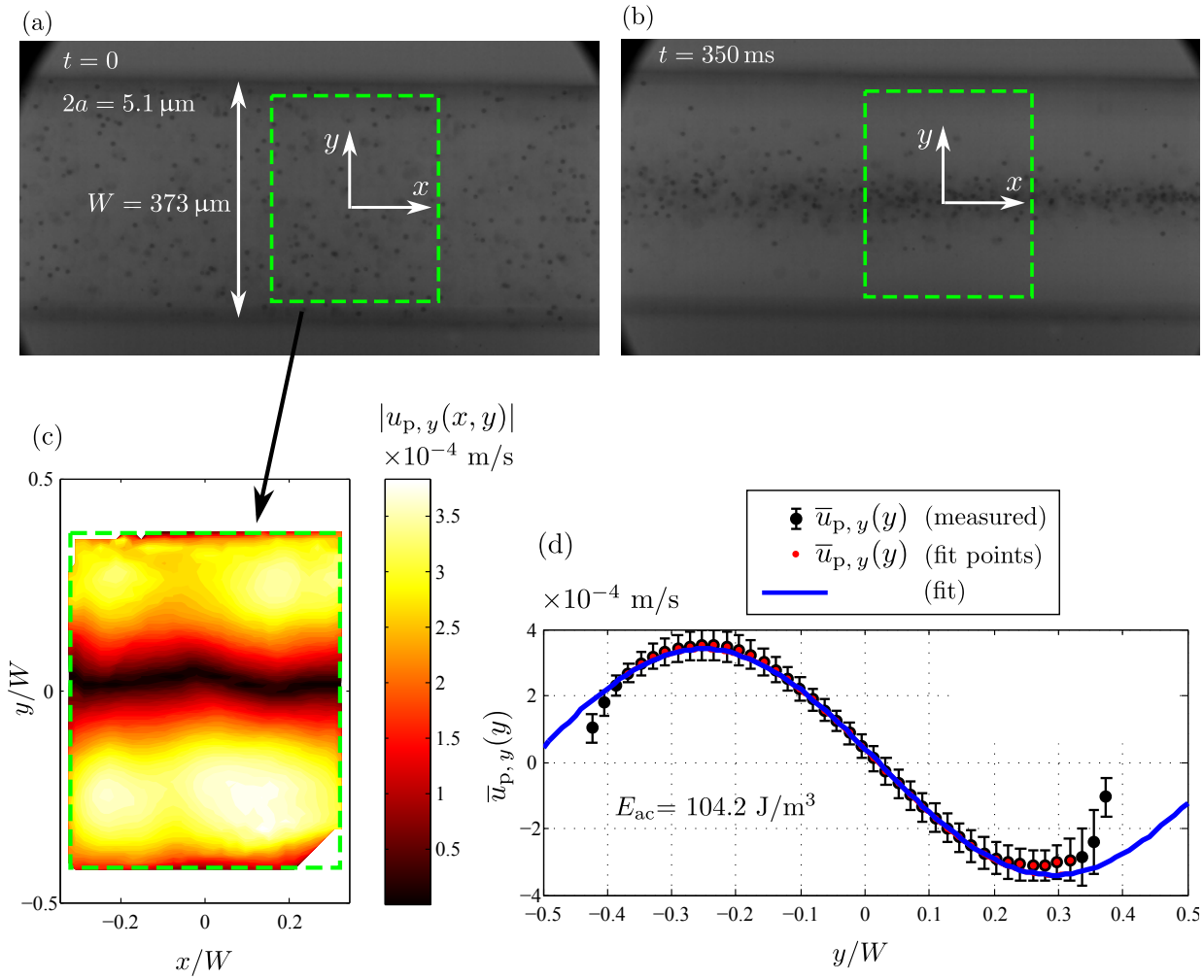

Figure 7.2: (a) and (b) : The particle velocities are measured inside the area of the green rectangle, also shown in Fig. 7.1. Particle velocities $\boldsymbol{u}_{\text{p}}$ are evaluated between 14 image frames, spanning between $t = 0$ (a) and $t = 350$ ms (b), raw image data courtesy of Kevin Cushing, LTH. By particle tracking in Matlab [44], the time averaged y-component over 14 image frames of the particle velocities $u_{\text{p},y}(x, y)$, are plotted in (c). The average value of $u_{\text{p},y}(x, y)$ is taken over the x-direction in (c), to find the mean value $\overline{u}_{\text{p},y}(y)$ and standard deviation, plotted in (d), denoted by black dots and error bars. Lastly, a sine curve (blue line) is fitted to the center data points (red dots), determing the velocity amplitude $u_{\text{p},y}$.

Note that we have let the identical sine dependencies of $u_{\mathrm{p},y}(y)$ and $\boldsymbol{F}_{\mathrm{ac}}$, drop out, leaving only the amplitudes. By the taking the average of $u_{\mathrm{p},y}(x,y)$ over the x-direction, we find the average velocity $\overline{u}_{\mathrm{p},y}(y)$ and the standard deviation which is plotted in Fig. 7.2(d), denoted by the black dots and errorbars. Close to the channel edges at $y \pm W/2$, the velocities $u_{\mathrm{p},y}$ deviate from the expected shape a sine function due to increases in drag forces from the nearby walls [45, 43]. We therefore omit these outermost datapoints, denoted by full black dots. Lastly, we find the amplitude velocity $u_{\mathrm{p},y}$, by fitting the red dotted data points to a sine curve (blue line) as seen in Fig. 7.2(d). By insertion of the amplitude $u_{\mathrm{p},y}$ in Eq. (7.2) we find the acoustic energy density as $E_{\mathrm{ac}} = 104\,\mathrm{J/m^3}$, which in turn allows us to determine the characteristic time scale t^* for various particle sizes (see Eq. (3.18)).

7.1.3 Behaviour of particles in different concentration regimes

To investigate the effects of particle-particle interactions in microfluidic acoustophoresis we recall that polystyrene particle suspension were made with particles of sizes $2a = \{1, 3, 5\}\,\mu\mathrm{m}$, and with volume concentrations $\phi_0 = \{0.001, 0.01, 0.1\}$. Unfortunately, time has not permitted rigorous quantitative analysis of the experimental data, but instead we will here present some qualitative findings. In Fig. 7.3 we show an image series of acoustophoretic particle-focusing for times $t = \{5, 10, 15, 20\}\,t^*$ for two particle suspension with *different* initial concentration, but same particle size $2a = 5\,\mu\mathrm{m}$. In Fig. 7.3(a)-(d): Concentrated suspension $\phi_0 = 0.1$ and in (e)-(h): Semi-dilute suspension $\phi_0 = 0.001$. The focusing of both suspensions is carried out in the same spot of the channel, namely in the red dashed region in Fig. 7.1 where the acoustic radiation force is seen to fan out. The images are seen from a top-view through the glass lid (see Fig. 3.1), and the full image series from $t = 0$ to $t = 20t^*$ consists of 70 images.

First and foremost, we experimentally confirm from Fig. 7.3 that the particle focusing in the concentrated regime $\phi_0 = 0.1$ in (a)-(d), happens on a much longer timescale, compared to the dilute suspension (e)-(h). The prolonged focus time for the concentrated suspension, corresponds approximately to what we expect from our model, namely that the focusing time has increased several times, compared to the semi dilute suspension $\phi_0 = 0.001$ in (e)-(h), see Fig. 6.9.

Particle movement during focusing

By inspection of both image series, we have manually tracked three different, easily identifiable, clusters of particles, and marked them by symbols (○, □ and △). The arrows and dotted lines denote the local particle velocity and approximate trajectories, respectively. For the concentrated suspension $\phi_0 = 0.1$ (a)-(d) all symbols are given in light blue ○, □ and △, and the for dilute suspension $\phi_0 = 0.001$ (e)-(h) all symbols are shown in red ○, □ and △.

In the case of the dilute suspension $\phi_0 = 0.001$, see (e)-(h), we see as expected that the particles go towards the transverse pressure node, with very little convective effects from the fluid. A slight drift to the left is observed for the particles at the pressure node, see ○ in (g). Because the particles at the right hand side of images (e)-(h) remains largely at rest, the mentioned drift in the center is not due to a Poiseuille flow in the channel, but probably more likely a hydrodynamic interaction effects. To understand this drift effect, investigation over the full area in Fig. 7.1 is needed. We note that the focusing happens on very long timescales $\sim 20t^*$, compared to what we expect from this set of parameters, see Fig. 6.5. This may be because the the acoustic radiation forces $\boldsymbol{F}_{\mathrm{ac}}$ are weaker than what we expect from employing standing wave in both directions (see Fig. 3.3), which we assumed in our numerical simulations.

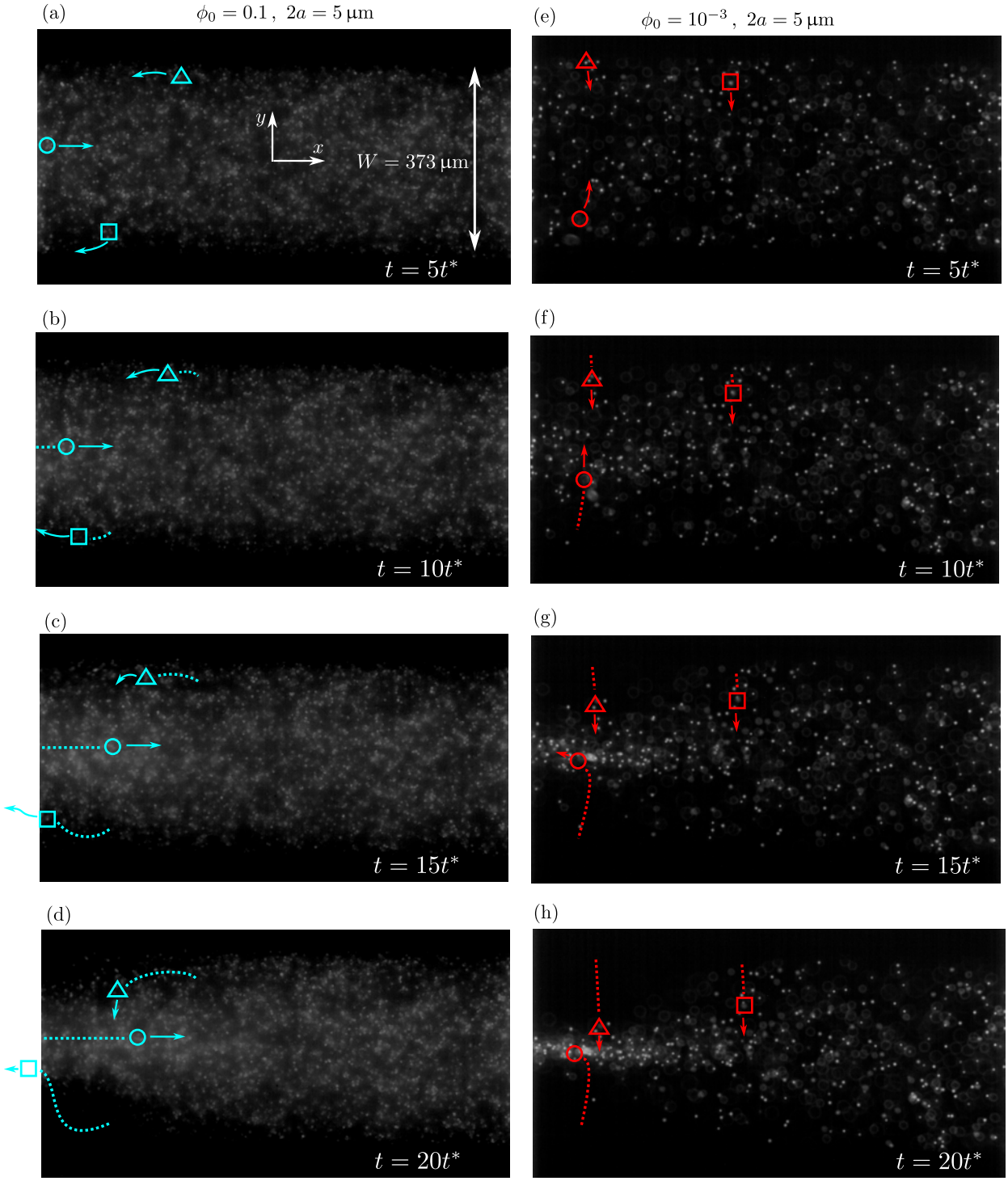

Figure 7.3: Top view images showing acoustophoretic focusing of $2a = 5\,\mu\text{m}$ polystyrene particles in red dashed area in Fig. 7.1. For two suspensions with *different* initial concentration but same particle size $2a = 5\,\mu\text{m}$. (a)-(d) Highly concentrated $\phi_0 = 0.1$. (e)-(h) Semi dilute $\phi_0 = 0.001$ The images for each dataset are for evolving times of $t = \{5, 10, 15, 20\}\,t^*$, representing a total of 70 images from $0 < t < 20t^*$. It is seen how the concentrated suspension, in (a)-(d), exhibits a far slower particle focusing, compared to its dilute counterpart (e)-(h). The symbols (○, □ and △) represent the local movement of manually tracked clusters of particles. The arrows and the dotted lines denote the approximate local velocity and trajectory, respectively. It is seen how the movement in the concentrated regime (a)-(d), exhibits a form of "rolling motion", while the dilute suspension (e)-(h) are simple focused to the channel center. Raw images courtesy of Kevin Cushing, LTH.

Inspecting the high concentration $\phi_0 = 0.1$ in Fig. 7.3(a)-(d), we see that the particle behaviour changes radically. Following ○ in (a)-(d), we note how the center bulk of particles are pushed to the right. This is visible in (c)-(d), where ○ have been displaced a relatively large distance. The outer particles, represented by the blue square □ and the green triangle △, are pushed to the left, while also being focused towards the transverse pressure node. Thus, the liquid and particles almost performs a "rolling motion", while at the same time being focused. This is in some sense similar to the behaviour observed for simulated particle trajectories in Fig. 6.7(b), though our simulations suggest that fluid convection effects would not so pronounced for particle sizes of $2a = 5\,\mu\text{m}$. This could be due to the fact that the model by Happel and Brenner [18] are too mild, giving estimates that are to low compared to the true values. The experimental data suggests in this way that the actual enhanced effective viscosity $\psi(\phi)$ might in fact be higher, and the particle mobility $\chi(\phi)$ might in fact be lower.

7.2 Omitted physical effects

We touch upon some of the physical effects we have omitted in the theoretical approach taken in this thesis.

7.2.1 Acoustic particle-particle wave scattering

One of the known particle-particle interaction effect that exists in ultrasonic acoustofluidics, is the effects of higher order scattering events of the acoustic field [46, 47]. When an incoming acoustic field scatters on a particle, other nearby particles feel the scattered field. This gives rise to secondary acoustic radiation forces, known as Bjerknes forces, and was first discovered for gas bubbles [48, 49]. As we are in the high concentration regime these effects might play a role for the particle dynamics. However, because polystyrene particles in water can be considered as weak scatterers [29], compared to the strong scattering by gas bubbles [48, 49], we have neglected this effect in this thesis, seeing as it is a full research topic on its own.

7.2.2 Influence of acoustic streaming

Another phenomenon omitted in our theoretical description, is the acoustic streaming [24, 25]. In the context of discussing the influence of acoustic streaming, it is relevant to compare the effects of convection rolls versus streaming rolls, see sections 6.1 and 2.2.2.

In Section 3.4.2 we defined and calculated the critical particle size $2a_{\text{str}} = 2\,\mu\text{m}$, below which, streaming effects are dominant. The critical particle size was defined as the turnover size $2a_{\text{str}}$ where the acoustic radiation force $\boldsymbol{F}_{\text{ac}}$ becomes dominant over the streaming drag force $6\pi\eta a v_{\text{str}}$. For streaming effects to become significant, we briefly consider particles of the critical size $2a_{\text{str}}$.

For particles of this size, we found the convection roll velocities to be of the order of the chosen characteristic fluid velocity $v \sim v^* = u_{\text{p}}$, see Fig. 6.3. Where u_{p} is the particle velocity in the dilute limit, given by $u_{\text{p}} = F_{\text{ac}}/(6\pi\eta a)$. This implies that around the critical particle size $2a_{\text{str}} = 2\,\mu\text{m}$, the convection roll velocities are expected to be of the same order of magnitude as the streaming rolls $v \sim v_{\text{str}}$, making their drag force contributions to the particle dynamics equally important.

From a biological viewpoint, it is of great interest to be able to acoustically manipulate biological particles smaller than the critical particle size $2a_{\text{str}}$, e.g. separation of *E. coli* bacteria where$2a \approx 1\,\mu\text{m}$, from other biofilaments [13]. Thus, in a study of very small particles in the high concentration limit, inclusion of both streaming and convection rolls would indeed be necessary.

7.2.3 Change of sound propagation properties

The sound propagation properties of the fluid is determined by the fluid compressibility κ_{wa} and mass density ρ_{wa}. One could imagine that when the volume of concentration of particles ϕ became significantly large, the effective sound propagation properties of the effective medium, might change. In return this could change the resonance frequency of the system, which would need to be recalibrated.

As a first approximation, one could try to identify an effective medium compressibility κ_{eff} and mass density ρ_{eff}, including the particle compressibility κ_{p} and mass density ρ_{p}, and recalculate the resonance frequency and the first-order acoustic fields $\boldsymbol{v}_1$ and p_1, which in turn yields a modified acoustic radiation force $\boldsymbol{F}_{\text{ac,eff}}$.

7.3 Model strengths and weaknesses

7.3.1 Model Strengths

When comparing the model qualitatively with experiment, it is clear that the model captures the essence of the change in particle behaviour, for highly concentrated suspensions. Namely that the particle focusing and movement slows down in general. This is due to the decrease in particle mobility $\chi < 1$ and increase in effective medium viscosity $\psi > 1$ for high concentrations, see Fig. 2.3. These effective interaction effects turns out be imperative in the description of particle focusing of highly concentrated suspensions. In some sense, this result is obvious, since focusing of particles is fully equivalent to forcing the particles to move relative to the surrounding fluid, which is exactly what the concept of particle mobility describes.

Moreover, the model captures the essential hydrodynamic coupling between the particles and the global velocity field of the liquid $\boldsymbol{v}$. Even though we saw that the net transport of the particles was largely unchanged by inclusion of the fluid movement in our geometry, one could imagine other systems where this coupling would be important in a correct description of the net transport of particles. Mikkelsen and Bruus [38] considers a similar model for the coupling of the fluid velocity $\boldsymbol{v}$ to particle transport $\boldsymbol{J}_{\text{p}}$, but for a system of paramagnetic beads subjected to an external magnetic field. The particle size considered is $2a = 1\,\mu\text{m}$, approximately similar to what is considered in this thesis. They find that convective effects become significant at volume concentrations around $\phi_0 = 0.04$, but do not consider the effects of changed particle mobility $\chi(\phi)$ and effective medium viscosity $\psi(\phi)$. At this level of volume concentrations, the particle dynamics are significantly affected by the changed particle mobility $\chi(0.04) = 0.49$ and effective medium viscosity $\psi(0.04) = 1.22$ which may lead to very different conclusions than presented by Mikkelsen and Bruus [38].

7.3.2 Model Weaknesses

Variance of the concentration field

In this description of the particles, we have disregarded the discrete nature of the particles. Thus we describe only the mean values of all quantities. Therefore, in this description, no information can be obtained about the expected variance of the respective fields. This could become important when increasing the particle size, thus decreasing the total number of particles and increasing the expected variances of the various fields.

Numerical Stability

In our model formulation of the acoustophoretic particle focusing, the particles are so big that diffusion effects are minute. Therefore, no steady state of the concentration field is reached in the simulation before COMSOL eventually crashes. This is due to the build-up of very large numerical concentration gradients. This problem is especially pronounced for simulations with high number concentrations c, which implies small particles $2a$ and high volume concentration ϕ. This is problematic because one of the goals with our model, is to predict the behaviour of highly concentrated suspensions. This could possibly be resolved by making a time independent flow-through model. In such a model we imagine particles continuously being flushed in from one side of the computation domain Ω with a Poiseuille flow, and leave at the other side of the computation, after being focused in an active acoustic force region in Ω. The concentration field undergoing acoustophoretic focusing, could then be studied as function of particle size $2a$ and initial concentration ϕ_0. A model of this form would prevent transient the build-ups of very large numerical concentration gradients, thereby possibly avoiding numerical crashes. In this context it is worth mentioning that we do not expect these numerical issues to be the result of too large mesh Péclet numbers[1] , as this problem is observed in the COMSOL simulations regardless of whether or not diffusion effects are in included.

Secondly, as the problem would no longer be transient, one could avoid solving for many time steps. Lastly, a model of this form would have high experimental relevance as experiments are often performed as "flow-through". Another way to possibly improve this issue, is to rewrite the fluid dynamical equations directly in weak form, avoiding the in-built *Creeping flow* module in COMSOL. This would allow for more direct control over the mathematical details in the model, e.g. investigating the effects of choosing higher order basis function for the concentration and fluid fields.

Model for effective viscosity and particle mobility

One of the important points for discussion in our model, is the approximative models used for effective medium viscosity $\psi(\phi)$ and particle mobility $\chi(\phi)$ by Happel and Brenner [18, 32], see Section 2.3.

Because these corrections plays such a crucial role in the particle dynamics for concentrated suspensions, it is important review the physical correctness of the model in an objective light. We therefore re-examine the imposed boundary conditions in the cell model by Happel and Brenner.

From Section 2.3 we recall that the boundary condition for the outer surface of the cell is 1) no-normal fluid velocity $\boldsymbol{v} \cdot \boldsymbol{n}|_{r=b} = 0$, and 2) no tangential stress. If just focusing on the no-normal fluid flow condition, we imagine pressing an incompressible liquid through a stationary assemblage of spheres. This is sketched in Fig. 7.4, for cases of increasing of volume concentration ϕ.

In the figure it is seen how the boundary condition of no-normal fluid flow at the cell boundary at $r = b$ is violated $\boldsymbol{v} \cdot \boldsymbol{n}|_{r=b} \neq 0$, but becomes an increasingly better approximation as the volume concentration increases, because the streamlines are forced to run increasingly parallel to the cell boundary. From the principal sketch, we also note that the no tangential stress condition is also violated, since this would require the streamlines to be symmetrical at all points around the cell boundary at $r = b$.

[1]The Péclet number [5] is given as the ratio between convective and diffusive transport $Pé = \boldsymbol{J}_{\text{conv}}/\boldsymbol{J}_{\text{diff}}$. The mesh Péclet number is the Péclet number over the length scale of mesh element size d_{mesh}. If the mesh Péclet number is too big, it is known to cause problem when numerically solving convection-diffusion problems.

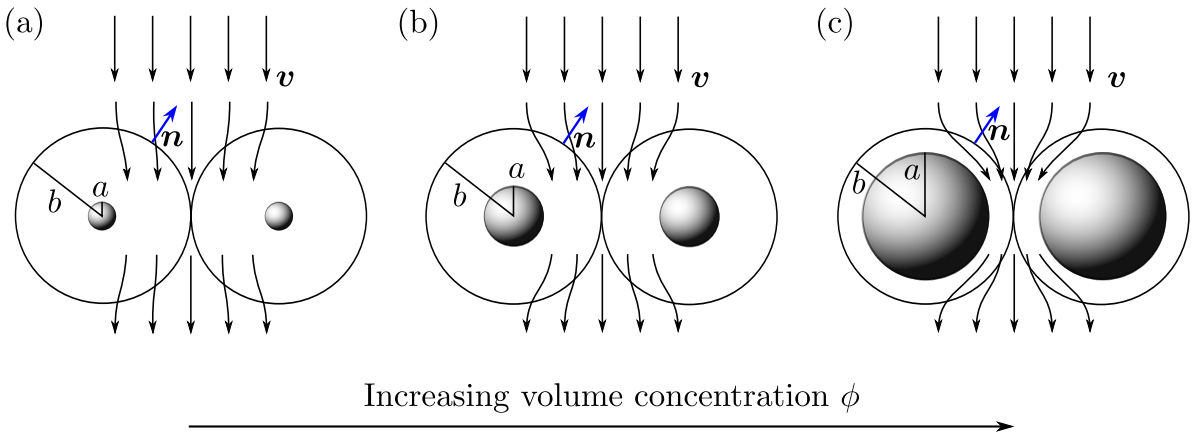

Figure 7.4: Principal sketch for investigating the no-normal fluid flow condition $\boldsymbol{v} \cdot \boldsymbol{n}|_{r=b} = 0$, in the Cell model by Happel and Brenner [18, 32], see Section 2.3. In this sketch we imagine some incompressible liquid, being pressed with velocity $\boldsymbol{v}$ through an assemblage of stationary spheres. The situation is sketched for three cases of increasing volume concentration ϕ, with inner particle radius a and outer cell radius b. It is noted how the no-normal fluid velocity at the cell boundary is violated in the different cases $\boldsymbol{v} \cdot \boldsymbol{n}|_{r=b} \neq 0$, where $\boldsymbol{n}$ is denoted by blue arrows. However, we note how the boundary condition becomes a better approximation for larger volume concentrations.

For this reason, we have briefly reviewed what other models exists in the literature. In a review paper from 2003 by Zeidan [30] 28 works are listed on this subject, using different calculation methods, and for different regimes (dilute vs. concentrated). The most promising paper looks to be a paper by Smith [50] from 1998 which mentions the models by Happel and Brenner [18, 32], but tries to include that fluid can enter and leave the cells. Another review paper is that of Barnea and Mizrahi from 1973 [51]. This paper is of more general interest, as it summarises some of the different techniques used for calculating the effective viscosity and particle mobility changes as function of volume concentration, along with some of the pros and cons of the different approaches. In the literature it is pointed out that not only volume concentration ϕ influences the viscous properties of particle suspensions, but also non Newtonian effects are also reported to play a role [52, 53]. This along with effects of surface roughness of particles [54], and the degree of flocculation(agglomeration) [55].

From this discussion it is clear that many factors exists within colloidal science that is able to change the particle mobility χ and the effective medium viscosity ψ, and that the exact dependence of χ and ψ on these factors quickly can become rather complicated. We therefore conclude that a more thorough literature study is needed in order to clarify which improvements one should use beyond Happel and Brenners Cell model.

7.4 Suggestions for further work

Based on the discussion in the previous sections we here list some suggestions for further work that are natural to pursue.

7.4.1 Experimental characterisation and calibration

Mapping the acoustic field

One of the uncertainties when comparing the numerical results with experimental data is the exact form of the acoustic fields $\boldsymbol{v}_1$ and p_1. Because the acoustic radiation force $\boldsymbol{F}_{\text{ac}}$ is the driving mechanism for the derivation for the particle dynamics, the specific form of the acoustic fields $\boldsymbol{v}_1$ and p_1 are vital in order to make quantitative predictions for the particle dynamics. Augustsson *et al.* [36] showed that the lateral modulation of the acoustic field, in the channel identical to the one used in the preliminary experiments, to be irregular and unpredictable from simple theory. But they found the form of the acoustic fields to be reproducible and stable in time. This would allow us to precisely map the acoustic field a certain part of the channel, and from this derive the precise acoustic radiation force $\boldsymbol{F}_{\text{ac}}$ to enter in our numerical model, for new quantifiable predictions.

Calibrating particle concentration with pixel intensity

Another issue in order to make quantitative predictions is knowing exactly how the pixel intensity is related to the concentration of the fluorescent microparticles in the raw images. We recall from Section 7.1.1 that only a small fraction of fluorescent particles were added to represent the full ensemble of particles. In our preliminary investigation of the data, we found that the pixel-intensity saturates at a certain concentration of fluorescent particles. This could be solved by making a precise calibration between pixel intensity and concentration of fluorescent microparticles in the channel. In this way one could choose the optimal dynamic working range of concentrations of fluorescent microparticles, in which the concentration of fluorescent particles could be directly related to the pixel intensity, and then simple vary the ratio of fluorescent to non-fluorescent particles to stay within the dynamic working range.

7.4.2 Improved model for effective medium viscosity and particle mobility

Another improvement of the modelling framework is the approximative model used for the changes of effective medium viscosity and particle mobility. Following the discussion of Section 7.3.2, it is clear that a thorough literature study is needed to clarify what improvements should be implemented. As a starting point we suggest the review paper by Zeidan [30] supplemented by a study of the model by Smith [50]. On the longer term it would be of interest to investigate the effects on viscosity of soft deformable particles. This would bring us one step closer to a theoretical understanding of bioparticle suspensions in acoustophoresis. From a biological viewpoint this is an interesting scope since red blood cells in blood can occupy volume concentrations of the order $\phi_0 \sim 0.4$ [16].

7.4.3 Numerical Flow Through model and experiment

Another natural continuation of this thesis work is to develop a "flow-through" model, mentioned in the discussion on numerical stability in Section 7.3.2. The main advantages of such a model lies in several aspects. Better numerical stability could possibly be obtained, along with the fact that such a model would be time independent, allowing to solve for only one time step. Furthermore, this type of model would allow for direct comparison between theory and experiment, directly comparing the particle concentration profiles in the active focusing region. One could then study these particle focusing profiles as function particle size $2a$, concentration ϕ_0 and other parameters

of interest. Experimentally this would be easy to implement since continuous "flow-through" experiments are easily performed in acoustofluidics [8].

Chapter 8

Conclusion and outlook

8.1 Conclusion

In this thesis we have developed a theoretical modelling framework for predicting the behaviour of suspended microparticles undergoing acoustophoresis. The main focus has been on understanding how highly concentrated particle suspensions behave differently from the well known dilute suspensions, characterised in previous works [37, 36, 43]. This was achieved by making a series of simplifications allowing the formulation of a set of numerically solvable governing equations. In this numerical framework we implemented two categories of particle-particle interactions, giving rise to different behaviours in the dilute versus the concentrated regimes. The first type of interactions, comes from the fact that the effective viscosity of the suspension and the Stokes drag force felt by particles increases, for increasing particle concentrations. The second interaction effect arises from allowing the particles to transfer momentum to the suspending fluid, setting it in motion. This motion introduces convective contributions to the particle transport, thus influencing the particle dynamics.

We find that the interaction effects through enhanced effective viscosity and particle drag forces, are by far the most significant interaction effect for the net transport of particles. This is relevant for particle sorting and upconcentration purposes. As a general result, we conclude that the particle dynamics slows down for increasing particle concentrations. Furthermore, we find that for 1% particle volume concentration, the focus time has increased by $\approx 50\%$, and by volume of 3%, the focus time has approximately doubled, thus exhibiting a non-linear dependence of the particle concentration. Moreover, we conclude that the particle focus times depends minutely on the particle size.

Since the particle suspension dynamics in our geometry are dominated by the enhanced viscosity effects, we point out that the correctness of these result are limited to the correctness of the model by Happel and Brenner [18], and we conclude that further studies in these models of viscosity effects are needed.

In general we find that the second type particle-particle interactions, which is mediated by the fluid convection, are important for a correct description of concentrated particle dynamics. However, we find that this interaction effect has very little influence for the purposes of particle focusing in our geometry. One could imagine other device geometries where the convective contribution to the particle behaviour might become important for the net transport and focusing of particles. This could possibly occur in acoustofluidic systems where the ultrasonic actuation was confined to small parts of the channel [12], giving strong lateral modulation of the overall particle dynamics.

8.2 Outlook

Based on the suggestions for further work in Section 7.4, we here list three concrete steps for improving the theoretical model framework. Thus enabling the model to make quantitative predictions of the acoustophoretic particle dynamics in concentrated suspensions that can be directly experimentally validated.

Acoustic characterisation and concentration callibration

In order to make quantitative predictions, the acoustic field used in the experimental system needs to be characterised in detail. Augustsson *et al.* [36] showed the lateral modulation of the acoustic fields in the channel to be irregular, and not directly predictable by theory. However, they also found the acoustic field to be stable in time and reproducible. In this way, it would be possible to map a specific part of the channel in detail. This would allow for a more physically correct form of the acoustic radiation force, to enter in the numerical simulations.

Furthermore it is necessary to perform a series of calibration measurements in order to relate the image pixel intensity from the raw microscope images to the precise concentration of fluorescent microparticles in the channel. Thus allowing quantitative measurements of particle concentrations directly from images.

Model studies of particle mobility and effective viscosity

In order to further study the models for enhanced effective medium viscosity and drag force on the particles, we suggest a literature study with a starting point in the review paper by Zeidan [30], supplemented with the review by Barnea and Mizrahi [51] for more general background. Furthermore, we suggest studying the extension of Happel and Brenners model by Smith [50].

From a brief discussion on some of the literature on these effects in Section 7.3.2, it is apparent that these viscosity modifications might also depend upon other parameters, such as particle surface properties or fluid shear rate [54, 55, 52, 53]. These consideration might be of relevance on the longer term, as we ultimately want to model the behaviour of complex biological liquid suspensions.

Theoretical flow-through model and experiment

With the above inputs for the modelling framework, we propose the development of a steady state numerical "flow-through" model. In such a model we imagine a homogeneous unfocused particle suspension continuously being flushed in from one end of the computation domain. The particles travel through an active acoustic region where they are focused, and leave at the other end of the simulation domain. The concentration profile throughout the acoustic focusing region could then be studied as a function of initial particle concentration and size, and be directly compared with concentration profiles obtained in new flow-through experiments.

Appendix A

Material parameters

List of relevant material parameters, see Table A.1

Table A.1: Relevant material parameters. Values given at ambient temperature 25 °C [20]

Water			
Dynamic viscosity	η	$= 0.893 \times 10^{-3}$	Pa s
Mass density	ρ	$= 0.998 \times 10^{3}$	kg m^{-3}
Isentropic speed of sound	v_{s}	$= 1.497 \times 10^{3}$	m s^{-1}
Polystyrene			
Mass density	ρ_{ps}	$= 1.050 \times 10^{3}$	kg m^{-3}
Isentropic speed of sound	$v_{\mathrm{s,\,ps}}$	$= 2.350 \times 10^{3}$	m s^{-1}

Appendix B

Lambs solution to the Stokes equation

We review some of the fundamental aspects of Lambs general solution to the Stokes equation [34].

By taking the divergence of the Stokes equation (2.22a), and using the continuity equation (2.22b), we see that the pressure has to obey a Laplace equation $\nabla^2 p = 0$, Therefore, the general solution in spherical co-ordinates, is an infinite sum of spherical harmonics

$$p(r,\theta) = \sum_{n=-\infty}^{\infty} p_n(r,\theta)\,. \tag{B.1}$$

For more information on the spherical harmonic functions, and determining then, see Lamb [34], chapter 5. Again using spherical harmonic function, one can solve the homogeneous set of equations

$$\nabla^2 \boldsymbol{v}_{\mathrm{h}} = \boldsymbol{0} \tag{B.2a}$$
$$\boldsymbol{\nabla}\cdot\boldsymbol{v}_{\mathrm{h}} = 0\,, \tag{B.2b}$$

where the subscript h, implies homogeneous velocity field, resulting in the solution

$$\boldsymbol{v}_{\mathrm{h}} = \sum_{n=-\infty}^{\infty} \left(\boldsymbol{\nabla}\times(\boldsymbol{r}f_n) + \boldsymbol{\nabla}g_n\right)\,, \tag{B.3}$$

where f_n, and g_n are harmonic functions. The full solution is found by adding the gradient of the pressure (B.1)

$$\boldsymbol{v} = \sum_{n=-\infty}^{\infty} \left(\boldsymbol{\nabla}\times(\boldsymbol{r}f_n) + \boldsymbol{\nabla}g_n + \frac{n+3}{2\eta(n+1)(2n+3)} r^2\boldsymbol{\nabla}p_n - \frac{n}{\eta(n+1)(2n+3)}\boldsymbol{r}p_n\right)\,. \tag{B.4}$$

B.1 Solving the specific flow for the particle mobility problem

Next, the boundary conditions Eqs. (2.23) and (2.24) are used to determine coefficients for each n in Eq. (B.4). To satisfy the boundary conditions, one can set $f_n = 0$, and only retain the term of g_n and p_n corresponding to $n = -2$ and $n = 1$, this implies that the velocity field simplifies to

$$\boldsymbol{v} = \boldsymbol{\nabla}g_1 + \boldsymbol{\nabla}g_{-2} + \frac{1}{5}r^2\boldsymbol{\nabla}p_1 - \frac{1}{10}\boldsymbol{r}p_1 + \frac{1}{2}r^2\boldsymbol{\nabla}p_{-2} + 2\boldsymbol{r}p_{-2}\,. \tag{B.5}$$

Due to symmetry of the boundary conditions Eqs. (2.23) and (2.24), we are led to assume that

$$g_1 = Az \tag{B.6a}$$

$$p_1 = Bz \tag{B.6b}$$

$$g_{-2} = -C\partial_z \left(\frac{1}{r}\right) = \frac{Cz}{r^3} \tag{B.6c}$$

$$p_{-2} = -D\partial_z \left(\frac{1}{r}\right) = \frac{Dz}{r^3}\,. \tag{B.6d}$$

In the case of spherical harmonics, Brenner calculates the frictional force on a sphere, see [18], section 3-2. By evaluating the Cauchy stress tensor at the surface of the sphere, and integrating over the surface of the sphere, Brenner deduces the simple result

$$\boldsymbol{F}_\mathrm{d} = -4\pi\boldsymbol{\nabla}(r^3 p_{-2})\,, \tag{B.7}$$

implying that only the constant D, needs to be determined to calculate the modified drag force on the sphere. Inserting Eq. (B.6d) in Brenners result for the drag force Eq. (B.7), it is clear that $F_\mathrm{d} = -4\pi\eta\, D$. From the boundary conditions Eqs. (2.23), (2.24) and (2.25), Brenner finds

$$D = a u_\mathrm{p} \frac{3 + 2\phi^{5/3}}{2 - 3\phi^{1/3} + 3\phi^{5/3} - 2\phi^2}\,. \tag{B.8}$$

Inserting the value for D, the modified drag force becomes

$$\boldsymbol{F}_\mathrm{d} = -6\pi\eta a \left[\frac{2}{3}\frac{3 + 2\phi^{5/3}}{2 - 3\phi^{1/3} + 3\phi^{5/3} - 2\phi^2}\right](\boldsymbol{u}_\mathrm{p} - \boldsymbol{v})\,, \tag{B.9}$$

Bibliography

[1] O. Geschke, H. Klank, and P. Tellemann, *Microsystem engineering of lab-on-a-chip devices* (John Wiley & Sons, New York) (2004).

[2] P. Tabeling, *Introduction to Microfluidics* (Oxford University Press, USA) (2006).

[3] J. Berthier and P. Silberzan, *Microfluidics for biotechnology.* Artech House microelectromechanical systems series (Artech House, Boston (Mass.), London) (2006).

[4] B. Kirby, *Micro- and Nanoscale Fluid Mechanics: Transport in Microfluidic Devices* (Cambridge University Press) (2010).

[5] H. Bruus, *Theoretical microfluidics*, vol. 18 (Oxford University Press, USA) (2007).

[6] H. Tsutsui and C.-M. Ho, *Cell separation by non-inertial force fields in microfluidic systems.* MECHANICS RESEARCH COMMUNICATIONS **36**(1), 92–103 (2009).

[7] H. Bruus, J. Dual, J. Hawkes, M. Hill, T. Laurell, J. Nilsson, S. Radel, S. Sadhal, and M. Wiklund, *Forthcoming lab on a chip tutorial series on acoustofluidics: Acoustofluidics-exploiting ultrasonic standing wave forces and acoustic streaming in microfluidic systems for cell and particle manipulation.* Lab Chip **11**, 3579–3580 (2011).

[8] A. Lenshof, C. Magnusson, and T. Laurell, *Acoustofluidics 8: Applications of acoustophoresis in continuous flow microsystems.* Lab Chip **12**, 1210–1223 (2012).

[9] M. Wiklund, *Acoustofluidics 12: biocompatibility and cell viability in microfluidic acoustic resonators (vol 12, pg 2018, 2012).* LAB ON A CHIP **12**(24), 5283 (2012).

[10] C. Grenvall, J. R. Folkenberg, P. Augustsson, and T. Laurell, *Label-free somatic cell cytometry in raw milk using acoustophoresis.* CYTOMETRY PART a **81A**(12), 1076–1083 (2012).

[11] H. Bruus, *Acoustofluidics 7: The acoustic radiation force on small particles.* Lab Chip **12**, 1014–1021 (2012).

[12] H. Wang, Y. Qiu, C. Demore, S. Cochran, P. Glynne-Jones, and M. Hill, *Particle manipulation in a microfluidic channel with an electronically controlled linear piezoelectric array.* 2012 IEEE INTERNATIONAL ULTRASONICS SYMPOSIUM (IUS) – (2012).

[13] Y. Ai, C. K. Sanders, and B. L. Marrone, *Separation of escherichia coli bacteria from peripheral blood mononuclear cells using standing surface acoustic waves.* Analytical Chemistry - Columbus **85**(19), 9126 (2013).

[14] C. Greenvall, P. Augustsson, J. R. Folkenberg, and T. Laurell, *Harmonic microchip acoustophoresis: a route to online raw milk sample precondition in protein and lipid content quality control.* Analytical Chemistry **81**(15), 6195–6200 (2009).

[15] H. Jonsson, C. Holm, A. Nilsson, F. Petersson, P. Johnsson, and T. Laurell, *Particle separation using ultrasound can radically reduce embolic load to brain after cardiac surgery.* ANNALS OF THORACIC SURGERY **78**(5), 1572–1578 (2004).

[16] F. Petersson, A. Nilsson, C. Holm, H. Jonsson, and T. Laurell, *Separation of lipids from blood utilizing ultrasonic standing waves in microfluidic channels.* ANALYST -LONDON-SOCIETY OF PUBLIC ANALYSTS THEN ROYAL SOCIETY OF CHEMISTRY- **129**(10), 938–943 (2004).

[17] M. Nordin and T. Laurell, *Two-hundredfold volume concentration of dilute cell and particle suspensions using chip integrated multistage acoustophoresis.* LAB ON a CHIP **12**(22), 4610–4616 (2012).

[18] J. Happel and H. Brenner, *Low Reynolds Number Hydrodynamics: With Special Applications to Particulate Media.* Mechanics of Fluids and Transport Processes Series (Prentice-Hall) (1965).

[19] A. S. Dukhin and P. J. Goetz, *Bulk viscosity and compressibility measurement using acoustic spectroscopy.* Journal of Chemical Physics **130**(12), 124519 (2009).

[20] H. Bruus, *Acoustofluidics 2: Perturbation theory and ultrasound resonance modes.* Lab Chip **12**, 20–28 (2012).

[21] *Acoustofluidics: theory and simulation of radiation forces at ultrasound resonances in microfluidic devices*, vol. 6 (Acoustical Society of America through the American Institute of Physics) (2009), proceedings to the 157th meeting of Acoustical Society of America, authored by Barnkob, Rune and Bruus, Henrik.

[22] P. B. Muller, *Acoustofluidics in microsystems: investigation of acoustic streaming.* Master's thesis, Technical University of Denmark, DTU, Department of micro- and nanotechnology (2012), supervised by Professor Henrik Bruus. For copy, visit.

[23] L. D. Landau and E. M. Lifshitz, *Fluid mechanics.* Course of theoretical physics / by L. D. Landau and E. M. Lifshitz, Vol. 6 (Elsevier/Butterworth-Heinemann), 2nd edn. (2000).

[24] P. B. Muller, R. Barnkob, M. J. H. Jensen, and H. Bruus, *A numerical study of microparticle acoustophoresis driven by acoustic radiation forces and streaming-induced drag forces.* Lab Chip **12**, 4617–4627 (2012).

[25] P. B. Muller, M. Rossi, A. G. Marin, R. Barnkob, P. Augustsson, T. Laurell, C. J. Kähler, and H. Bruus, *Ultrasound-induced acoustophoretic motion of microparticles in three dimensions.* Phys. Rev. E **88**, 023006 (2013).

[26] L. Rayleigh, *On the circulation of air observed in kundt's tubes, and on some allied acoustical problems.* Philosophical Transactions of the Royal Society of London **175**, 1–21 (1884).

[27] H. Schlichting, *Berechnung ebener periodischer grenzschichtströmungen.* Phys. Z **33**, 327–335 (1932).

[28] L. Gor'kov, *On the forces acting on a small particle in an acoustal field in an ideal fluid.* Soviet Physics - Doklady **6**, 88 (1962).

[29] M. Settnes and H. Bruus, *Forces acting on a small particle in an acoustical field in a viscous fluid.* Phys. Rev. E **85**, 016327 (2012).

[30] A. Zeidan, S. Rohani, A. Bassi, and P. Whiting, *Review and comparison of solids settling velocity models*. REVIEWS IN CHEMICAL ENGINEERING **19**(5), 473–530 (2003).

[31] M. H. Abu-Ali, *Sedimentation of homogeneous suspensions at intermediate particle reynolds numbers*. International Journal of Mineral Processing **50**(3), 161–175 (1997).

[32] Happel, *Viscosity of suspensions of uniform spheres*. Journal of Applied Physics **28**(11), 1288–1292 (1957).

[33] B. Lautrup, *Physics of Continuous Matter: Exotic and Everyday Phenomena in the Macroscopic Worl d* (Institute of Physics Publishing, Bristol.) (2005).

[34] H. Lamb, *Hydrodynamics*. Kessinger Publishing's rare reprints (Kessinger Publishing) (1895).

[35] A. Lenshof, M. Evander, T. Laurell, and J. Nilsson, *Acoustofluidics 5: Building microfluidic acoustic resonators*. Lab Chip **12**, 684–695 (2012).

[36] P. Augustsson, R. Barnkob, S. T. Wereley, H. Bruus, and T. Laurell, *Automated and temperature-controlled micro-piv measurements enabling long-term-stable microchannel acoustophoresis characterization*. Lab Chip **11**, 4152–4164 (2011).

[37] R. Barnkob, P. Augustsson, T. Laurell, and H. Bruus, *Measuring the local pressure amplitude in microchannel acoustophoresis*. Lab On a Chip **10**(5), 563–570 (2010).

[38] C. Mikkelsen and H. Bruus, *Microfluidic capturing-dynamics of paramagnetic bead suspensions*. Lab Chip **5**(11), 1293–1297 (2005).

[39] R. Barnkob, I. Iranmanesh, M. Wiklund, and H. Bruus, *Measuring acoustic energy density in microchannel acoustophoresis using a simple and rapid light-intensity method*. Lab On a Chip **12**(13), 2337–2344 (2012).

[40] COMSOL, *COMSOL Multiphysics Reference Guide*. November 2012 comsol 4.3a edn. (2012).

[41] C. P. Nielsen, *Introduction to weak form modeling in comsol* (2013), note on weak form and COMSOL implementation. version 1.3.

[42] L. H. Olesen, *Computational Fluid Dynamics in Microfluidic Systems*. Master's thesis, Mikroelektronik Centret (MIC), Technical University of Denmark (2003), supervised by Professor Henrik Bruus.

[43] R. Barnkob, P. Augustsson, T. Laurell, and H. Bruus, *Acoustic radiation- and streaming-induced microparticle velocities determined by microparticle image velocimetry in an ultrasound symmetry plane*. Phys. Rev. E **86**, 056307 (2012).

[44] W. Brevis, Y. Nino, and G. H. Jirka, *Integrating cross-correlation and relaxation algorithms for particle tracking velocimetry*. EXPERIMENTS IN FLUIDS **50**(1), 135–147 (2011).

[45] H. Faxén, *Der widerstand gegen die bewegung einer starren kugel in einer zähen flüssigkeit, die zwischen zwei parallelen ebenen wänden eingeschlossen ist*. Annalen der Physik **373**(10), 89–119 (1922).

[46] L. L. Foldy, *The multiple scattering of waves. i. general theory of isotropic scattering by randomly distributed scatterers*. SPIE MILESTONE SERIES MS **120**, 438–450 (1996).

[47] N. Gumerov and R. Duraiswami, *Computation of scattering from n spheres using multipole reexpansion*. JOURNAL OF THE ACOUSTICAL SOCIETY OF AMERICA **112**(6), 2688–2701 (2002).

[48] L. Crum, *Bjerknes forces on bubbles in a stationary sound field*. JOURNAL OF THE ACOUSTICAL SOCIETY OF AMERICA **57**(6), 1363–1370 (1975).

[49] T. J. A. Kokhuis, V. Garbin, K. Kooiman, B. A. Naaijkens, L. J. M. Juffermans, O. Kamp, A. F. W. van der Steen, M. Versluis, and N. de Jong, *Secondary bjerknes forces deform targeted microbubbles*. ULTRASOUND IN MEDICINE AND BIOLOGY **39**(3), 490–506 (2013).

[50] T. Smith, *A model of settling velocity*. CHEMICAL ENGINEERING SCIENCE **53**(2), 315–323 (1998).

[51] E. Barnea and J. Mizrahi, *Generalized approach to the fluid dynamics of particulate systems em dash 1. general correlation for fluidization and sedimentation in solid multiparticle systems*. Chem Eng J **5**(2), 171–189 (1973).

[52] D. Jeffrey and A. Acrivos, *Rheological properties of suspensions of rigid particles*. AICHE JOURNAL **22**(3), 417–432 (1976).

[53] D. Quemada, *Rheology of concentrated disperse systems and minimum energy dissipation principle*. Rheologica Acta **16**(1), 82–94 (1977).

[54] J. Walz, *The effect of surface heterogeneities on colloidal forces*. ADVANCES IN COLLOID AND INTERFACE SCIENCE **74**, 119–168 (1998).

[55] D. Thomas, *Transport characteristics of suspension .8. a note on viscosity of newtonian suspensions of uniform spherical particles*. JOURNAL OF COLLOID SCIENCE **20**(3), 267 (1965).